REPORT DOCUMENTATION PAGE

Form Approved
OMB No. 0704-0188

1. AGENCY USE ONLY (Leave blank)	2. REPORT DATE	3. REPORT TYPE AND DATES COVERED
		FINAL REPORT 01 Jun 92 - 31 May 95

4. TITLE AND SUBTITLE

(FY91 AASERT) Silicon-Germanium-Carbon Alloys For Optoelectronic Devices

5. FUNDING NUMBERS

3484/S3
61103D

6. AUTHOR(S)

Professor Kolodzey

7. PERFORMING ORGANIZATION NAME(S) AND ADDRESS(ES)

Department of Electrical Engineering
University of Delaware
140 Evans Hall
Newark, Delaware 19716-3130

AFOSR-TR-95

0759

9. SPONSORING / MONITORING AGENCY NAME(S) AND ADDRESS(ES)

AFOSR/NE
110 Duncan Avenue Suite B115
Bolling AFB DC 20332-0001

10. SPONSORING / MONITORING AGENCY REPORT NUMBER

F49620-92-J-0340

11. SUPPLEMENTARY NOTES

12a. DISTRIBUTION / AVAILABILITY STATEMENT

APPROVED FOR PUBLIC RELEASE: DISTRIBUTION UNLIMITED

12b. DISTRIBUTION CODE

This research resulted in the growth of this new semiconductor alloy, silicon-germanium-carbon, by the technique of molecular beam epitaxy (MBE). The alloys have been characterized by several techniques including Rutherford backscattering spectrometry (RBS) for composition, and Fourier transform infrared spectrometry (FTIR) for optical absorption.

The $Si_{1-x-y}Ge_xC_y$ alloys were successfully grown using all solid sources for the Si, Ge and C. Substrates were 75 mm diameter (100) - oriented Si wafers, and alloy layer thicknesses ranged from 10 nm to 3 μm. X-ray diffraction indicated a diamond cubic structure for the alloys which had good crystalline structure and good optical properties when grown at substrate temperatures from 500 to 600°C. The optical absorption edge was adjusted by changing the composition, indicating variations in the bandgap versus composition. The bandgaps ranged from 0.7 to 1.0 eV, and increased with the C atomic fraction, which was up to 3 at. %.

We have formed strong working relations with colleagues including Dr. S.S. Iyer at IBM/Sibond, and with Dr. R.A. Soref at Hanscom AFB. We attended technical conferences, had an invited talk, and have published technical manuscripts.

Keywords: Silicon, germanium, carbon, silicon-based alloys, optoelectronic devices, molecular beam epitaxy (MBE), Rutherford backscattering spectrometry (RBS), Fourier transform infrared spectrometry (FTIR), optical absorption.

17. SECURITY CLASSIFICATION OF REPORT	18. SECURITY CLASSIFICATION OF THIS PAGE	19. SECURITY CLASSIFICATION OF ABSTRACT	20. LIMITATION OF ABSTRACT
UNCLASSIFIED	UNCLASSIFIED	UNCLASSIFIED	

Silicon Germanium Carbon Alloys for Optoelectronic Devices

Final Report for AASERT Grant F49620-92-J-0340

James Kolodzey
Department of Electrical Engineering
University of Delaware
Newark, Delaware 19716
302/831-1164, kolodzey@ee.udel.edu

UDEE Technical Report Number 95-11-1
November 1995

This is the final report for Grant #F49620-92-J-0340 *AASERT-91, Silicon-Germanium-Carbon Alloys for Optoelectronic Devices,* awarded by the Physics and Electronics Program of the Air Force Office of Scientific Research. The period of award for this grant was June 1, 1992 through May 31, 1995.

Abstract

This research resulted in the growth of this new semiconductor alloy, silicon-germanium-carbon, by the technique of molecular beam epitaxy (MBE). The alloys have been characterized by several techniques including Rutherford backscattering spectrometry (RBS) for composition, and Fourier transform infrared spectrometry (FTIR) for optical absorption.

The $Si_{1-x-y}Ge_xC_y$ alloys were successfully grown using all solid sources for the Si, Ge and C. Substrates were 75 mm diameter (100) - oriented Si wafers, and alloy layer thicknesses ranged from 10 nm to 3 μm. X-ray diffraction indicated a diamond cubic structure for the alloys which had good crystalline structure and good optical properties when grown at substrate temperatures from 500 to 600°C. The optical absorption edge was adjusted by changing the composition, indicating variations in the bandgap versus composition. The bandgaps ranged from 0.7 to 1.0 eV, and increased with the C atomic fraction, which was up to 3 at. %.

We have formed strong working relations with colleagues including Dr. S.S. Iyer at IBM/Sibond, and with Dr. R.A. Soref at Hanscom AFB. We attended technical conferences, had an invited talk, and have published technical manuscripts.

Keywords: Silicon, germanium, carbon, silicon-based alloys, optoelectronic devices, molecular beam epitaxy (MBE), Rutherford backscattering spectrometry (RBS), Fourier transform infrared spectrometry (FTIR), optical absorption.

Publications Resulting From This Work

"Growth of GeC Alloys by Molecular Beam Epitaxy," J. Kolodzey, S. Zhang, P. O'Neil, E. Hall. R. McAnnally, and C. P. Swann, *Proc. Int. Conf. on Silicon Carbide and Related Materials,* Washington, DC, 1993, *Inst. Phys. Conf. Ser. No. 137,* 1994, Chapter 3, pp. 357-360.

"MBE Growth and Characterization of Group IV Alloys," P. A. O'Neil, MEE Thesis, Department of Electrical Engineering, University of Delaware, 1994.

"Growth of Germanium-Carbon Alloys on Silicon Substrates by Molecular Beam Epitaxy," J. Kolodzey, P. A. O'Neil, S. Zhang, B. A. Orner, K. Roe, K. M. Unruh, C. P. Swann, M. M. Waite and S. Ismat Shah, *Appl. Phys. Lett.,* Vol. 67, pp. 1865-1867, 1995.

"Optical and Electronic Properties of SiGeC Alloys Grown on Si Substrates," J. Kolodzey, P. R. Berger, B. A. Orner, D. Hits, F. Chen, A. Khan, X.Shao, M. M. Waite, S. Ismat Shah, C. P. Swann, and K. M. Unruh, invited talk at the 5th Int. Symp. on Silicon Molecular Beam Epitaxy, E-MRS Conf., Strasbourg, May 1995, *J. Crystal Growth,* 1995, in press.

"Properties of Group IV Semiconductor Alloys Grown by Molecular Beam Epitaxy," B. A. Orner, MEE Thesis, Department of Electrical Engineering, University of Delaware, 1995.

Acknowledgements

The authors wish to acknowledge the many contributions of their colleagues:

Main Contributors

Suibin Zhang: X-Ray Diffraction, MBE

Prof. Charles P. Swann: RBS Characterization

Dr. Phillip Thompson: SIMS

Additional Contributions by:

Bradley Orner, Robbie McAnnally, Eric Hall, Charles Woerner: MBE

Al Khan, Brian Watson, Prof. Mark Barteau, and Prof. John Kramer: Auger

William W. Rule: Carbon Filament.

Dr. Subramanian Iyer, Dr. Adrian Powell, Bruce Ek: Advice on SiGeC MBE Growth

Financial Support by:

Grant: Air Force Office of Scientific Research (AFOSR) 91-0370

Augmentation Award for Science and Engineering Training (AASERT) under award: F49620-92-J-0340

Special Thanks to:

Don Nelson, Doke Scott, Prof. Charles Swann, Barbara Westog, Tom Goodwin, Sudhakar Kalluri, Sunita Bhatia, and Dr. James V. Masi

TABLE OF CONTENTS

LIST OF FIGURES

LIST OF TABLES

ABSTRACT

The growth and development of a silicon lattice-matched, group IV alloy could extend the present-day heterostructure technology to include new IC compatible silicon based devices. Such an alloy may have potential applications in the areas of heterojunction bipolar transistor technology, light emission, or long-wavelength infrared detection. In order to determine the device potential of such an alloy, the material's electrical, optical, and structural properties must be determined for various compositions. Growth optimization and compositional analysis has been performed on germanium-carbon and silicon-germanium-carbon alloys in hopes to obtain a silicon lattice-matched material compatible for heterostructure applications. The growth of the group IV alloys has been performed by molecular beam epitaxy (MBE) and compositional analysis has been investigated using Auger Electron Spectroscopy (AES), Rutherford Backscattering Spectrometry (RBS), and Secondary Ion Mass Spectrometry (SIMS). In order to determine the composition of low carbon concentration alloys, molecular growth and incorporation rates were calculated using experimental data obtained from RBS. Average alloy compositions have been determined for each sample and additional growth phenomena such as carbon filament evaporation and carbon film segregation have been investigated.

Chapter 1

INTRODUCTION

1.1 Heterojunctions

In the search for improved device performance, numerous researchers have discovered the advantages of using heterojunction materials in electronic and optoelectronic applications. By careful choice of the bandgap and band offsets of the materials comprising the junction, increased carrier injection and/or increased carrier confinement may result [1]. Bandgap engineering can enhance device performance by improving device characteristics including: increased efficiency, cutoff frequency, mobility, or lasing capability (through decreased threshold current) depending on the device. This raises the question: why aren't most devices heterostructures? Unfortunately not all materials can be ideally lattice matched with one another to form a heterojunction. In the past a large amount of success has been attained with group III-V compounds and alloys for the fabrication of heterostructure devices. This is largely due to the ease with which many of these compounds and alloys could be lattice matched with one another. If the two materials comprising a heterojunction are of differing structures or lattice parameters, a uniform unstrained junction transition cannot be achieved. A small lattice mismatch may produce only strain; a large mismatch, however, may produce interfacial defects such as misfit dislocations. These defects are best avoided since a misfit dislocation will produce a dangling bond [2], act as a trap or current leakage site, and reduce the device's performance. Along with a material's band structure, both the lattice structure and lattice parameter need to be considered when evaluating a potential heterojunction.

1.2 Group IV Alloys

Heterostructures of the III-V compound materials remain incompatible with established silicon circuit integration and processing techniques. As a result, virtually all large scale integration utilizes silicon, a group IV semiconductor. Silicon is the preferred semiconductor processing material since it forms a stable oxide which is effectively utilized as an insulation and a diffusion barrier during device processing. Group III-V compounds do not form oxides as readily as silicon and therefore processing of these materials can be quite difficult and costly. Furthermore, silicon, the third most abundant element, is inexpensive in comparison to other semiconductors and its supply bears little threat of depletion. For these reasons, silicon has been widely researched and therefore has mature refining methods.

Despite these advantages of silicon, finding a suitable material to form a defect-free silicon heterostructure is a difficult task. As can be seen from Figure 1.1, GaP, AlP, and ZnS, do have equivalent lattice constants to that of silicon. The bonding of these semiconductors, however, is polar whereas for silicon the bonding is covalent [2]. This variation in bonding causes these two semiconductors to be non-ideal heterojunction materials due to separation of the polar material into anti-phase domains.

To fabricate silicon-based heterostructure devices, junctions of silicon and silicon-germanium alloy have been heavily researched in recent years in order to determine their optical and electronic properties for potential device applications [2], [3], [4]. Alloying germanium with silicon reduces the bandgap below that of silicon and permits the fabrication of devices such as heterojunction bipolar transistors (HBTs) and modulation doped field effect transistors (MODFETs). By keeping the concentration of germanium low relative to silicon, devices such as the HBT have been fabricated [5], [6]. The incorporation of germanium into a silicon lattice reduces the alloy bandgap relative to silicon as a result of compressive strain and

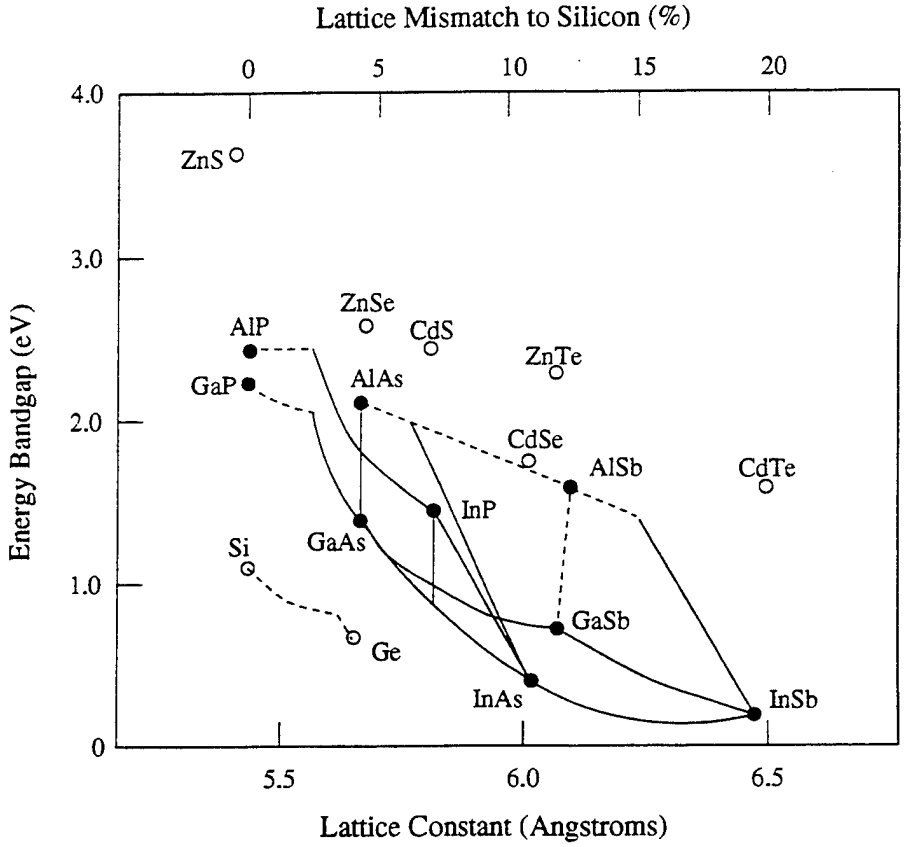

Figure 1.1: Plot of semiconductor lattice constant vs. minimum bandgap.

the smaller energy gap of germanium. Above some critical thickness, however, the strain of the alloy is overcome by defect formations. To minimize the amount of defects at the heterojunction union, the degree of lattice mismatch within the heterojunction must be minimized. In order to minimize the lattice mismatch, the amount of germanium that can be present in the lattice must be constrained. On the other hand, sufficient concentrations of germanium must be incorporated into the silicon lattice to effectively reduce the bandgap and produce the desired carrier confinement and carrier injection characteristic of heterostructures.

The larger atomic radius of germanium with respect to silicon increases the lattice constant of the alloy and produces compressive stress. Carbon, however, can be added to silicon-germanium to compensate for the crowded germanium atoms and form a ternary alloy. Theoretically, a range of compositions should exist where the sizes of the large germanium and small carbon atoms offset one another to maintain the silicon lattice constant. One approach to determining the critical composition of the alloy is to use a linear approximation called Vegard's Law. Vegard's Law assumes that the lattice constant of an alloy linearly depends on its composition. Given the lattice constants of silicon, $a_{Si} = 5.4307$ Å, germanium, $a_{Ge} = 5.6575$ Å, and carbon, $a_C = 3.5597$ Å [7], the germanium to carbon composition ratio predicted for silicon lattice matching is,

$$a_{Si} = a_{Ge}x_{Ge} + a_C x_C \tag{1.1}$$

$$\text{where, } x_C = [a_{Ge} - a_{Si}]/[a_{Ge} - a_C]$$

$$\text{Therefore, } x_C = 0.108 \text{ and } x_{Ge} = 0.892$$

$$\frac{x_{Ge}}{x_C} = 8.2 \tag{1.2}$$

This matching ratio corresponds to a composition of $Ge_{0.892}C_{0.108}$ for no silicon

present within the alloy or, more generally, $Si_xGe_{(1-x)0.892}C_{(1-x)0.108}$ for x amount of silicon within the alloy.

Not only does the carbon reduce the lattice constant of the SiGe alloy, but it may also increase the alloy's bandgap energy by reducing the strain and by the addition of a high energy gap element to the alloy. By incorporating an appropriate amount of carbon into a SiGe lattice structure, a new ternary alloy should form with a lattice parameter approximating that of silicon, 5.43 Å, and a bandgap energy that may differ from that of silicon, 1.11 eV [7]. The bandgap of SiGeC has been theoretically predicted [8], [9], but no comprehensive experimental study has yet been reported.

1.3 Growth by Molecular Beam Epitaxy

Initial reports concerning SiGeC have described ternary amorphous alloys grown by Chemical Vapor Deposition (CVD) [10], [11], [12]. With increasing interests in the alloy, other fabrication techniques resulting in crystalline material were employed. Such techniques have included Solid Phase Epitaxy, or simply ion implantation, [13], [14], [15] and Molecular Beam Epitaxy (MBE) [16]. Although all growth techniques have arguable advantages and disadvantages, MBE offers high growth controllability with low levels of unintentional background impurity doping. These advantages are a result of the low growth temperatures and the ultra-high vacuum environment inherent to MBE. Low growth temperatures can be utilized since MBE is a far-from-equilibtium growth technique which allows growth of compounds away from the equilibrium condition. A low growth temperature would typically imply poor quality or high impurity levels; however, the extremely low background pressure of MBE allows a net increase in growth quality. Unfortunately, limitations exist as to the minimum substrate temperature for acceptable epitaxial growth. From silicon MBE crystal growth theory, the substrate temperature must be at least one third the melting temperature of the source; otherwise, adatoms do not

possess the required mobility to form a single-crystal structure [17]. Likewise, too high a substrate temperature can also result in poor epitaxial growth since inter-diffusion of junctions and out-diffusion of the substrate may occur. In comparison with ion implantation techniques, MBE incorporates all alloy source elements during growth and therefore the structural damage occurring with Solid Phase Epitaxy can be eliminated. In summary, based on the above comparisons, molecular beam epitaxy appears to be a promising method for the growth of the new ternary alloy, SiGeC.

1.4 Project Goals

A complete investigation into the SiGeC ternary alloy system, could require years of research within the related fields of Materials Science and Electrical Engineering. In general, this is the case with all new material systems since a great deal of characterization and growth optimization needs to be performed before potential devices may become a reality. Research of a new material system can be grouped within one of three categories: crystal growth; material properties and characterization; and device applications. Work on the SiGeC alloy began only recently at the University of Delaware and the immediate research goals have encompassed the growth and characterization of the ternary alloy.

The first goal of the project entailed calibration of the newly built MBE system and evaluation of the elemental sources used for growth. Additional research included investigation into innovative carbon and silicon growth techniques so that a better understanding of the growth of the SiGeC alloy could be achieved. Investigations included analysis of the silicon source purity and the carbon deposition cracking pattern. Growth optimization of the alloy was required and involved growth rate determination and observations of morphology and crystallinity versus variations in growth temperatures. While optimizing the growth, characterization of the epitaxial layers was required in order to gain insight into the material properties

at various growth conditions. Characterization included structural and compositional analysis as well as electronic and optoelectronic properties. After consistent and satisfactory growth of crystalline SiGeC has been achieved, potential device applications may then be experimentally researched.

Chapter 2

THE MBE GROWTH SYSTEM

2.1 Introduction to MBE

MBE involves the transportation of atoms, molecules or ions within a beam produced by excitation of an elemental or molecular source. In general, this elemental source could be of gaseous or solid form and would require differing growth conditions depending upon the source type and material being grown. A heated substrate is aligned so as to intercept the molecular beam and a resulting epitaxial layer is formed through impingement and migration of the adsorbed atoms or adatoms. The temperature of the substrate plays a crucial role in the success of the crystal growth and must be chosen for the particular growth method and semiconductors involved. For example, in gas-source MBE, where the chamber pressure during growth is quite high, a large substrate temperature is required in order to minimize impurities. With solid-source MBE, the chamber pressure is extremely low, usually on the order of 10^{-11} to 10^{-10} Torr, and therefore the substrate temperature can be lowered significantly. Solid-source MBE has been the only technique utilized throughout the duration of this project and will therefore be exclusively discussed.

As previously mentioned, a molecular beam is formed through the excitement of an elemental source. For solid-source MBE, the energy of the beam may be a result of thermal excitation or electron bombardment [e-beam]. In order to avoid the electronic defects that have been widely associated with e-beam evaporation, thermal evaporation sources have been utilized for the growth of the group IV alloys.

2.2 System Description

A drawing of the MBE system used for the fabrication of the group IV alloys has been included in Figure 2.1 for reference.

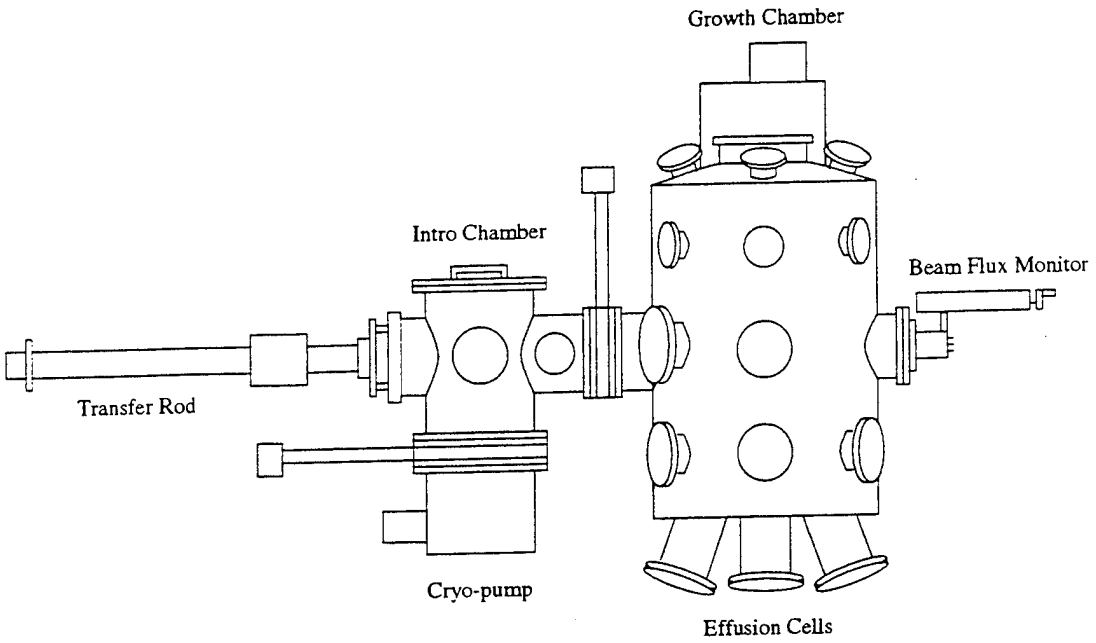

Figure 2.1: Molecular Beam Epitaxy system

The MBE unit is a custom made, dual chamber system designed by J. Kolodzey [Electrical Engineering Department, University of Delaware] and manufactured by EPI Chorus Corporation in St. Paul, Minnesota. The main and introduction chambers are separated by a pneumatically controlled gate valve so that introduction and removal of a sample is possible with minimal disruption to the growth chamber pressure. Vacuum is maintained in the two chambers by two CTI high vacuum cryopumps which typically produce background pressures of 10^{-10} and 10^{-9} Torr in the Growth and Intro chambers respectively. Unfortunately, the cryopumps do not function efficiently at high pressures, therefore, initial evacuation of the chambers is required. Three molecular sieve sorption pumps are used to produce vacuum pressures as low as 10^{-4} Torr. Once vacuum pressures of 10^{-3} Torr are

obtained with the initial roughing, the cryopumps may be activated. A cryoshield just inside the main chamber is supplied with a constant flow of chilled water. The shield serves to cool the internal chamber surfaces and prevents any outgassing of the stainless steel portions that are heated by the nearby effusion cells. In most MBE systems, liquid nitrogen is passed through the vanes of this shield located just inside the chamber walls. Unfortunately, when the shield is lowered to liquid nitrogen temperatures the silicon that builds up along the walls of this shield may flake. In order to reduce the flaking, a constant flow of glycol chilled water is passed through the shroud and prevents the temperature cycles that may otherwise cause deposits to flake off.

Unlike ion pumps, the cryopumps do not indicate the chamber pressure. The chamber pressure must be monitored by separate vacuum gauges. The gauges presently used on the MBE system include convectrons [GV270], ion gauges [Granville Phillips], and a Residual Gas Analyzer (RGA) [Spectra]. The convectrons are used to monitor the Intro chamber and roughing line pressures following venting of the system. They provide readings at relatively high pressures specifically $9x10^{2}$ to 10^{-4} Torr. The ion gauges, on the other hand, measure much lower pressures ranging from 10^{-5} to 10^{-11} Torr. After evacuation of the system to below 10^{-6} Torr, the RGA can determine partial pressures of the residual gases within the chamber. The output of the instrument is presented as pressure intensities versus atomic mass units. The displayed partial pressures can be compared with internal memory files to reveal the identities of the unknown gases. An RGA is advantageous since an unusually high pressure source, such as air leaks or excess water, can be identified.

The gauges mentioned are primarily used to measure background pressures of the chamber. During growth, the beam-equivalent pressure is measured by a beam flux monitor (BFM) which has a shield that serves as the main shutter for the substrate. The BFM consists of a nude ion gauge attached to a retractable

arm. During growth the gauge is moved within the path of the molecular beam and the shield prevents the impingement of any material onto the substrate surface. By opening and closing the source shutter, a variation in pressure can be measured and a resulting source flux can be obtained.

The sources are located on the underside of the growth chamber so that the molecules or atoms rise vertically toward the substrate. Six ports are available on the chamber and are designated for silicon, germanium, carbon, erbium, boron, and antimony cells. Presently only three of these cells are in operation: silicon, germanium, and carbon. These three cells will be discussed in further detail elsewhere.

A three inch diameter substrate is held in place by a manipulator capable of rotating the substrate at a desired rate. Rotation of the substrate is necessary to insure uniform epitaxial growth. Without rotation, the epitaxial films would have varying thicknesses and compositions across the substrate. In addition to rotation, the manipulator heater allows substrate heating up to 1100°C. The heat is generated by current through a tungsten filament residing in close proximity to the substrate. Water cooling prevents excess heating of the manipulator assembly and its electronics. The substrate's temperature is controlled by a thermocouple near the substrate. Although the thermocouple does not contact the surface of the growing film directly, its voltage output is empirically related to the surface temperature of the substrate. In addition to the thermocouple, the growth temperature is monitored by an optical pyrometer located at the base of the chamber. Again, this technique is not absolute, but it can be used to provide a repeatable empirical growth temperature and therefore a basis upon which the epitaxial growth temperatures can be compared.

2.3 Elemental Source Description

2.3.1 Silicon Cell Description

In previous solid-source MBE, silicon growth has been almost exclusively performed by electron-beam bombardment of a silicon target. Silicon Knudsen cells

have been less commonly used since thermal evaporation of silicon from standard crucible materials can produce crucible decomposition at silicon evaporation temperatures. If a crucible is subject to decomposition at source growth temperatures, unintended impurity doping may result. With the development of a new experimental ceramic crucible, however, thermally evaporated silicon growth may now be possible.

Silicon epitaxial growth has been investigated utilizing a new high temperature effusion cell with an EPI proprietary ceramic crucible. Within the cell, a tungsten filament is heated by passing current through electrical feedthroughs mounted at the base of the cell. The tungsten filament heats a conical crucible which contains the source material. The temperature of the crucible is measured using a thermocouple that is mounted close to the cell filament. The output of the thermocouple is monitored by a temperature controller which supplies the current to the cell. The controller compares the cell temperature as measured by the thermocouple to a specified set point temperature, and adjusts the filament current accordingly.

Since silicon has a relatively high melting point, 1414°C, a material of an exceedingly high melting temperature must be chosen for the crucible. Initially, a standard pyrolitic graphite crucible was used in the silicon cell. Epitaxial growth of silicon was attempted at temperatures of 1650°C and 1675°C; however, no evidence of growth could be found. Thermal evaporation of the silicon source required that the crucible be heated above its recommended temperature limit of 1700°C. Growth at these temperatures would result in crucible decomposition and was therefore not investigated. Instead, an experimental ceramic crucible, developed by EPI, was installed and utilized for all subsequent silicon growth layers.

2.3.2 Germanium Cell Description

Germanium is grown by means of thermal evaporation from a standard effusion cell [EPI]. Since the melting point of germanium, 937°C, is much lower than

that of silicon, a high temperature cell was not required. Growth of germanium was performed using a standard effusion cell with a pyrolitic boron nitride (PBN) crucible. As a precaution, the source temperature during germanium growth was kept below 1500°C in order to avoid unwanted impurity doping caused by crucible decomposition. Since adequate growth rates of germanium were obtained from source temperatures well below the crucible limit, this restriction never needed to be challenged.

2.3.3 Carbon Cell Description

Due to the exceedingly low vapor pressure of carbon, epitaxial growth with a conventional Knudsen cell is not possible. Furthermore, in the interest of keeping the MBE system solid source, acetylene gas was not used. Motivated by the success of R. Malik for carbon doping of GaAs [18], thermal evaporation of carbon was performed by resistively heating a high purity graphite filament. Depending upon the filament used, current ranging from 35 to 54 Amperes was used to heat the filament to temperatures approximating 2000°C. Based on Malik's work, EPI developed a carbon evaporation cell which used two individual filament designs: the "S" shaped filament and the Serpentine filament [19]. After using both filaments to fabricate several germanium-carbon alloy layers, the filament designs were evaluated. The design of the serpentine filament exhibited definite advantages over the design of "S" shaped filament. Due to the smaller surface area and smaller resistance of the "S" shaped filament, a higher current was needed to obtain the necessary filament temperatures for carbon growth. The smaller surface area also caused a reduction in the growth rate and lifetime of the filament. The majority of the carbon growths were therefore performed using the serpentine rather than "S" shaped filament. After compositional analysis of several carbon rich layers that had been grown using the serpentine filament, the purity of the EPI filament material became questionable. A third filament was therefore designed using high quality pyrolitic graphite

[Union Carbide] that was recommended by S. Iyer [IBM, T.J. Watson]. The filament shape was optimized for maximum surface area and maximum growth rate. The final design is indicated in Figure 2.2.

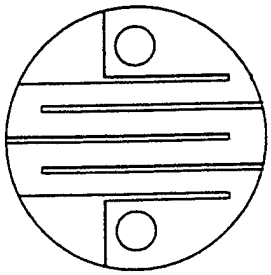

Figure 2.2: WWR carbon filament design

Two filaments of the above configuration were machined by W. Rule [Electrical Engineering Department, University of Delaware] and have yet to be tested during actual growth. Extensive analysis on the filament purity and growth mechanisms has been performed. The analysis demonstrated noticeable improvements in filament purity upon comparison of the "S" Shaped and serpentine designs.

2.4 System and Source Purity

In MBE, the quality of the epitaxial layers greatly depends upon the purity of the system and the individual sources. Any interior surface of the vacuum chamber must be impurity free, all sources must be baked-out, and the source materials must be etched prior to installation. Additional precautions, such as additional RGA and compositional analysis, were needed with the non-traditional carbon and silicon sources in order to insure low impurity level growth.

2.4.1 Silicon Purity

High quality source material was chosen for each cell. The silicon source utilized high resistivity silicon wafers [SI-TECH, Inc.] as specified by Table 2.1.

Table 2.1: Silicon source material specifications

Silicon Source	
Original Manufacturer	Wacker
Lot Number	42T000
Growth Method/Grade	Float Zone/Test
Type/Dopant	p-type/Boron
Resistivity	5950-11050 ohm-cm

Although the bulk regions of a source material may be high in purity, oxides and various contaminants often reside on the material's outer surfaces; therefore, the material must be etched prior to installation. As recommended by S. Iyer [IBM, T.J. Watson], the following procedure was used.

Table 2.2: Silicon source etching procedure

Silicon Etch	
Boil in tri-chloro-ethylene	10 minutes
Boil in acetone	10 minutes
Boil in methanol	10 minutes
Submerge in 1:15:5 $HF:HNO_3:CH_3COOH$	3 minutes
Submerge in DI	1 minute
Submerge in 1:15:5 $HF:HNO_3:CH_3COOH$	3 minutes
Submerge in DI	1 minute
N_2 blow dry	———

Since slicing a semiconductor ingot into wafer form can add impurities to the surface of the material, initial degreasing of the wafers with organic solvents was required before etching. The etch rate for the concentrations given in the acid step of Table 2.2 were estimated by S. Iyer at five microns per minute.

In addition to the source material, the effusion cell and crucible must also be contaminant free so that outgassing will not occur at elevated temperatures. Since

finding a crucible material that is stable at the high silicon evaporation temperatures is a difficult task, the experimental crucible developed by EPI was carefully tested prior to any silicon growth. The crucible was subjected to an extensive bake-out procedure and inspected for gaseous emissions at elevated temperatures. The crucible was raised to a maximum cell temperature of 2000°C and held for a total of 6 hours. Two test growths of silicon on silicon substrates were performed at 1800°C and 1930°C respectively. The layer grown at 1930°C was sent to Phillip Thompson at Naval Research Laboratory for impurity level compositional analysis by Secondary Ion Mass Spectrometry (SIMS). Due to a lack of standard samples. quantitative analysis could not be performed on the epitaxial layer. The depth profiling results, however, did demonstrate high levels of titanium and boron that exceeded what Thompson would consider normal background levels.

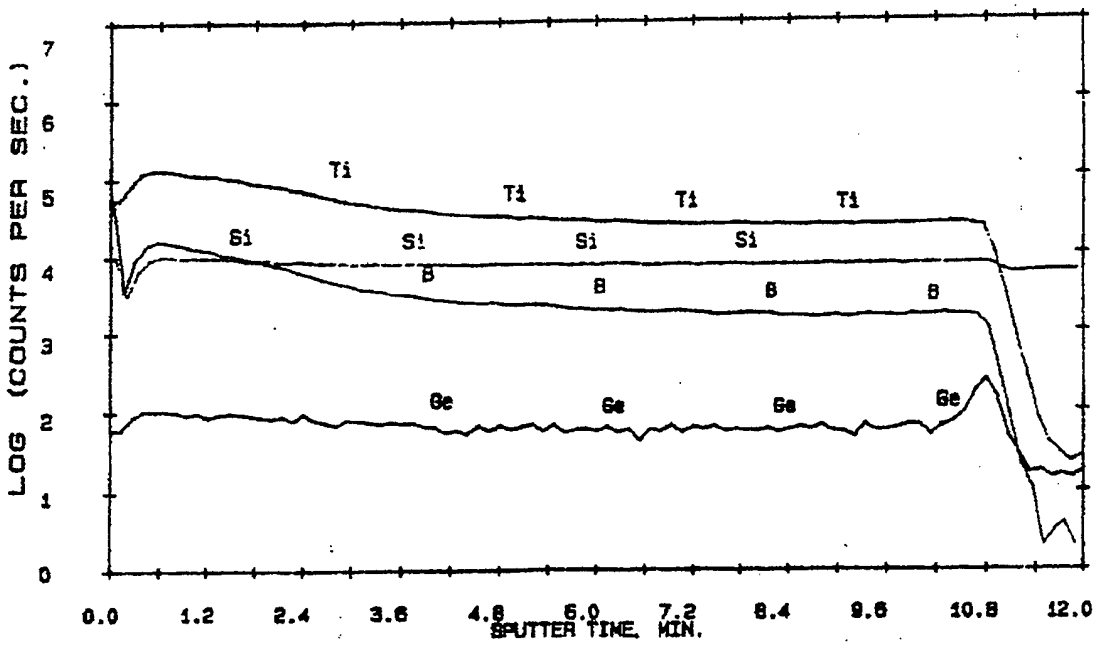

Figure 2.3: SIMS analysis (a) of silicon grown at 1930°C

In addition to titanium and boron impurities, copper, zinc, and germanium were all detected but at less significant levels.

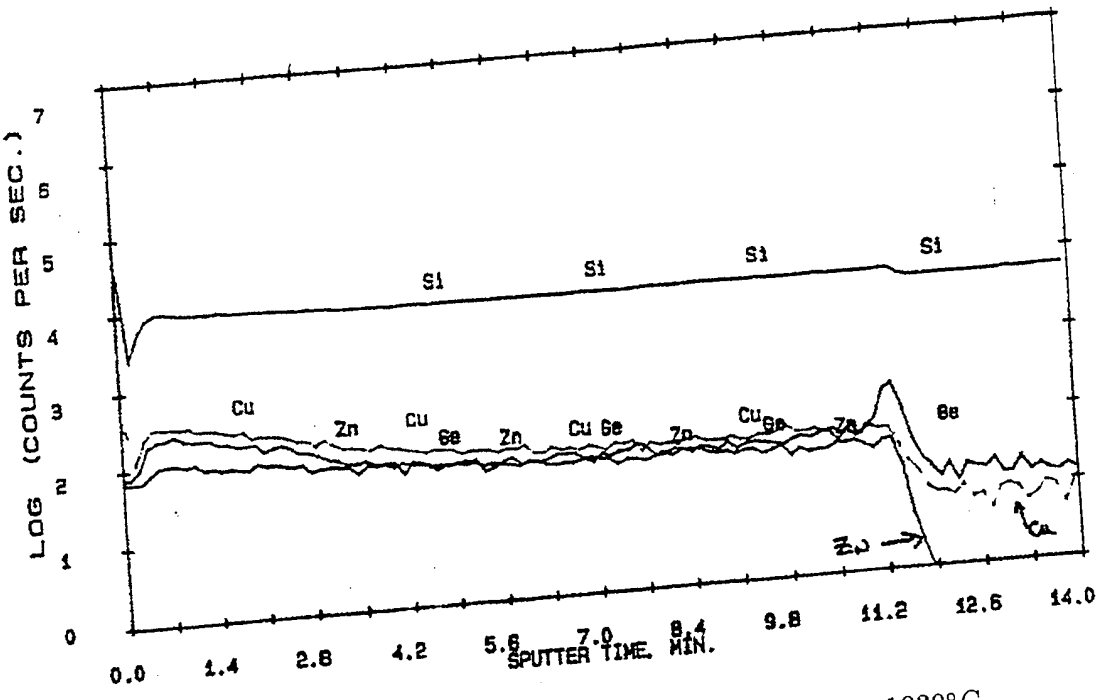

Figure 2.4: SIMS analysis (b) of silicon grown at 1930°C

These results indicate that crucible decomposition does occur at temperatures in excess of 1930°C; therefore, future silicon growth should be limited to temperatures below 1930°C.

2.4.2 Germanium Purity

A boule of intrinsic germanium was purchased from Eagle-Picher Industries, Inc, for use in the germanium Knudsen cell. The germanium, lot number E-327, had been zone-refined to a purity of at least 99.9999 percent. To remove surface contaminants, the germanium was etched using the procedure in Table 2.3.

Unlike the silicon source, the germanium was a solid ingot; therefore, initial degreasing by organic solvents was not required. As noted in Table 2.3, a more acidic solution was used for the second etch.

As previously mentioned, a more standard effusion cell crucible, a pyrolitic boron-nitride (PBN) crucible, was used for the evaporation of germanium. The

Table 2.3: Germanium source etching procedure

Germanium Etch	
Submerge in 1:15:5 HF:HNO_3:CH_3COOH	2 minutes
Submerge in DI	1 minute
Submerge in 5:15:7 HF:HNO_3:CH_3COOH	3 minutes
Submerge in DI	1 minute
N_2 blow dry	

crucible was baked-out up to 1580°C prior to the installation of the germanium source. Due to the low growth temperature of germanium relative to that of silicon. additional analysis indicating any crucible decontamination was not performed.

2.4.3 Carbon Purity

As mentioned previously, the growth characteristics and purity of three different carbon filament designs were investigated. In summary, the initial filament used for carbon growth, the "S" shaped filament, was proven undesirable due to a short filament lifetime and a low carbon growth rate. An improved filament, the serpentine filament, utilized the same graphite material but incorporated a larger surface area for an increased growth rate. Unfortunately, the purity of the graphite used in both of these filaments became questionable when compositional analysis showed oxygen incorporation into the epitaxial layers. The oxygen was detected by Rutherford Backscattering Spectrometry (RBS) and was measured at levels equalling as much as one third the amount of carbon within the layer. For further study, the Residual Gas Analyzer (RGA) was placed in the Intro-chamber within a direct line projection with the serpentine filament. Gaseous emissions were monitored over increasing filament current and the partial pressures were recorded. With increases in the serpentine filament current, the RGA measured increases in the emission levels of carbon monoxide, carbon dioxide, acetylene, and ethane. Ideally, only carbon atoms

or molecules should have been emitted from the filament. In order to minimize the amount of gaseous emissions, a third filament (WWR filament) was designed and developed from high quality Union Carbide graphite. Surface contaminants were removed by etching the filament in an Aqua Regia solution.

Table 2.4: Graphite etch procedure used for WWR filament

Carbon Etch	
Boil in tri-chloro-ethylene	5 minutes
Boil in acetone	5 minutes
Boil in methanol	5 minutes
Rinse in de-ionized water (DI)	30 seconds
Submerge in 3:1 $HCl:HNO_3$	5 minutes
Rinse in de-ionized water (DI)	30 seconds
Boil in DI	45 minutes
Boil in DI	45 minutes
Place on hot plate (low heat)	15 minutes

Emission analysis of the WWR filament was repeated using the RGA as previously described with the serpentine filament. The WWR filament demonstrated reduced carbon monoxide, acetylene, and ethane emissions at temperatures comparable to those used during the analysis of the serpentine filament. The partial pressures of the gaseous emissions are provided in a later chapter in which more extensive analysis of the graphite filament evaporation is discussed. Carbon growth has not yet been performed with the new WWR filament design; however, reduced oxygen incorporation into the epitaxial layers is expected.

2.4.4 Substrate Cleaning

The surface of the substrate intended for epitaxial growth can act as a major source of epilayer contamination. A great deal of research has been performed within the scientific community towards finding an optimum silicon substrate cleaning procedure [20], [21]. Past techniques have suggested: etching the surface clean, capping

the surface with a protective oxide, and then in-situ desorption of the oxide at high temperatures. Unfortunately, the high temperatures required for oxide desorption can often result in impurity diffusion, dislocations, and slip lines [20]. An alternative solution to applying the protective oxide involves the termination of the substrate surface with hydrogen [21]. The hydrogen atoms bond to the dangling silicon bonds that remain on the substrate surface after etching and prevent the adsorption of impurities and contaminants. Since the hydrogen passivation layer can be desorbed at much lower temperatures than the previously used oxide, impurity diffusion and defect formation can be reduced.

The substrate is terminated with hydrogen by finalizing the cleaning procedure with an HF dip. The substrate cleaning procedure utilized prior to all epitaxial growth has been provided in Table 2.5.

Table 2.5: Substrate cleaning procedure

Substrate Cleaning		
Boil in tri-chloro-ethylene	5 to 10 minutes	Wax Removal
Boil in acetone	5 to 10 minutes	Degreaser
Boil in methanol	5 to 10 minutes	Degreaser
Rinse in de-ionized water (DI)	30 seconds	———
Boil in DI with 2 percent FL-70 detergent	10 minutes	Degreaser
Boil in DI	20 minutes	———
Submerge in warm 5:3:3 DI:HCl:H_2O_2	5 minutes	Etchant
Submerge in DI	1 minute	———
Submerge in DI	1 minute	———
Submerge in 10:1 DI:HF	1 minute	H Passivation

Chapter 3

GROWTH OF GROUP IV ALLOYS

In order to obtain samples for material analysis and the determination of growth rates, epitaxial layers of varying material type, composition, and growth conditions have been produced with the MBE system. Growth condition optimization and compositional analysis has been reserved for future discussion in subsequent chapters; however, the conditions present during each sample growth and the determination of element growths rates are to follow. Growth rates were used for compositional analysis since flux measurements from the beam flux monitor were not avalible for silicon and carbon. In addition to sample growth analysis, investigation of carbon emission from a heated filament has been performed in order to determine the dominant molecular species emitted during carbon growth.

3.1 Growth Conditions

Sample growth has been performed using certain combinations of all three active sources, silicon, germanium, and carbon, to form alloyed epitaxial layers. Presently, all growths are categorized into one of four material types: silicon, germanium, germanium-carbon, or silicon germanium-carbon. The epitaxial layers were grown on 3 inch (76.2 mm) silicon (100) substrates having the specifications given in Tables 3.1 through 3.3.

Table 3.1: Silicon substrate specifications for the samples identified as SGC-1 through SGC-21

Silicon Substrate	
Original Manufacturer	Unisil
Lot Number	106604-3
Growth Method/Grade	CZ/Test
Type	n-type
Dopant	Phosphorus
Resistivity	1-10 ohm-cm
Thickness	13-17 mil

Table 3.2: Silicon substrate specifications for the sample identified as SGC-22

Silicon Substrate	
Original Manufacturer	Unisil
Lot Number	10685
Growth Method/Grade	CZ/Test
Type	p-type
Dopant	Boron
Resistivity	1-10 ohm-cm
Thickness	13-17 mil

Table 3.3: Silicon substrate specifications for the samples identified as SGC-23 through SGC-32

Silicon Substrate	
Original Manufacturer	Unisil
Lot Number	10701
Growth Method/Grade	CZ/Test
Type	n-type
Dopant	Phosphorus
Resistivity	1-2 ohm-cm
Thickness	18-22 mil

3.1.1 Silicon Growth

Only two silicon layers, SGC-12 and SGC-13, were successfully grown. These samples were used for purity analysis of the cell crucible and for determination of the silicon growth rate. The growth conditions for both samples have been provided in Table 3.4.

Table 3.4: Silicon growth conditions

Silicon Growth					
Sample Number	Substrate Temp. (°C)	Silicon Temp. (°C)	Time (hours)	Thickness μm	Growth Rate μm/hr.
SGC-12	700	1800°C	2.0	0.098	0.049
SGC-13	700	1930°C	2.5	0.298	0.119

3.1.2 Germanium Growth

Due to the ease of germanium growth with a standard Knudsen effusion cell, many samples of varying growth conditions were obtained. The growth conditions for all germanium epitaxial layers are provided in Table 3.5. From these conditions growth rate versus cell temperature was determined as well as the growth effects of a varying substrate temperature. Growth characterization and conclusions concerning the growth conditions will be discussed in a later chapter.

After several growths, the germanium cell's thermocouple became inoperable causing the source temperature to become unknown. Estimations of the germanium growth temperature by means other than the cell's thermocouple were therefore required. A constant cell filament current near 8.22 amps was used for subsequent growths. This current was believed to produce germanium source temperatures near 1350 to 1375°C. Since, however, an equivalent thermocouple temperature could not be precisely determined, the germanium growth rates calculated prior to the cell malfunction could not be used to accurately determine alloy composition. The

Table 3.5: Germanium growth conditions

Germanium Growth					
Sample Number	Substrate Temp. (°C)	Germanium Cell	Time (hours)	Thickness μm	Growth Rate μm/hr.
SGC-04	500	1350°C	3	0.153	0.051
SGC-05	500	1450°C	3	0.908	0.303
SGC-10	500	1350°C	6	0.444	0.073
SGC-14	800	1350°C	3	0.639	0.213
SGC-15	700	I=8.22 A	3	0.527	0.176
SGC-16	400	I=8.22 A	3	0.544	0.181
SGC-25	300	I=8.23 A	3	0.518	0.173
SGC-26	600	I=8.23 A	3	0.520	0.173

problem with the germanium cell was later determined to be the result of a cracked crucible which caused a malfunction in the temperature control of the cell. It was also realized that the cracked crucible may not have produced constant germanium flux, even with a constant current.

3.1.3 Germanium-Carbon Alloy Growth

For the growth of germanium-carbon, a thin germanium buffer layer was initially deposited to assist nucleation of carbon containing layers. A silicon buffer layer would have been preferred since the alloy was to be lattice matched to silicon rather than germanium; however, the silicon source was not operational during the majority of the growths. All but two of the alloy growths included a 10 to 15 minute, approximately 125 to 200 Å, germanium buffer layer which was grown at a 400°C substrate temperature. SGC-17 and SGC-21 included a thicker germanium buffer layer, approximately 760 Å, grown for 1 hour. In Table 3.6, the growth conditions for all germanium-carbon alloy layers grown with the serpentine graphite filament are provided. Germanium-carbon growth rates have not been included since it is a function of the individual element growth rates.

Table 3.6: Germanium-carbon alloy growth conditions

Germanium-Carbon						
Sample Number	Substrate Temp. (°C)	Ge Cell (T or I)	C Current (Amps)	C Temp. (°C)	Time (hrs.)	Thickness μm
SGC-11	500	1325°C	40	2091	2.50	0.153
SGC-17	400	8.22 A	36	1970	4.00	0.908
SGC-18	400	8.24 A	37	2001	3.25	0.444
SGC-21	400	8.27 A	35	1939	4.00	0.639
SGC-23	600	8.22 A	37	2001	3.25	0.527
SGC-24	600	8.22 A	36	1970	3.25	0.544
SGC-27	600	8.23 A	35	1939	3.25	0.518
SGC-28	700	8.23 A	37	2001	3.25	0.520
SGC-29	700	8.23 A	38	2031	3.25	—
SGC-30	600	8.23 A	38	2031	3.25	0.582
SGC-31	600	7.80 A	38	2031	3.25	0.139
SGC-32	500	7.80 A	38	2031	3.25	0.136

3.1.4 Silicon-Germanium-Carbon Growth

Two silicon-germanium-carbon samples were grown with the intent of varying the carbon concentration. Based on the success of pure germanium growth at a substrate temperature of 400°C, growth of the ternary alloy was attempted at this temperature. Using growth rate data, the source temperatures and currents were specifically chosen in order to produce an alloy composition of approximately $Si_{.50}Ge_{.45}C_{.05}$. Growing a silicon-germanium-carbon alloy of this composition would theoretically produce a silicon latticed matched alloy. Malfunctions with the germanium cell and minimal source material within silicon the cell caused large compositional deviations from the predicted values. Based on the determined elemental growth rates, however, future growths should be performed at similar silicon and germanium source temperatures but at higher carbon currents. The growth conditions of the two ternary alloy layers have been provided in Table 3.7.

Table 3.7: Silicon-germanium-carbon alloy growth conditions

Silicon-Germanium-Carbon							
Sample Number	Subst. Temp.	Si Temp.	Ge Current	Carbon Current	Carbon Temp.	Time (hrs.)	Thickness μm
SGC-19	400°C	1870°C	8.20 A	36 A	1970°C	3.25	0.488
SGC-20	400°C	1870°C	8.24 A	35 A	1939°C	3.25	0.474

All reported germanium-carbon and silicon-germanium-carbon growths, utilized the serpentine carbon filament design.

3.2 Determination of Growth Rates

In order to produce an alloy of a desired composition, the growth rate versus temperature characteristics for each element must be known. For elements such as silicon and germanium, the growth rate is relatively simple to obtain since single component layers may be epitaxially grown. The growth rate for a specific source temperature may be calculated by measuring the thickness of the layer and then dividing it by the duration of the epitaxial growth. For elements such as carbon, which was not used to grow independent epitaxial layers, the layer thickness must incorporate more than one element and therefore another technique for measuring growth rate was employed. Typical growth rates for the more commonly grown elements, silicon and germanium, have been reported within the range of 0.36 to 1.80 μm/hr. (1 to 5 Å/s) [17], [22].

Since growth rate calculations depended upon the epitaxial layer thickness, an accurate method for determining the growth thickness was required. All thickness measurements were made by Suibin Zhang utilizing the Sloan Angstrommeter at the Institute for Energy Conversion, courtesy of Dr. Robert W. Birkmire, Director. An Angstrommeter measures a step height from the interference fringes produced at a step in layer thickness. Fringes are areas of destruction and reinforcement of

light through interference of multiple beams. The sharpness of the fringes which distinguish these interference regions strongly depend on the number of light beams utilized. The fewer the number of beams contributing to inference, the less sharp the fringe pattern. For this reason multiple beams are employed. After slightly tilting the sample, fringes occur every one-half wavelength of the incident light. Since the Angstrommeter used sodium light, this distance corresponded to 2945 Å; therefore, the fringe to fringe spacing viewed on the sample, represents a change in tilt height of 2945 Å. When a step is reached on the surface of the sample, the fringes will deflect a distance proportional to the step height and related to the fringe spacing. A step height can therefore be obtained from a photograph of the fringe pattern and calculation of Equation (3.1).

$$\frac{A}{B} = \frac{2945\text{Å}}{\text{x}} \tag{3.1}$$

where,

A = Measured distance between fringes as obtained from photograph

B = Measured distance of fringe displacement as obtained from photograph

2945 Å = Sample height between fringes

x = Step height.

Figure 3.1 illustrates the fringe pattern of a sample step height as would be observed through the Sloan Angstrommeter.

Once the growth rate of an element at a specific temperature is known, a trend displaying growth rates for all temperatures can easily be obtained. The growth rate of a material should theoretically follow its vapor pressure; therefore, the growth rate of a material at all temperatures can be estimated by shifting the known vapor pressure versus temperature curve to overlay the single experimentally determined growth rate. All subsequent material growth *should* occur at rates that follow the

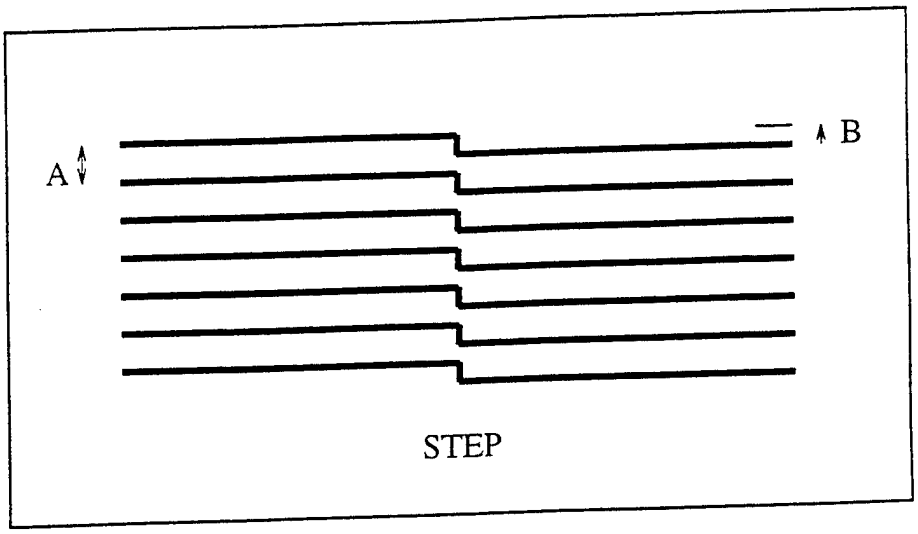

Figure 3.1: Illustration of a fringe pattern used to measure a step height.

theoretical predictions, provided that minimal change occurs in the source growth kinetics over time. Additional growth points, however, can be added to improve the accuracy of the estimated curve.

3.2.1 Growth Rate of Silicon

In order to determine the growth rate of silicon at a specific temperature, an epitaxial layer of silicon was grown at a cell temperature of 1800°C and its thickness was measured. The vapor pressure of silicon versus temperature obtained from EPI reference manuals was plotted and used to determine the theoretical silicon growth rate. An estimated growth rate trend was generated by superimposing the vapor pressure versus temperature trend over the growth rate point measured for 1800°C. A second growth rate data point was found for a silicon source temperature of 1930°C.

As shown in Figure 3.2, the experimentally obtained growth rate, 0.12 μm at 1930°C, was less than the theoretically predicted rate, 0.19 μm. The deviation from the theoretical growth rate at 1930°C can be explained by the following reason. Insufficient silicon charge may have been loaded into the crucible prior to the growth

Table 3.8: Determination of silicon growth rate for a substrate temperature of 700°C

Silicon Growth		
Sample Number	SGC-12	SGC-13
Source Temperature	1800°C	1930°C
Duration	2 hours	2.5 hours
Measured Thickness	0.098 μm	0.298 μm
Growth Rate	0.049 μm/hr.	0.12 μm/hr.

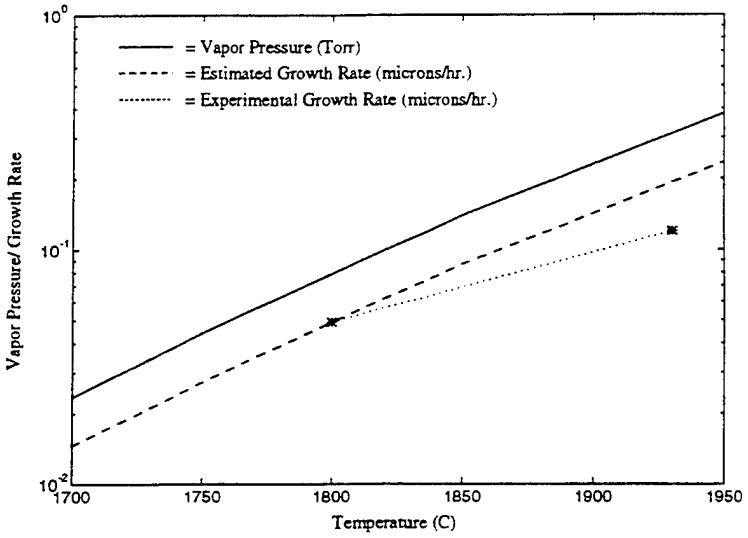

Figure 3.2: Plot of silicon vapor pressure and growth rate. Value of experimental growth rate at 1930° may lie below the estimated value because of source depletion.

of sample SGC-12 and a large percentage of the source material in the crucible may have evaporated during the growth of SGC-12. A decrease in the source material contained in a crucible will produce a decrease in the source surface area and an increase in the beam path length, the length from source to substrate. As a result, the subsequent growths would exhibit different growth kinetics, and specifically, a reduction in growth rate. Since after four growths, SGC 12, 13, 19, and 20, the silicon in the crucible had completely evaporated, significant depletion of the source material prior to SGC-19 may have occurred and is a plausible explanation for the reduced growth rate.

3.2.2 Growth Rate of Germanium

As with silicon, the growth rate of germanium was determined by fitting the germanium vapor pressure trend to the experimental growth rate data points. Three growths of pure germanium were used for the analysis.

Table 3.9: Determination of germanium growth rate for substrate temperature of 500°C

Germanium Growth			
Sample Number	SGC-4	SGC-5	SGC-10
Source Temperature	1350°C	1450°C	1350°C
Duration	3 hours	3 hours	6 hours
Measured Thickness	0.196 μm	0.88 μm	0.458 μm
Growth Rate	0.065 μm/hr.	0.29 μm/hr.	0.076 μm/hr.

As can be seen from Figure 3.3, the three experimental germanium growth rates do follow the vapor pressure trend. Unfortunately, the estimated germanium growth rate curve could not be utilized for reliable germanium compositions during the alloy growths following SGC-11. The thermocouple at the germanium crucible malfunctioned and caused the controller to produce rapid changes in the filament current. The current supply from the controller was still functional and therefore the

cell was controlled directly by the filament current. Since the cell temperature could only be approximated from the current setting, the reproducibility of the growth conditions remained questionable. The fault affecting the temperature control was later determined to be a cracked crucible which allowed molten germanium to leak and damage the thermocouple. As a result, alloys grown during this time had to be compositionally analyzed using carbon growth rates and other analytical techniques since germanium growth rates based on cell current were unreliable.

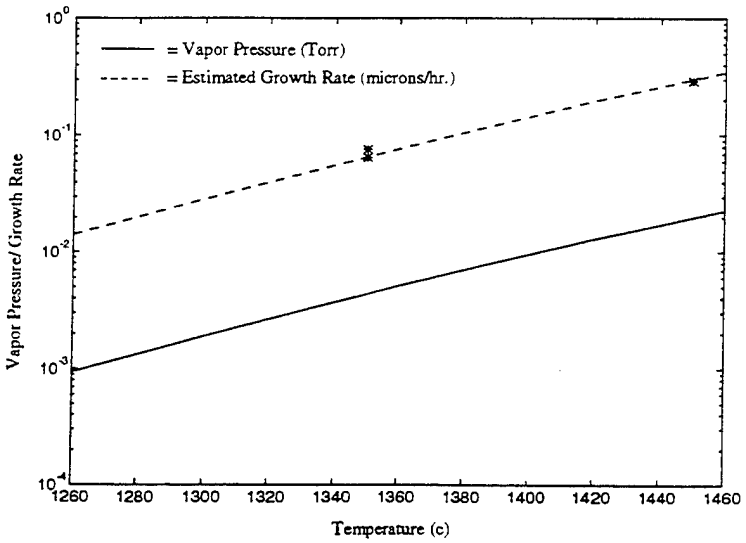

Figure 3.3: Plot of germanium vapor pressure and growth rate.

3.2.3 Growth Rate of Carbon

A pure carbon layer was not grown independently and therefore the carbon growth rate had to be determined by other methods than those previously used for silicon and germanium. Since carbon was grown in an alloy with other elements, the growth rate(s) of the other element(s) may be used to estimate the relative carbon thickness within the alloy. By using this calculated carbon thickness, the growth rate of carbon could be estimated. If the growth rates are not known, however, a

relative carbon thickness can still be determined by measuring the carbon content of the sample. The disadvantage of these techniques is that they assume complete carbon incorporation onto substitutional sites within the lattice. Due to the small size of the carbon atom relative to silicon and germanium, an unknown percentage of carbon within the layer may reside at interstitial rather than substitutional sites. Another disadvantage is that the equivalent thickness of oxygen, an impurity that has been found within the carbon alloys, is not accounted for. The actual carbon thickness would therefore be less than the calculated value. Overall, the alloy must be considered a pure, ideal solid solution for which the effective lattice constant depends linearly on the composition. With these possible errors in mind, substitutional carbon incorporation was assumed when calculating the carbon growth rate.

By Rutherford Backscattering Spectrometry (RBS) the carbon content of two germanium-carbon alloys was measured and a relative carbon thickness was determined. Composition measurements will be discussed in more detail within a later chapter. Upon comparison of the experimental growth rate data points with the carbon vapor pressure, a reasonable trend of estimated growth rates was obtained.

3.2.3.1 Current Vs. Temperature Characteristics

Since the carbon source used for the growth of group IV alloys did not incorporate a thermocouple and controller, direct observation of the filament temperature was not possible. By estimating the filament resistance and surface area from which carbon emission occurred, an approximation of the emission temperature for any filament current could be obtained. From the theory of black body radiation, the resistive power loss of an object can be described by the following relation known as the Stefan-Boltzmann law [7], [18].

$$P = \sigma A T^4 \tag{3.2}$$

Table 3.10: Resistance and surface areas of "S"Shaped, Serpentine, and WWR filaments and a filament published by Malik [18].

Carbon Filament Properties				
Filament Design	"S" Shaped	Serpentine	WWR	Malik
Resistance (ohms)	0.066	0.2	0.56	—
Total Surface Area (cm^2)	0.968	1.806	7.564	—
Top Surface Area (cm^2)	0.484	0.903	3.782	1.000

Where, $\sigma = 5.67 \text{x} 10^{-12}$ Watts$\cdot cm^{-2} \cdot K^{-4}$

$P = I^2R$

A = Surface area

T = Temperature (K)

$$T^4 = \left(\frac{I^2 R}{\sigma A} \right) \tag{3.3}$$

For each of the three filament designs, active region resistances and surface areas were calculated. Using the values described in Table 3.10 and Equation (3.2), the current versus temperature characteristics were determined for each filament. As can be seen in Figure 3.4, the serpentine filament should require the least amount of current to achieve an approximate growth temperature of 2000°C.

3.2.3.2 Estimated Growth Rate Based on Published Data

In order to compare the relative carbon growth rates of the three filament designs and have a basis for which to set the carbon filament current during the initial alloy growths, estimated growth rate trends were produced from published experimental data [18]. Use of these predicted carbon growth rates was discontinued once the actual experimental growth rates for carbon were determined. The estimated growth rates, however, provided a reasonable prediction of the filament growth conditions required for carbon alloy growth. The published data that were

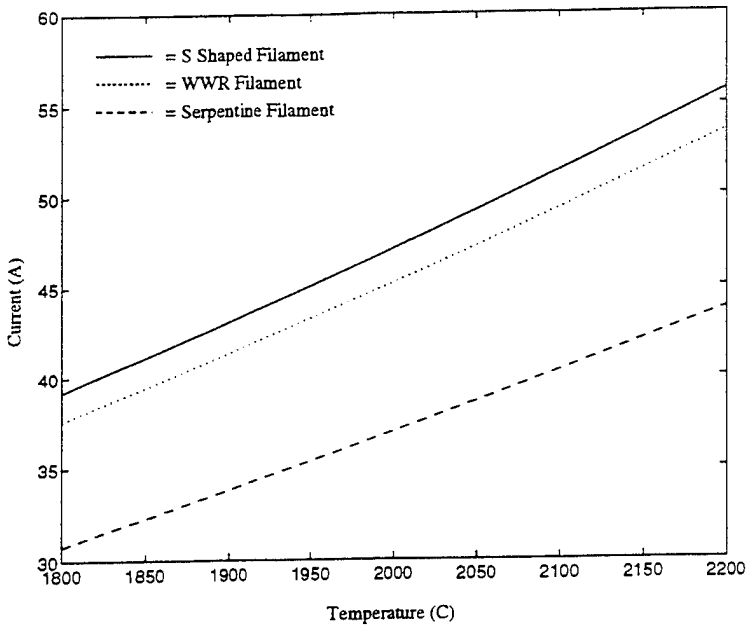

Figure 3.4: Plot of carbon filament current versus temperature.

used for growth rate predictions described the carbon doping concentrations of gallium arsenide for a range of graphite strip currents as shown in Figure 3.5.

Malik estimated a carbon source temperature of 2150 K when 21 Amps was driven through the filament to produce a carbon doping concentration of 10^{19} cm^{-3}. This estimate was made using the Stefan-Boltzmann law, equation 3.2, and carbon vapor pressure data. Complete conversion of the filament current into its equivalent source temperature was performed using the "2150 K @ 21 Amps" data point and the Stefan-Boltzmann law of Equation (3.2) to yield,

$$(2150)^4 = \left(\frac{21^2\ R}{\sigma\ A}\right), \tag{3.4}$$

or

$$\frac{R}{\sigma\ A} = 4.845\text{x}10^{10}. \tag{3.5}$$

Substituting Equation (3.5) into Equation (3.3) yields

$$T = \left(I^2\ 4.845\text{x}10^{10}\right)^{1/4}. \tag{3.6}$$

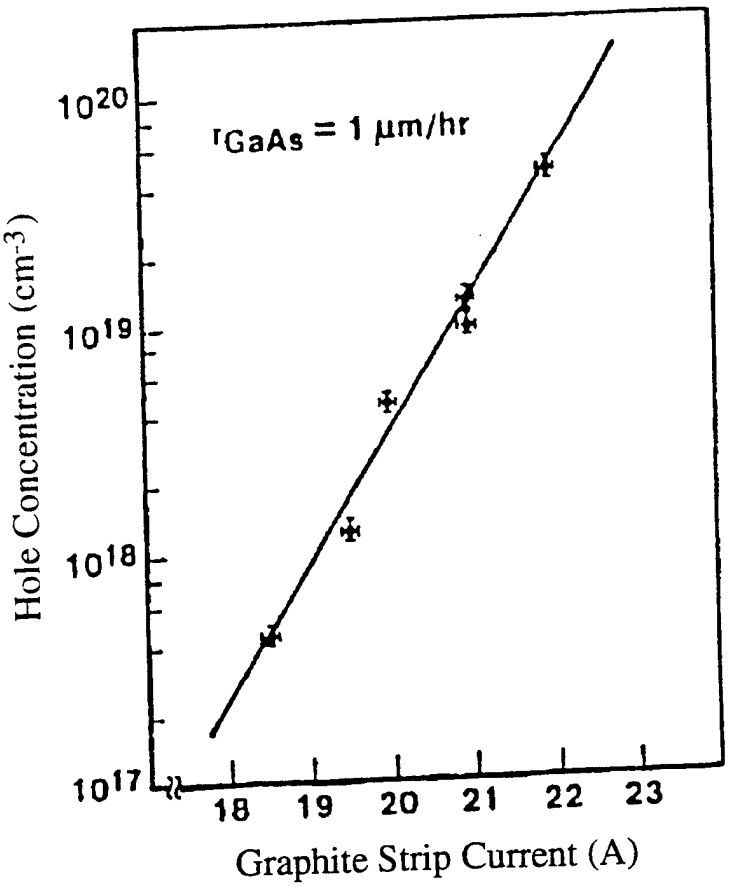

Figure 3.5: Published plot of hole carrier concentration versus graphite filament current (After Malik [18]).

Since the published carbon concentrations occurred in gallium arsenide at an effective growth rate of 1 μm/hr., a relative carbon growth rate could be calculated. Assuming a contribution of one electronic hole per carbon atom:

$$Carbon\ Growth\ Rate\ =\ \frac{(hole\ conc.)(effective\ growth\ rate)}{carbon\ atomic\ density}, \qquad (3.7)$$

where, carbon atomic density = 1.76x10^{23} atoms/cm^3 [7].

Table 3.11 displays the data extracted from Figure 3.5 and an estimation of the carbon growth rates at 2045°, 2150°C, and 2230°C.

Table 3.11: Published carbon concentrations and estimated growth rates at three source temperatures.

I (A)	*Temp. (^{circ}C)*	*C Conc. (cm^{-3})*	*Estimated C growth rate ($\mu m/hr.$)*
19.0	1772	10^{18}	5.68x10^{-6}
21.0	1877	10^{19}	5.68x10^{-5}
22.6	1957	10^{20}	5.68x10^{-4}

Assuming a linear relation between filament surface area and growth rate, the growth rate of any other filament of similar graphite material, growth mechanism, and source to substrate distance can be estimated by scaling to the calculated growth rates in Table 3.11 by the ratio of filament areas. Since these conditions are not easily met, the scaled filament growth rates given are only approximate. Estimated growth rates of the "S" shaped, serpentine, and WWR filament designs, were calculated from the three growth rate points of Malik's filament. The estimated growth rates of all three filaments are listed in Table 3.12.

Extrapolation of growth rate trends were obtained from the three estimated growth rate points in order to predict the growth rates at large source temperatures.

Table 3.12: Estimated carbon growth rate, μm/hr, based on extrapolation from published data [18].

Temperature (K)	*Malik*	*S Shaped*	*Serpentine*	*WWR*
1772	$5.68\text{x}10^{-6}$	$2.75\text{x}10^{-6}$	$5.13\text{x}10^{-6}$	$2.15\text{x}10^{-5}$
1877	$5.68\text{x}10^{-5}$	$2.75\text{x}10^{-5}$	$5.13\text{x}10^{-5}$	$2.15\text{x}10^{-4}$
1957	$5.68\text{x}10^{-4}$	$2.75\text{x}10^{-4}$	$5.13\text{x}10^{-4}$	$2.15\text{x}10^{-3}$

As can be seen from Figure 3.6, the WWR filament design should theoretically provide a greater carbon growth rate than its two predecessors, the "S" shaped and serpentine filaments. This is due to the fact that the growth rate of carbon depends not only on the source temperature, but also the carbon source surface area facing the substrate. By maximizing the surface area of the active region of the carbon filament, a maximum growth rate can be achieved; therefore, filament designs with large active region surface areas, such as the WWR filament, are preferred. Experimental growth with the large area WWR filament, however, has not yet been performed to verify these theoretical predictions.

3.2.3.3 Experimental Growth Rate

As mentioned previously, the estimated carbon growth rates were used only for determination of the initial growth conditions. All subsequent growths and compositional analysis required knowledge of that actual experimental carbon growth rates. All of the carbon alloys grown prior to June 1994 were made using either the "S" shaped or serpentine filament designs. Initial growths were performed using the "S" shaped filament which had short filament lifetimes, 8 hours maximum, and led to abandonment of this filament for growth. The majority of the growths were performed with the serpentine filament. The growth rate of carbon from the serpentine filament was measured using compositional analysis and thickness measurements. From a germanium-carbon sample of known carbon composition and

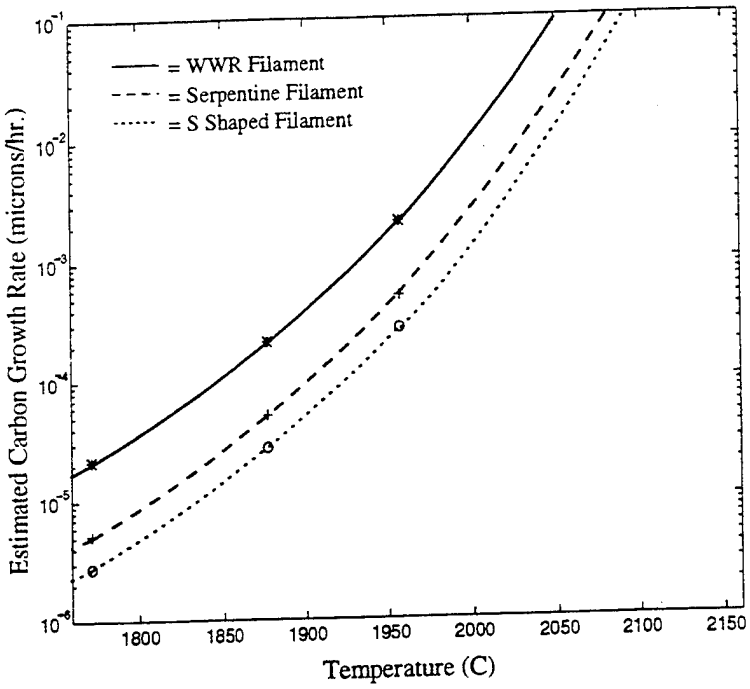

Figure 3.6: Plot of estimated carbon growth rates for "S" shaped, serpentine, and WWR filaments. The Data points shown are the calculated growth rates of Table 3.12.

alloy layer thickness, the carbon growth rate could be determined by the following equations:

$$X_C = \left[\frac{d_C/a_C}{d_C/a_C + d_{Ge}/a_{Ge}}\right], \tag{3.8}$$

and

$$d_C = d\left[\frac{(a_C\ X_C)}{(a_C\ X_C) + (a_{Ge}\ X_{Ge})}\right], \tag{3.9}$$

and

$$G_C = (d_C)(t), \tag{3.10}$$

where,

X_C = Carbon atomic fraction

X_{Ge} = Germanium atomic fraction

a_C = Carbon lattice constant

a_{Ge} = Germanium lattice constant

d_C = Partial layer thickness of C in GeC

d_{Ge} = Partial layer thickness of Ge in GeC

d = Total layer thickness

$d = d_{Ge} + d_C$

t = Duration of total growth

G_C = Carbon growth rate.

Note: Using Equations (3.8) through (3.10) implies that carbon is elastically incorporated into a germanium lattice and effectively displaces the germanium atoms by an amount determined by the carbon lattice constant and concentration.

Using RBS, the percent composition of two germanium-carbon alloys was determined. Further details regarding this technique of compositional analysis will

be discussed elsewhere. The carbon growth rates were calculated using equations 3.9 and 3.10. Table 3.13 summarizes the important sample parameters and the final carbon growth rates for germanium-carbon alloys SGC-11 and SGC-31.

Table 3.13: Experimental determination of carbon growth rate.

Carbon Growth		
Sample Number	SGC-11	SGC-31
Substrate Temperature	500°C	600°C
C Source Current	40 A	38 A
Equivalent C Temperature	2091°C	2031°C
Duration	2.5 hours	3 hours
Measured Thickness (d)	0.153 μm	0.139 μm
Carbon Composition*	28.5%	14.2%
Carbon Thickness (d_C)	0.031 μm	0.013 μm
Carbon Growth Rate	1.24×10^{-2} μm/hr.	4.33×10^{-3} μm/hr.

As shown in Figure 3.7, SGC-11 and SGC-31 both exhibited lower measured carbon growth rates from the serpentine filament than was theoretically estimated. As seen in Figures 3.7 and 3.8, the experimental growth rate trend matches that of carbon vapor pressure rather than Malik's data. This difference may have resulted from differing filament materials and/or source to substrate distances. Other experimental data points were not available since the remaining germanium-carbon growths had very small carbon compositions (less than 5%) and could not be accurately measured by RBS.

Due to non-linearities in growth with the germanium and silicon cells, calculations using the carbon growth rates and carbon incorporation rates were the most reliable methods for determining the composition of alloy layers with low carbon content. Further description of the growth rate and incorporation rate methods used to calculate alloy composition will be discussed in Chapter 5.

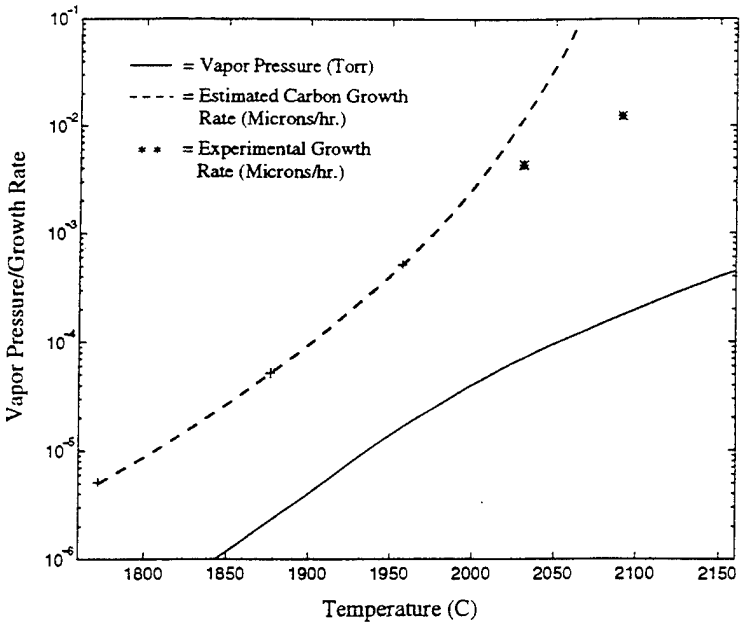

Figure 3.7: Plot of estimated and experimental carbon growth rates of serpentine filament.

3.3 Carbon Cracking Pattern

The molecular weight of the carbon molecular flux during growth can greatly effect the arrangement of carbon atoms within an alloy layer. If carbon molecules, C_2, C_3, C_4, etc., are emitted from the filament and impinge on the substrate, there could exist a higher tendency for carbon clustering than if the carbon beam was purely monatomic. Several published works dating back to as early as 1953, have suggested that C_3 is the dominant molecular species during carbon evaporation [23], [24], [25]. J. Drowart, for example, showed through mass spectrometric studies that during carbon evaporation, the relative ion intensties of C_3 exceeded all other molecular species from C to C_5 [24]. Figure 3.9 illustrates Drowart's findings for carbon emission intensities over a temperature range of 1800K to 2700K (1530°C to 2430°C).

In order to measure the carbon evaporation signature during MBE growth,

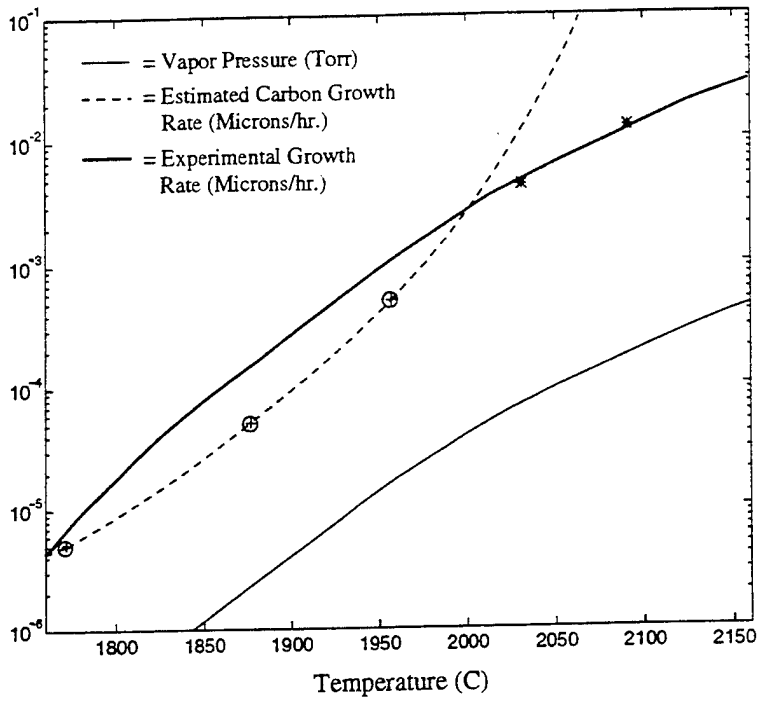

Figure 3.8: Plot of experimental growth rate data for serpentine filament assuming a carbon vapor pressure trend.

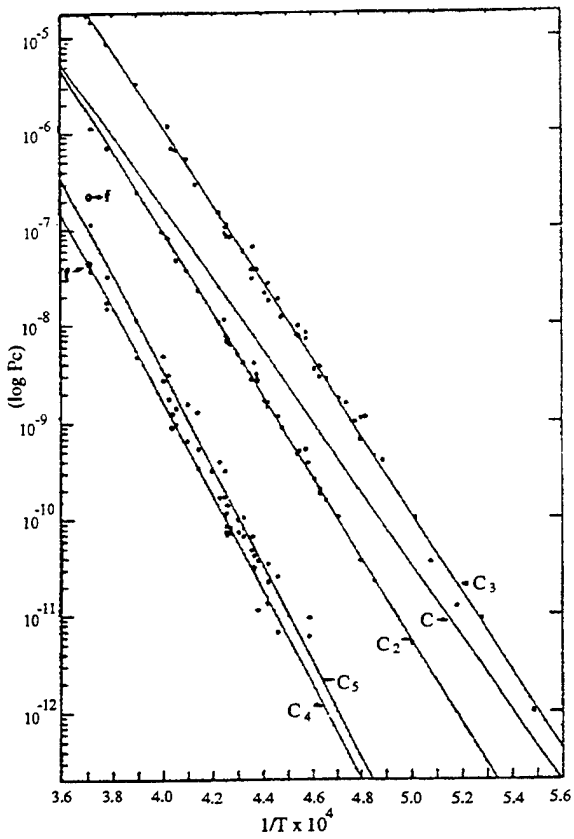

Figure 3.9: Plot of relative ion intensity C_n^+/C^+ (After Drowart [24]).

both the serpentine and WWR filaments were analyzed with the RGA and the carbon cracking pattern was evaluated. The RGA and carbon effusion cell were placed in direct line with one another in the Intro chamber. The gaseous emissions from both the serpentine and WWR filaments were monitored versus filament current. The cracking pattern of many carbon based gases, such as CO and CO_2, were identified by the RGA in addition to the carbon molecular species C_2, C_3, C_4, and C_5. The partial pressures of the significant carbon-based emissions from both filaments were monitored and recorded at a filament temperature of 2090°C. Masses corresponding to C through C_5 were detected; however, these signals were exceeded by impurity gas signals such as carbon monoxide, carbon dioxide, and acetylene. The cracking patterns of these gases produced monatomic carbon, thereby obscuring the amount that is emitted from the filament. The impurity gas partial pressures at mass 12 and 24 were calculated using cracking patterns in stored RGA library files that were scaled by the detected partial pressures for masses 44, 14, 28, and 27. The amount of molecular carbon, or cracking pattern, was estimated by subtracting the cracking patterns of the impurity gases from the observed signals for the carbon molecules. The estimated values, however, may have significant error. The partial pressures of molecular carbon and various carbon based impurity gases for the serpentine and WWR filaments have been presented in Tables 3.14 and 3.15. The "Measured Pressures" listed in the table are the pressures obtained directly from the RGA. The "Partial Pressures" are the individual pressure contributions due to impurities and molecular carbon. Ideally, the sum of the individual partial pressures for any one mass, should equal the measured pressure. For mass 12, this was not the case and an unphysical result was yielded.

Upon comparison of the impurity emissions measured, the serpentine filament appeared to emit over two times the amount of carbon monoxide and ten times the amount of acetylene gas as the WWR filament. Since an unknown portion of the

Table 3.14: RGA results of serpentine filament at 40 amps (2090°C). Total pressure in chamber was approximately 3.2×10^{-8} Torr.

Serpentine Filament			
AMU	Measured Press. (T)	Compound Emitted	Partial Press. (T)
12	3.30×10^{-10}	CO: Carbon monoxide	5.57×10^{-10}
		CO_2: Carbon dioxide	5.70×10^{-11}
		C_2H_2: Acetylene	2.65×10^{-11}
		TOTAL	6.40×10^{-10}
24	9.40×10^{-11}	C_2H_2: Acetylene	5.30×10^{-11}
		C_2: Carbon	**4.10×10^{-11}**
36	1.00×10^{-10}	**C_3: Carbon**	**1.00×10^{-10}**
48	1.50×10^{-11}	**C_4: Carbon**	**1.50×10^{-11}**
60	2.00×10^{-12}	**C_5: Carbon**	**2.00×10^{-12}**

Table 3.15: RGA pressures of WWR filament at 49 amps (2090°C). Total pressure in chamber was approximately 2.5×10^{-8}.

WWR Filament			
AMU	Measured Press. (Torr)	Compound Emitted	Partial Press. (Torr)
12	1.70×10^{-10}	CO: Carbon monoxide	2.07×10^{-10}
		CO_2: Carbon dioxide	1.08×10^{-10}
		C_2H_2: Acetylene	2.00×10^{-12}
		TOTAL	3.17×10^{-10}
24	1.50×10^{-11}	C_2H_2: Acetylene	4.00×10^{-12}
		C_2: Carbon	**1.10×10^{-11}**
36	3.40×10^{-10}	**C_3: Carbon**	**3.40×10^{-11}**
48	1.60×10^{-11}	**C_4: Carbon**	**1.60×10^{-11}**
60	6.00×10^{-12}	**C_5: Carbon**	**6.00×10^{-12}**

observed impurities gases could have evolved from outgassing of the cryopump at high carbon filament temperature, the exact origin of the gaseous emissions remains unknown. Assuming, however, that equal amounts of impurities were emitted from the pump during both filament experiments, the qualitative impurity comparisons would remain valid.

The relative amount of monatomic carbon in both filaments could not be determined since the calculated partial pressures of impurity gases contributing to mass 12 exceeded the detected pressure in the intro chamber. After careful analyzation of the RGA spectra, however, the relative pressures of C_2, C_3, C_4, and C_5 were estimated and plotted as shown in Figures 3.10 and 3.11. As predicted, both filaments produced trimeric carbon, C_3, in excess of all other molecular carbon species. The unexpected decrease in trimeric carbon emission from the WWR filament in comparison to the serpentine filament may result from differences in cracking pattern for each filament and/or a lower operation temperature for the WWR filament than was theoretically predicted.

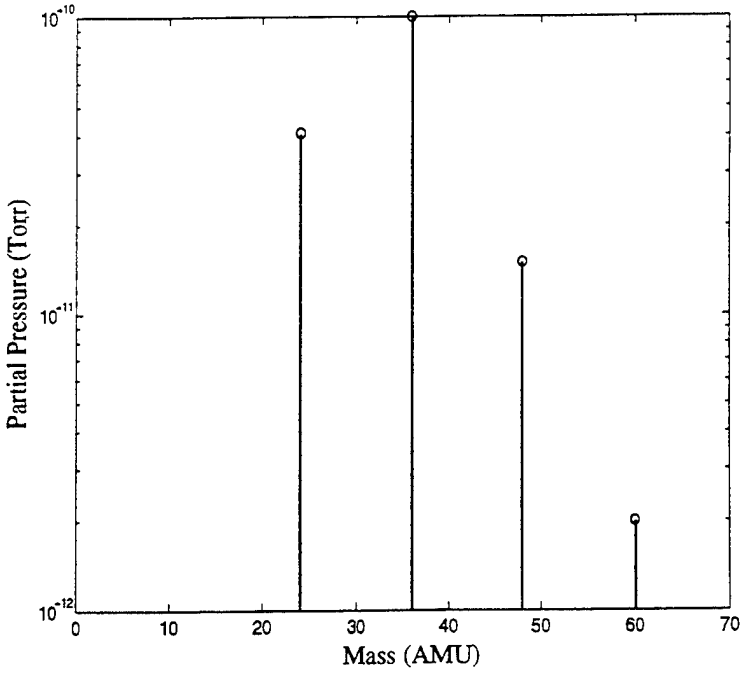

Figure 3.10: Partial pressures of carbon molecular species for serpentine filament.

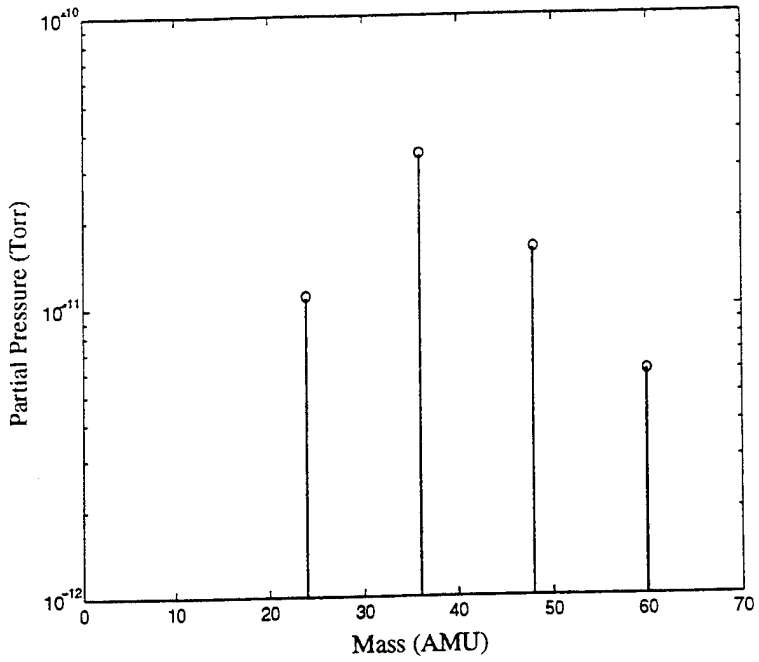

Figure 3.11: Partial pressures of carbon molecular species for WWR filament.

Chapter 4

GROWTH CHARACTERIZATION

Optimization of the substrate growth temperature was performed by analysis of the surface morphology and material structure of the epitaxial layer for varying growth conditions. X-ray diffraction was used to determine whether the growth was single crystal, polycrystalline, or amorphous and Optical Microscopy was used to analyze the growth morphology. The x-ray diffraction measurements were performed by Suibin Zhang using the powder diffractometer in the Materials Science Program.

4.1 X-Ray Diffraction Analysis

By examination of the (400) x-ray diffraction peaks of an epitaxial layer and silicon substrate, an idea of the layer's crystalline nature and amount of carbon incorporation was determined. In order to qualitatively analyze the Ge, GeC, and SiGeC films, estimations of the epitaxial layer's diffraction peak intensity, Full-Width-Half-Maximum (FWHM), and angle between substrate and film diffraction peaks were found. These parameters were examined over various substrate temperatures and carbon concentrations. Although preferred substrate growth temperatures were observed for germanium and germanium-carbon epitaxial layers, single crystal growth has not yet been achieved.

4.1.1 Analysis of Germanium

Suibin Zhang performed X-ray diffraction on all samples grown with the MBE. The x-ray diffraction patterns of six germanium samples that were grown

at differing substrate temperatures were analyzed for variations in the diffraction peaks. The (400) germanium peak intensity, germanium and silicon peak positions, and the germanium FWHM have been determined for each sample as shown in Table 4.1.

Table 4.1: Effect of substrate temperature on germanium x-ray data.

Germanium Films				
Sample Number	Substrate Temp. (C)	Ge (400) Intensity	Ge (400) FWHM	Peak Angle Displacement Si (400) - Ge (400)
SGC-25	300	10%	0.38°	3.10°
SGC-16	400	200%	0.41°	2.66°*
SGC-10	500	40%	0.19°	3.12°
SGC-26	600	60%	0.20°	3.08°
SGC-15	700	40%	0.37°	2.94°
SGC-14	800	10%	0.37°	2.94°

For pure germanium, the sample having the greatest (400) peak intensity with respect to the silicon substrate occurred at a substrate temperature of 400°C (SGC-16). Unfortunately, the accuracy of the x-ray data for this sample is debatable since an unresolved substrate peak at an ambiguous silicon peak position was produced. The sample having the second largest (400) peak intensity occurred at 600°C (SGC-26). Despite the abnormal x-ray diffraction pattern for SGC-16, it was concluded that germanium would most likely crystallize for substrate temperatures between 400° and 600°C. Based on this conclusion, the analyzed sample representing a substrate temperature of 500°C, SGC-10, should have produced a higher intensity germanium peak than was found. Since SGC-10 was grown five months prior to the other samples, additional environmental factors present at that time, such as chamber pressure, may have altered the growth conditions, and thereby produced a weaker intensity than expected. The diffraction results for samples SGC-26 grown at 600°C and SGC-14 grown at 800°C can be seen in Figures 4.1 and 4.2. The

patterns for these samples have been presented since they demonstrate the normal x-ray diffraction peak resolution obtained from the powder diffractometer in the Material Science Program.

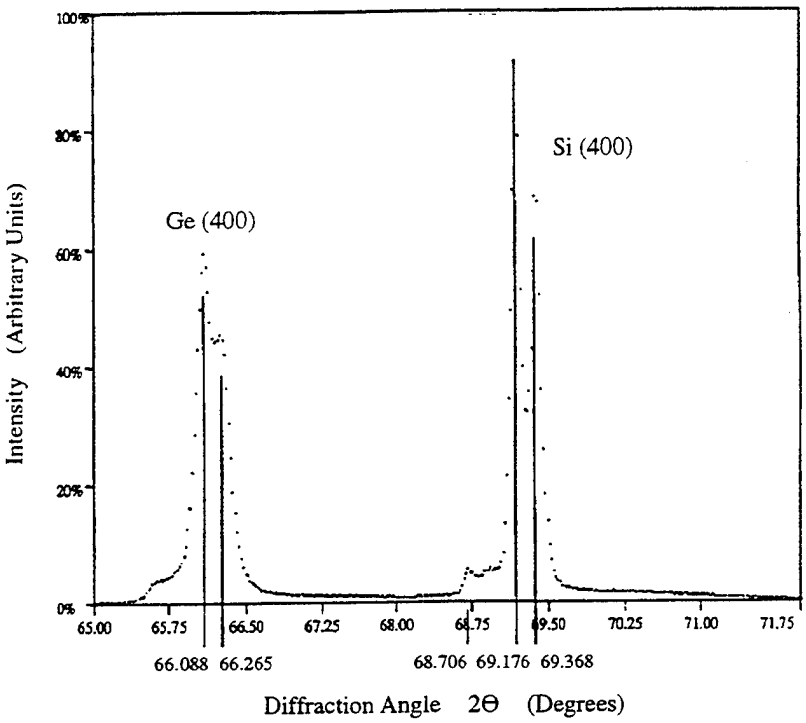

Figure 4.1: Measured x-ray diffraction intensity versus diffraction angle for sample SGC-26 indicating substrate peak at $2\theta = 69.176°$ and epilayer peak at $2\theta = 66.088°$.

The width of an epilayer's (400) peak is usually determined by two factors: the size of the crystallites and the thickness of the grown epitaxial layer. A thick single epitaxial layer would theoretically produce a narrow diffraction peak due to an increased number of planes contributing to constructive interference. In the same respect, a thin epilayer would produce a wide diffraction peak. For polycrystalline growth, the width of the peak would increase since the peak width would now be related to the average crystallite size. Assuming single-crystal growth of all germanium epitaxial layers, Suibin Zhang calculated layer thicknesses based on the

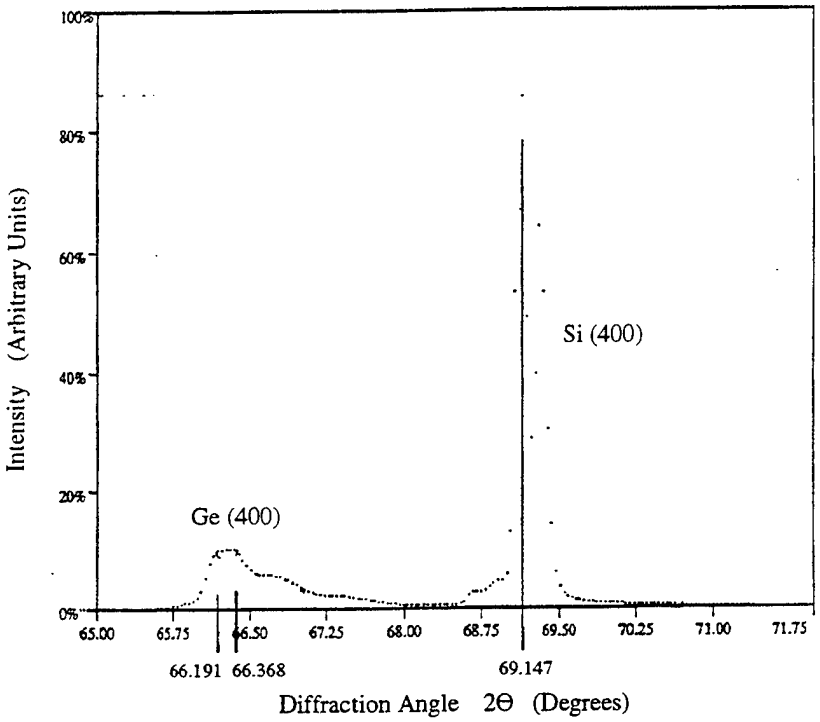

Figure 4.2: Measured x-ray diffraction intensity versus diffraction angle for sample SGC-14 indicating substrate peak at $2\theta = 69.147°$ and epilayer peak at $2\theta = 66.191°$. Due to the high substrate growth temperature, the pattern for SGC-14 demonstrates a decreased epilayer peak intensity and increased FWHM from that of SGC-26.

FWHM of the germanium (400) diffraction peak for each sample. The thicknesses required to produce the peak widths in the diffraction patterns were equal to the crystallite size and less than the actual measured sample thicknesses. Figures 4.1 and 4.2 exemplify the diffraction differences of a single-crystal substrate and polycrystalline epitaxial layer. The difference between Bragg diffraction angles found for the germanium and silicon (400) peaks varied from 2.94° to 3.12°, depending on the (germanium) sample. Since all of the layers were grown well above the critical thickness for dislocation formation, about 4 monolayers [26], strain from the heterojunction could not have accounted for the large variation in peak angles. The error in angle is such that a peak shift in 2θ of at least 0.2° must occur for the shift to be conclusive.

4.1.2 Analysis of Germanium-Carbon

Based on the x-ray diffraction analysis previously noted, pure germanium was most successfully grown on silicon at temperatures between 400° and 600°C. Upon the addition of carbon, however, it is expected that the optimum substrate temperature will vary and become dependent upon the concentration of carbon present. In order to determine the influence of substrate temperature on a germanium-carbon layer, the diffraction patterns for a fixed carbon concentration in germanium was examined at three different substrate temperatures. Data extracted from the diffraction patterns of the three samples was tabulated as seen in Table 4.2. All three samples were grown with a carbon current of 37 Amps and a germanium current of approximately 8.22 Amps.

The x-ray peak intensity was maximized at a substrate temperature of 600°C with the second largest peak occurring at 400°C. The range of temperatures needed for optimum growth of germanium-carbon at this carbon concentration is similar to those found with pure germanium. Since the carbon concentration in silicon-germanium-carbon and germanium-carbon required for silicon lattice matching is

Table 4.2: Effect of substrate temperature on germanium-carbon x-ray data.

Germanium-Carbon				
Sample Number	Substrate Temp. (C)	Ge (400) Intensity	Ge (400) FWHM	Displacement Si (400) - Ge (400)
SGC-26	400	50%	0.25°	3.14°
SGC-15	600	63%	0.20°	3.08°
SGC-14	700	25%	0.18°	3.10°

relatively small (about one tenth the concentration of germanium), only slight increases in substrate temperature from that for germanium may be required for growth of these alloy films at the required carbon concentrations.

Assuming that carbon atoms bond within a germanium lattice substitutionally, the addition of carbon to germanium should theoretically produce a shift in the (400) diffraction peak to greater diffraction angles. This shift would lessen the displacement between the epitaxial layer and substrate diffractions peaks by an amount proportional to the composition of the alloy. For the germanium-carbon samples shown in Table 4.2, no observable shift greater than 0.2° (the margin of error for pure germanium), occurred. The carbon, therefore, had no conclusive effect on the lattice constant of the epitaxial layer and a lattice constant equivalent to that of germanium was observed.

Two situations have been provided that may explain the germanium lattice parameter found for germanium-carbon. Assuming that each interstitial site within a germanium lattice is as large as the carbon atom, the carbon atoms may have occupied these interstitial sites, rather than substitutional sites, and caused no lattice deformation. Another possibility is that the carbon atoms may have incorporated into the germanium lattice in such a manner that the carbon sites were the size of germanium vacancies. This latter situation could only remain valid in the case of small carbon concentrations since excess strain energy between the germanium

and carbon bonds would be present with large carbon concentrations. Furthermore, after calculating the effective lattice constant of carbon in germanium, a tendency toward an "elastic model" lattice structure has been determined. The term "elastic model" has been used to represent an alloy sructure in which all atoms have bonded into the lattice at values close to their lattice parameters. Calculation of the effective carbon lattice constant of germanium-carbon sample SGC-11 as determined by Equation (4.1) has suggested that carbon within the lattice displaces 0.455 times that of germanium. The effective lattice constant of carbon in SGC-11 would be approximately 2.5742 Å. This value is lower than the actual lattice constant of carbon, 3.5597 Å, since a significant amount of oxygen, an element with a smaller atomic radius than carbon, was present within the sample.

$$a_c = a_{Ge} \left(\frac{d_C}{d_{Ge}}\right) \left(\frac{X_{Ge}}{X_C}\right) \tag{4.1}$$

To determine if changes in the lattice occur over variations in carbon concentration, several germanium-carbon layers were grown at a substrate temperature of 600°C and at varying carbon and germanium currents. The diffraction pattern features were recorded as shown in Table 4.3

Table 4.3: Effect of carbon concentration on germanium-carbon x-ray data. Substrate temperature = 600°C, germanium current = 8.22 Amps except for SGC-31 for which germanium current = 7.8 Amps.

Germanium-Carbon				
Sample Number	Carbon Current (A)	GeC (400) Intensity	GeC (400) FWHM	Displacement Si (400) - GeC (400)
SGC-27	35	65%	0.17°	3.14°
SGC-24	36	58%	0.16°	3.08°
SGC-23	37	63%	0.20°	3.08°
SGC-30	38	60%	0.16°	3.06°
SGC-31	38	10%	0.29°	3.06°

Four of the five germanium-carbon sample (400) intensity peaks displayed similar intensity and all of the peaks exhibited similar peak widths. The sample with the largest concentration of carbon, SGC-31, did show a significant difference in the intensity of the epilayer peak. The low diffraction intensity obtained would tend to indicate that an excess of carbon may possibly degrade the film quality. Further growth studies, however, are required to validate this hypothesis. The diffraction patterns of germanium-carbon samples SGC-27 and SGC-31 are shown in Figures 4.3 and 4.4.

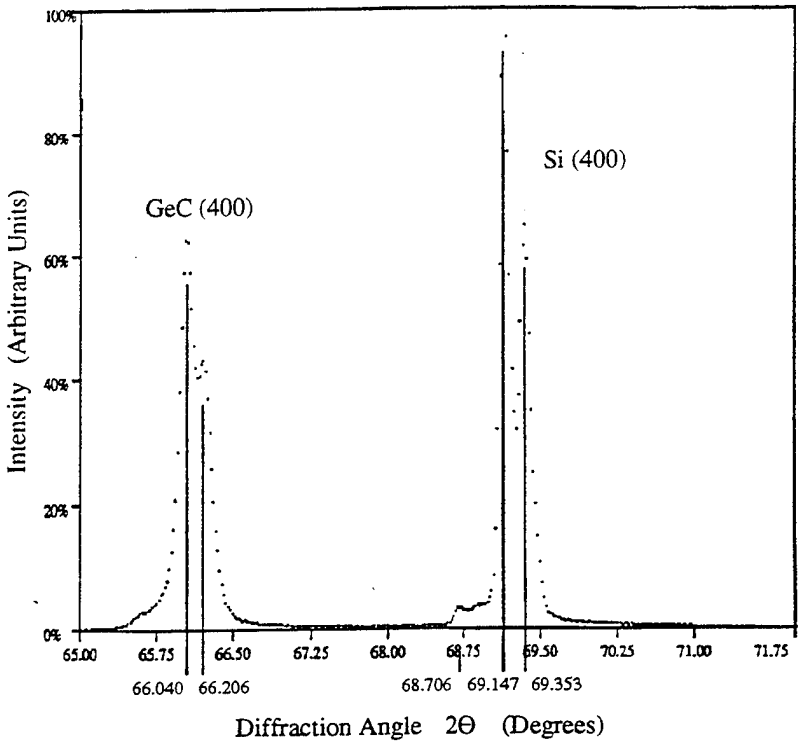

Figure 4.3: Measured x-ray diffraction intensity versus diffraction angle for sample SGC-27 indicating substrate peak at $2\theta = 69.147°$ and epilayer peak at $2\theta = 66.040°$.

In addition to estimates of the epilayer film quality, the x-ray data can yield the lattice constant of the layer using Bragg's Law. To determine if any change in lattice constant occurred upon the addition of carbon to germanium, the epilayer's

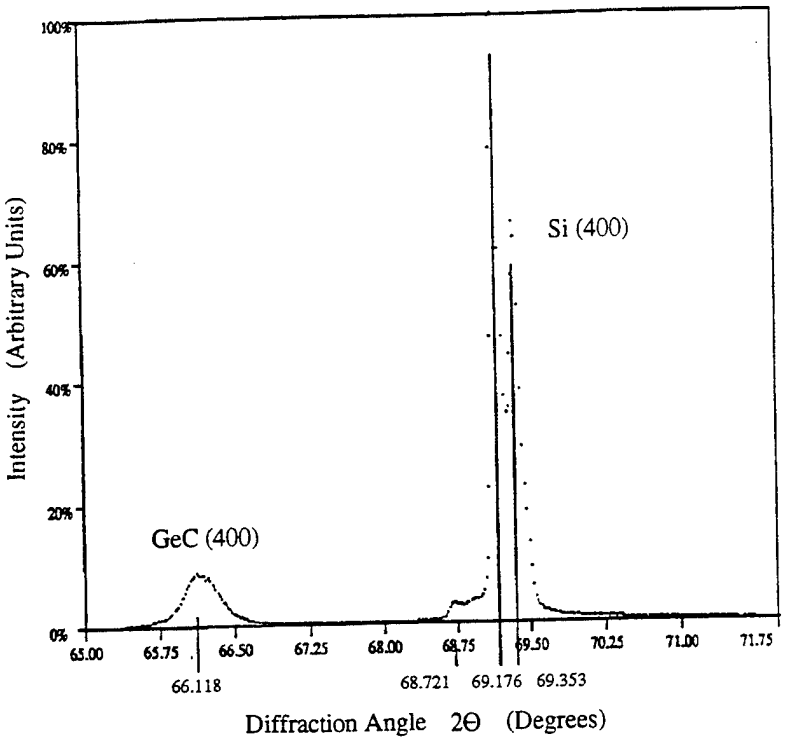

Figure 4.4: Measured x-ray diffraction intensity versus diffraction angle for sample SGC-31 indicating substrate peak at $2\theta = 69.176°$ and epilayer peak at $2\theta = 66.118°$. The pattern for SGC-31 demonstrates a decreased epilayer peak intensity from that of SGC-27. This decrease may be a result of the high concentration of carbon within the epilayer.

peak location in reference to the silicon substrate has been examined and compared to that of pure germanium. The displacement in 2θ between the substrate and epilayer peaks diminished with increasing carbon concentration; however, the shift did not exceed the system error of 0.2°. Therefore, no conclusions regarding the amount of carbon incorporation could be drawn from the x-ray data.

4.1.3 Analysis of Silicon-Germanium-Carbon

Unlike the germanium and germanium-carbon epitaxial layers, the diffraction patterns for the two silicon-germanium-carbon layers exhibited multiple diffraction peaks. The appearance of multiple peaks in a diffraction pattern of an alloy implies one of two conditions: either the sample is polycrystalline or the elements of the alloy have segregated to form individual layers. For the case of silicon-germanium-carbon, the multiple peaks were caused by varying surface indices within the sample so that the x-ray measurements did not produce constructive interference at a single Bragg diffraction angle. As with the germanium and germanium-carbon films, the ternary alloy samples were polycrystalline.For the ternary alloy, however, the crystallites were not oriented in the same direction and thereby produced multiple diffraction peaks. As determined by Suibin Zhang, the peaks were located at slightly higher diffraction angles than for germanium (400), (200), (111), and (311) surfaces [27]; therefore, the polycrystals were either silicon-germanium, germanium-carbon, or silicon-germanium-carbon. Broad and narrow range scans of the x-ray diffraction pattern for SGC-19 are shown in Figures 4.5 and 4.6 respectively.

4.2 Growth Morphology

In order to determine the dependence of the quality of epitaxial growth on substrate temperature, the surface morphology of the grown layers was examined using a Leica Optical Microscope with interference contrast (Nomarski) objectives.

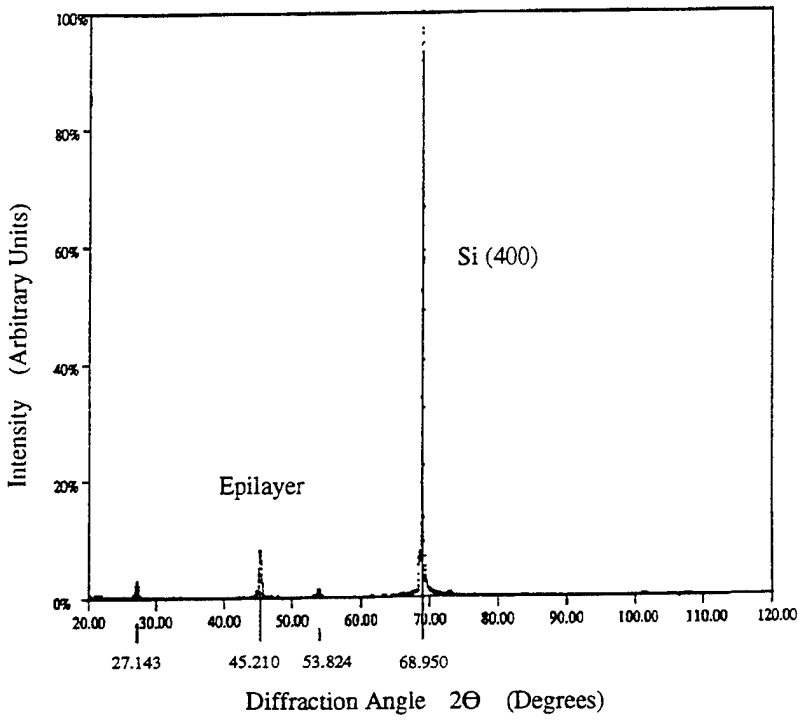

Figure 4.5: Broad range scan of x-ray diffraction results for SGC-19. Pattern includes diffraction peaks generated from both the substrate and epilayer.

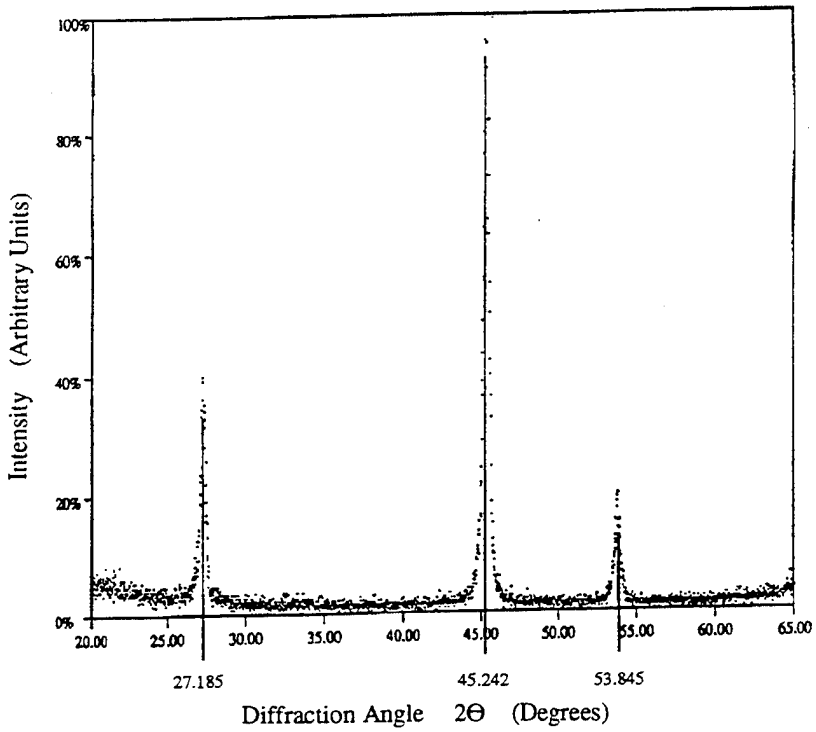

Figure 4.6: Narrow range scan of x-ray diffraction results for SGC-19. Pattern excludes diffraction peaks generated by substrate.

For optimum near-single-crystal growth, a smooth, mirror-like surface should be observed up to a magnification of 1000x.

4.2.1 Germanium Surface Morphology

Six germanium samples were grown on substrates ranging in temperatures from 300°C to 800°C. Qualitative descriptions of each sample's morphology are shown in Table 4.4. For high substrate temperatures, 700°C and above, variations in surface morphology were visually observed as haziness or cloudiness without magnification of the sample surface.

Table 4.4: Effect of substrate temperature on germanium surface morphology.

Germanium		
Sample Number	Substrate Temp. (C)	Surface Morphology (1000x) / (No Magnification)
SGC-25	300	(No texture, smooth) / (Mirror finish)
SGC-16	400	(No texture, smooth) / (Mirror finish)
SGC-10	500	(No texture, smooth) / (Mirror finish)
SGC-26	600	(Slight texture, dimpled) / (Mirror finish)
SGC-15	700	(Extreme texture, Rough) / (Hazy finish)
SGC-14	800	(Extreme texture, Rough) / (Hazy finish)

The surface morphology of SGC-14 at 1000x magnification is shown in Figure 4.7 in order to demonstrate the effect of high substrate temperatures during the growth of germanium.

4.2.2 Germanium-Carbon Surface Morphology

Germanium-carbon alloy samples were grown at substrate temperatures ranging from 400°C to 700°C. Growth was not performed at 300°C and 800°C due to the poor surface morphology and low x-ray diffraction intensities found with pure germanium. As with the germanium samples, growths at 400°C and 500°C demonstrated

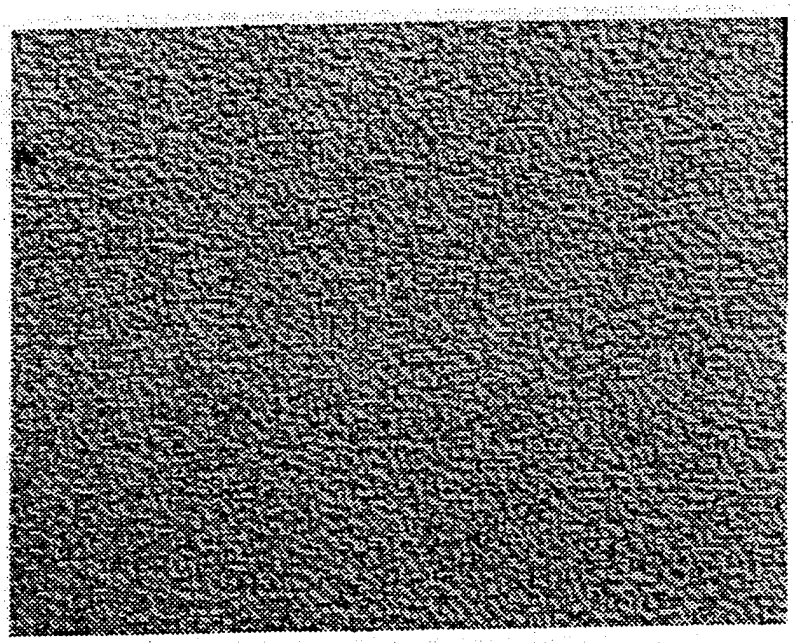

Figure 4.7: Surface morphology of germanium sample SGC-14, as photographed at 1000x magnification, indicating rough hazy surface. Scale: 1 cm is equivalent to 10 μm.

specular finishes upon normal visual inspection and at magnifications up to 1000x. Samples grown at 600°C exhibited texturing that was only visible upon magnification. The surface morphology of SGC-31, grown at 600°C, was photographed as seen in Figure 4.8 using the Leica microscope at a magnification of 1000x. Differential interference contrast was used in order to provide three-dimensional enhancement.

Table 4.5: Effect of substrate temperature on germanium-carbon surface morphology.

Germanium-Carbon		
Sample Number	Substrate Temp. (C)	Surface Morphology (1000x) / (No Magnification)
SGC-17,18,21	400	(No texture, smooth) / (Mirror finish)
SGC-11,32	500	(No texture, smooth) / (Mirror finish)
SGC-23,24,27,30,31	600	(slight texture, dimpled) / (Mirror finish)
SGC-28,29	700	(Extreme texture, Rough) / (Hazy finish)

4.2.3 Silicon-Germanium-Carbon Surface Morphology

Two silicon-germanium-carbon samples, SGC-19 and SGC-20, were grown at a substrate temperature of 400°C. Upon visual inspection of the two samples at magnifications up to 1000x, a smooth, specular, mirror-like surface was observed.

Table 4.6: Silicon-germanium-carbon surface morphology.

Germanium-Carbon		
Sample Number	Substrate Temp. (C)	Surface Morphology (1000x) / (No Magnification)
SGC-19	400	(No texture, smooth) / (Mirror finish)
SGC-20	400	(No texture, smooth) / (Mirror finish)

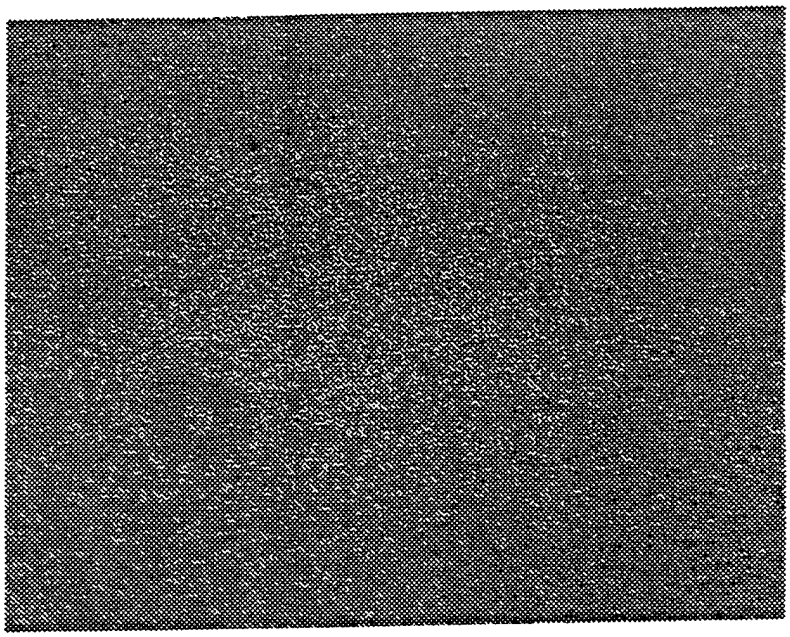

Figure 4.8: Surface morphology of germanium-carbon sample SGC-31, as photographed at 1000x magnification, indicating slight texturing. Scale: 1 cm is equivalent to 10 μm.

4.3 Annealing Effects

In attempt to increase the size of the crystallites of the grown epitaxial layers and possibly incorporate any interstitial carbon atoms, annealing and further x-ray diffraction measurements were performed by Suibin Zhang. The diffraction patterns of the post-annealed samples were examined for variations in peak intensity and peak width. Furthermore, the patterns obtained for the germanium-carbon layers were examined for evidence of a decrease in lattice constant from that of pure germanium by comparing the displacement of the germanium-carbon peak from the peak of the silicon substrate. Evidence of a decrease in lattice parameter for the germanium-carbon alloys would indicate substitutional carbon incorporation upon annealing. In addition to x-ray diffraction analysis, the annealed samples' surface morphology was examined at a magnification of 1000x on the Leica Optical Microscope and 15,000x on a Scanning Electron Microscope (SEM). Five samples were annealed for one-half

hour at 900°C in forming gas. Four of the five samples were germanium-carbon alloy layers identified as SGC-11, SGC-23, SGC-27, and SGC-31. The fifth sample was SGC-19, a silicon-germanium-carbon alloy layer.

4.3.1 Lattice Parameter

After comparing the pre- and post-annealed diffraction patterns, little variation, other than decreased layer peak intensity and increased layer peak width, was observed in four of the five given samples. Germanium-carbon sample SGC-31, however, exhibited a shift in the (400) epitaxial peak relative to the substrate implying a decrease in the layer's lattice constant. Prior to any annealing, the 2θ displacement between the germanium-carbon layer and the silicon substrate was 3.06°, within the 0.2° range surrounding pure germanium (average germanium displacement was found to be 3.09°). After annealing for one-half hour at 800°C an initial shift was observed in the diffraction peak that lessened the layer to substrate peak displacement to 2.94°. After annealing at one-half hour at 900°C, the displacement between the peaks lessened to 2.21°, a substantial shift that is well outside the instrumental error. The diffraction patterns for the cases previously described are shown in Figures 4.9 and 4.10. Further structural analysis, including lattice parameter approximations, has been reported by Suibin Zhang [27].

4.3.2 Morphology

Following the 900°C anneal of samples SGC-11, SGC-19, SGC-23, SGC-27, and SGC-31, the surface morphology of each sample was examined at 1000x magnification. Each sample demonstrated a change in surface morphology following annealing. The post-annealed morphologies of the five samples all demonstrated random, surface nonunifomities resembling segregation or possible island formation. The morphologies of GeC samples SGC-31 and SGC-27 are shown in Figures 4.11 and 4.12 respectively.

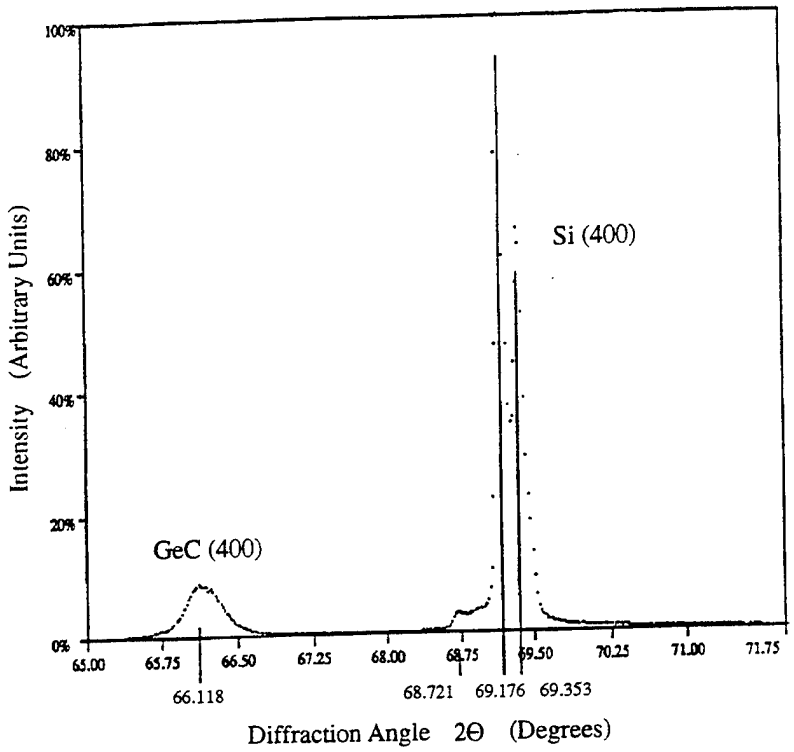

Figure 4.9: X-ray diffraction pattern for SGC-31, as grown.

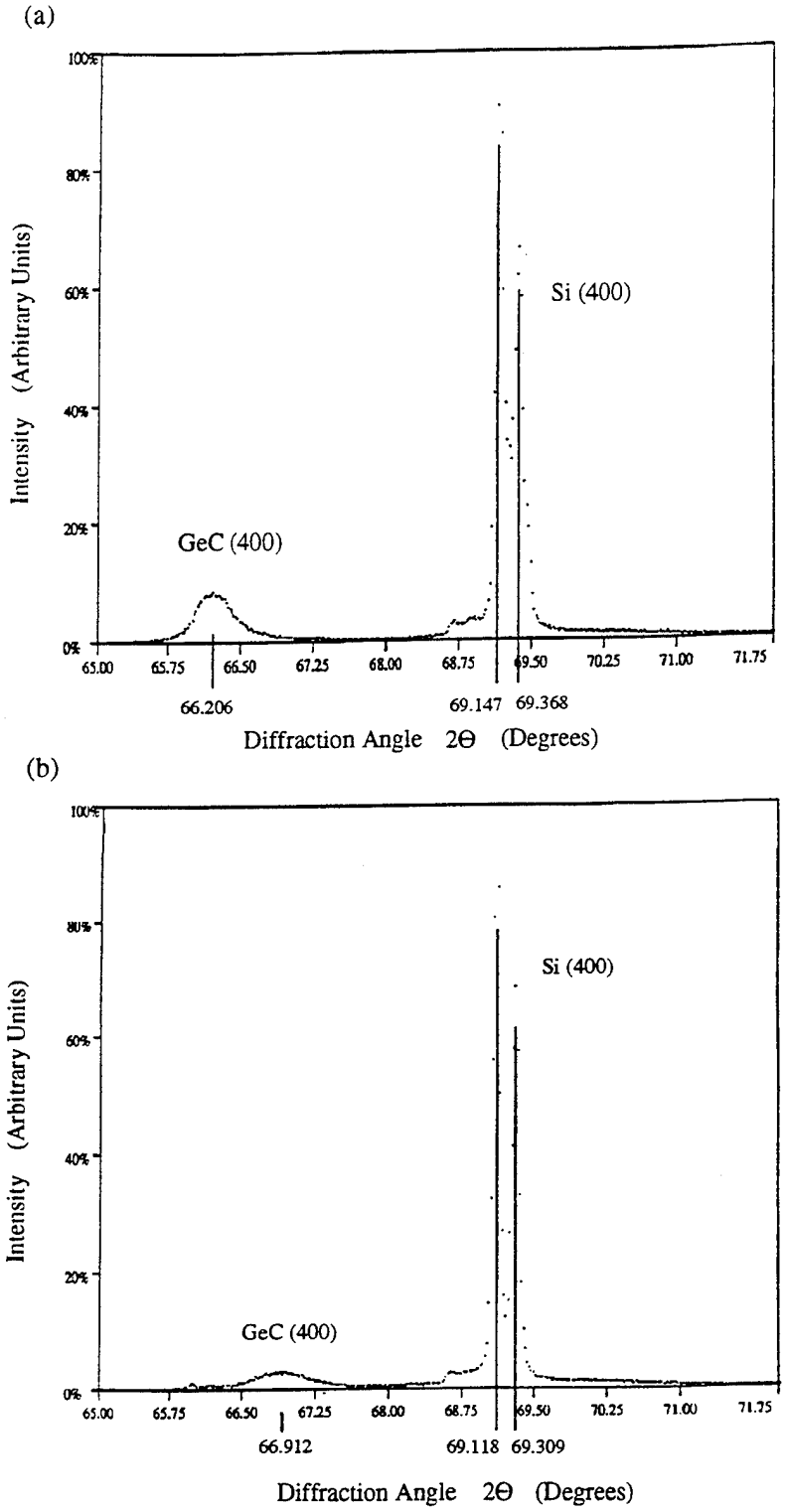

Figure 4.10: X-ray diffraction patterns for germanium-carbon sample SGC-31, (a) after annealing at 800°C for 1/2 hour and (b) after annealing at 900°C. The shift in diffraction angle for the GeC (400) peak implies a decrease in lattice constant after annealing at 900°C.

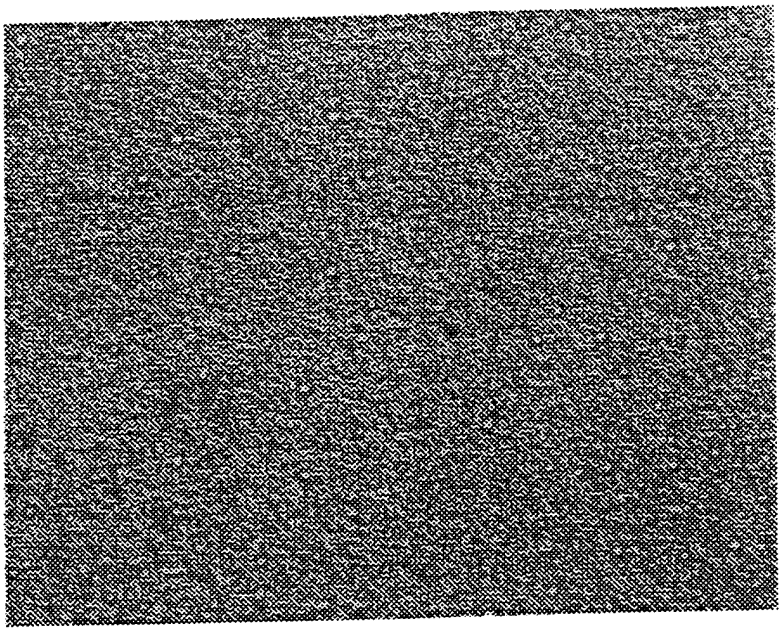

Figure 4.11: Surface morphology of germanium-carbon sample SGC-31 after annealing at 900°C. Magnification = 1000x. Segregates or particles appeared following annealing. 1 cm is equivalent to 1 μm.

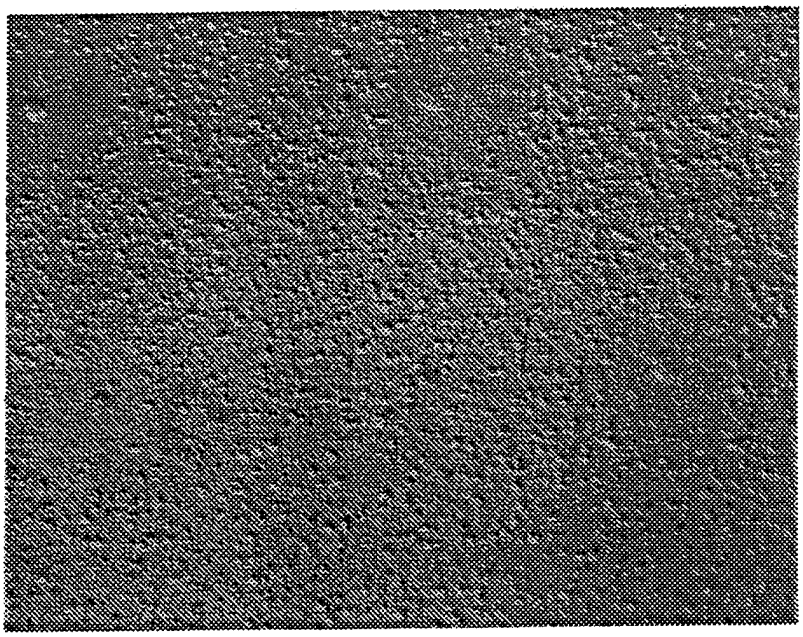

Figure 4.12: Surface morphology of germanium-carbon sample SGC-27 after annealing at 900°C. Magnification = 1000x. Precipitates formed following annealing. 1 cm is equivalent to 1 μm.

The segregation occurred unevenly across the samples. The center portion of each sample exhibited the largest particle sizes in comparison with the other regions. For example, the segregates of Figure 4.11 represent center portion particle sizes of approximately 1 μm in diameter.

Further magnification of samples SGC-31 and SGC-27 was performed using a Scanning Electron Microscope (SEM), courtesy of the Institute for Energy Conversion. For each sample, the surface was examined "as-grown" and following the 900°C annealing. As seen in Figure 4.13, only slight variation between pre- and post-annealed surface morphologies of germanium-carbon layer SGC-31 were apparent at a magnification of 15,000x. Germanium-carbon sample SGC-27, however, exhibited substantial changes in surface morphology. After annealing, the uniformly textured surface developed larger crater-like features within a smooth surrounding material.

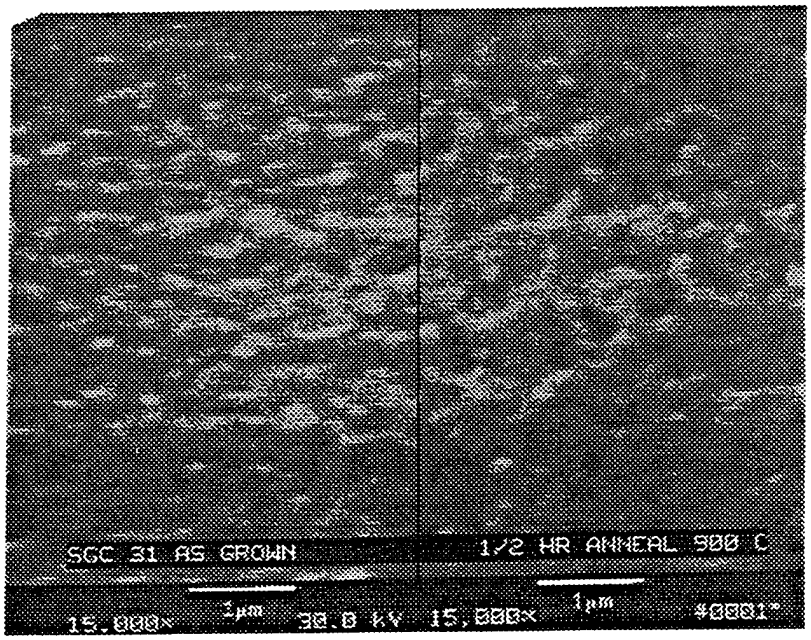

Figure 4.13: Scanning electron micrograph of germanium-carbon sample SGC-31 before and after annealing at 900°C indicating slight variations in surface morphology. Magnification = 15,000x.

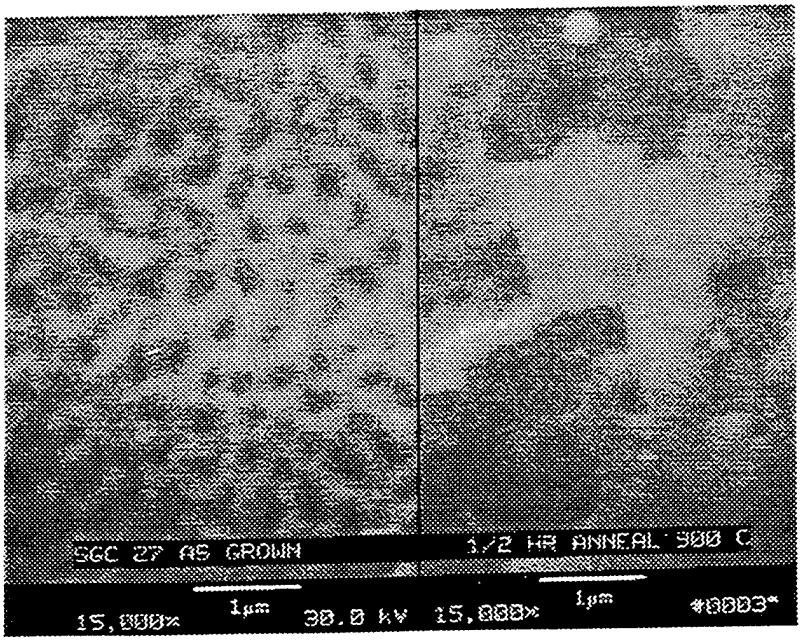

Figure 4.14: Scanning electron micrograph of germanium-carbon sample SGC-27 before and after annealing at 900°C indicating that surface morphology becomes cratered by annealing at 900°C. Magnification = 1000x.

Upon comparison of the annealed surface morphologies of SGC-27 and SGC-31, the variation in pre- and post-annealed morphologies may be dependent upon the carbon concentration within the epilayer. For example, SGC-27 was composed of 99.3% germanium and 7% carbon (to be discussed in Chapter 5). Therefore, annealing close to the melting point of germanium may have caused slight melting of the epilayer. SGC-31, however, contains a large concentration of carbon, 15.2%. The increased concentration of carbon in germanium may have effectively increased the epilayer melting temperature and thereby prevented any partial phase changes from occurring at the annealing temperature of 900°C. Further characterization would be required in order to determine if the observable change in surface morphology had any direct effect on the crystalline structure of the material. Transmission Electron Microscopy (TEM) would provide further information regarding this issue and is presently being performed by Xiaoping Shao at the University of Delaware.

Overall, through x-ray diffraction analysis and surface microscopy, the effects of substrate temperature, carbon concentration, and annealing on surface morphology and/or crystallite size have all been demonstrated for germanium-carbon alloys. Further growth of silicon-germanium-carbon needs to be performed before similar analysis of growth temperature and compositional effects can be performed.

Chapter 5

COMPOSITIONAL CHARACTERIZATION

The most fundamental property of any alloy is its composition. Comparative analysis of electrical and structural characteristics requires the knowledge of the alloy's composition in order to optimize material parameters. Lattice constant and band-gap are two examples of material properties that may depend on the composition. A reliable and relatively accurate means for determining the composition of the grown germanium-carbon and silicon-germanium-carbon layers is therefore required.

5.1 Auger Electron Spectroscopy

A limited number of compositional techniques have the ability to detect carbon concentrations within a material. Auger Electron Spectroscopy (AES) is one of these techniques and is extremely sensitive to carbon and readily detects carbon contamination on the surface of any sample. Due to the ability of AES to detect carbon at low concentrations (1%), this technique was utilized as the initial method for determining alloy composition.

5.1.1 Principles of AES

Auger Electron Spectroscopy involves the measurement of Auger electrons emitted from the surface as a result of an electron beam. As an electron energy beam is projected at the surface of a sample, a large percentage of the incident electrons will backscatter with little energy loss. Another percentage, otherwise known

as secondary electrons, will cause other electrons within the material to decay to lower energy states. The added energy given to a material as a result of this decay may be given to a third set of electrons known as Auger electrons. The energetic auger electrons at the surface can then eject from the sample with a kinetic energy that is characteristic of the parent atom from which it came. The number of Auger electrons emitted from the surface will be proportional to the quantity of parent atoms. The cylindrical mirror analyzer of the AES system collects the electrons of various energies and supporting electronics produce a differentiating energy distribution. Since each element produces a set of auger electrons of a characteristic energy distribution, the constituents of a sample's surface may be determined. The surface concentration of the sample may be determined based on the relative peak to peak magnitudes and utilizing known sensitivity factors.

In order to perform AES, four main features must be present within the system: an electron source, electron detector/analyzer, supporting electronics for signal interpretation, and an ultra high vacuum environment. The system used for Auger analysis, as illustrated by B. Pregger, is shown in Figure 5.1 [28].

The nude ion gauge shown serves two purposes in the chamber. Its main function is to monitor the pressure within the chamber. Its secondary function is to ionize argon gas that is bled into the chamber. By placing a bias of -800 volts on the sample, the ionized argon is attracted to the sample and slowly sputters its surface. Since it is desired to completely remove any contaminants from the sputtered region, the Ion pump (Varian, 140 l/s Diode) must be functioning during sputtering and keep a constant low pressure within the chamber. With the aid of Al Khan, Department of Electrical Engineering Department, University of Delaware, complete guidelines to the usage of the auger system have been prepared. These guidelines are included in Appendix A.

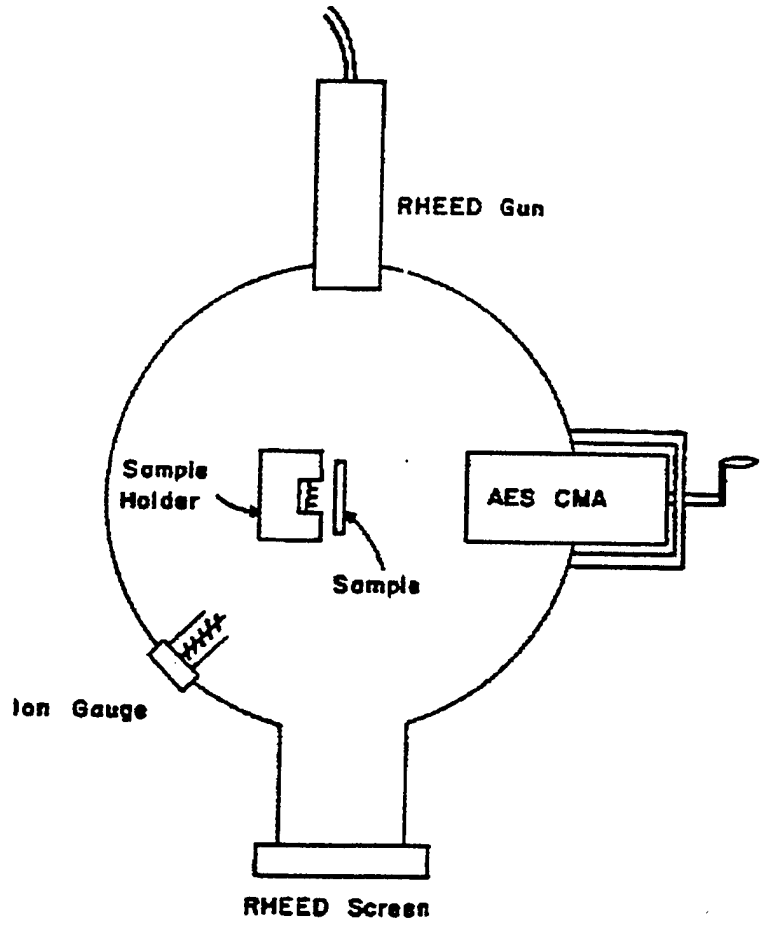

Figure 5.1: Schematic of AES ultra high vacuum system and components (Adapted from B. Pregger [28]).

As a compositional technique, AES offers many advantages. For example, detection of light masses such as carbon is possible; analysis is not limited to samples of large thickness since AES is a surface technique; and given adequate sputtering capability, a depth profiling analysis may be obtained. Without adequate sputtering rates, however, samples with nonuniform concentration profiles can not be accurately analyzed since only a surface composition will be obtained. Furthermore, assuming a uniform alloy composition, sputtering may still be required if surface contaminants, such as carbon, compose a percentage of the bulk material (as in germanium-carbon). Without sputtering, the surface carbon would cause an increased characteristic peak in the Auger energy distribution which may be unintentionally included in the compositional analysis. These issues will be discussed in further detail along with the Auger compositional analysis of germanium and germanium-carbon epitaxial layers.

5.1.2 Compositional Analysis

The composition of a sample from an Auger spectrum can be most accurately determined by comparison of the peak energy intensities with the intensities of known standards. Using a more convenient and reasonably accurate approach, composition has been determined by normalization of a spectrum's peak intensities with published sensitivity factors. The sensitivity factors from the Handbook of Auger Electron Spectroscopy were used to determine sample composition by the following equation:

$$C_x = \frac{\frac{I_x}{S_x}}{\sum_{a=1}^{n} \frac{I_a}{S_a}}, \tag{5.1}$$

where,

C_x = Percent composition of element x

I_a = Peak to Peak Intensity of element a

S_a = Sensitivity factor of element a

n = Total number of elements used in comparison.

and,

S_{Si} = 0.025, Silicon sensitivity factor

S_{Ge} = 0.107, Germanium sensitivity factor

S_C = 0.190, Carbon sensitivity factor

S_O = 0.510, Oxygen sensitivity factor

Equation (5.1) implies that the concentration of a particular element is determined by dividing the normalized spectrum intensity of the particular element in question by the sum of the normalized spectrum intensities of each element.

In order to determine the composition of germanium-carbon layer SGC-11, a 1 cm^2 sample was loaded into the Auger system along with a pure germanium sample, identified as SGC-10. Upon examination of the Auger traces of both samples, excessive amounts of carbon and oxygen were detected in even the pure germanium sample at energies of 273 eV and 510 eV respectively. In order to provide an accurate measurement of carbon in the bulk of the alloy, removal of all surface contaminants through sputtering was required. After 3 hours of argon sputtering with the ion gauge, the spectrum showed a significant amount of carbon still remaining on the surface of the pure germanium sample. Since both samples had been rinsed in methanol just prior to loading, it was assumed that the amount of carbon and oxygen contamination on the surface of the germanium surface was identical to that on the germanium-carbon surface. An estimated composition for germanium-carbon sample SGC-11 was calculated by subtracting the carbon and oxygen intensities obtained from the germanium sample.

After subtracting the carbon and oxygen surface intensities from the spectrum of SGC-11, Equation (5.1) was used to determine the sample composition. Germanium, carbon, and oxygen were detected and the relative compositions are given in Table 5.1.

Table 5.1: Composition of germanium-carbon alloy, SGC-11, as determined by AES.

Element	Composition
Germanium	43%
Carbon	55.6%
Oxygen	1.4%

According to estimated carbon and germanium growth rates, the amount of carbon in sample SGC-11 should not have exceeded the amount of germanium. Either subtraction of the germanium layer surface impurity levels did not account for all of the carbon on the surface of SGC-11, or the sample exhibited carbon segregation toward the surface. To check the accuracy of AES system and the calculation methods, a silicon-germanium sample of known concentration was measured. A $Si_{0.93}Ge_{0.07}$ layer was obtained from Dr. S. Iyer [IBM Corp, T.J. Watson Research Center]. The original composition had been determined by Iyer using x-ray diffraction analysis and assuming Vegard's Law. Any surface carbon or oxygen could be ignored since x-ray diffraction is a bulk measurement technique.

As shown in Table 5.2, the composition determined by AES was within 10% of the value of composition that IBM had determined. This is a reasonable error and concludes that neither the system's margin of error nor the calculation method could have accounted for the large carbon concentration that was found for germanium-carbon sample SGC-11. As will be discussed later, it is believed that the high value of carbon fraction at the surface is a real effect and demonstrates non-uniformities in composition. Due the apparent surface sensitivity of AES and lack of efficient

sputtering capability, alternative methods for determining the composition of carbon alloys was investigated.

Table 5.2: Composition of silicon-germanium alloy (Sample IBM-27), obtained from S. Iyer, as determined by AES at the University of Delaware and X-Ray diffraction at IBM.

Element	AES	X-Ray
Germanium	7.7%	7%
Silicon	92.3%	93%

5.2 Rutherford Backscattering Spectrometry

Another technique capable of detecting carbon within a material is Rutherford Backscattering Spectrometry (RBS). Unlike AES, RBS is a bulk analysis technique and therefore provides an average composition of the sample in question. As seen with AES, segregation and/or contamination can cause invalid overall sample compositions if a bulk technique is not employed. In addition, unlike most bulk techniques, compositional depth profiling has been achieved with RBS by the use of simulation models that are designed to fit to experimental data.

5.2.1 Principles of RBS

In RBS, a sample is bombarded by helium ions of a given energy. The collision of ions with a sample produces an energy transfer that is dependent upon the target material. In other words, atoms of light mass within the sample will absorb more energy from the ions than atoms of heavy mass. Figure 5.2 gives an example for a target of gold (Au) and aluminum (Al) and demonstrates this variation in backscattered ion energy due to target atom size [30]. Due to the principle of conservation of energy, the light mass particles (Al) cause low energy backscatter and the heavy mass particles (Au) cause high energy backscatter. A

detector measures the energy distribution of the backscattered ions from the sample. The energy distribution can be used to determine the target type and concentration. The principle of conservation of energy relates the incident to scattered energies and makes identification of a target possible provided that the incident beam energy and backscattering ion energies are known.

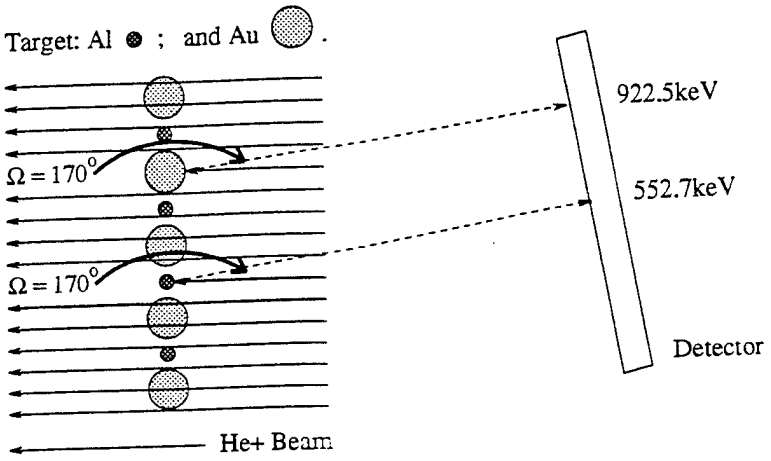

Figure 5.2: Diagram demonstrating varied backscattering energies due to variations in target size (Adapted from W. Chu [30]).

The helium ion beam for RBS system was generated using a 2.5 MeV Van de Graff accelerator. The generated ions were directed towards the target by means of focusing and analyzing magnets. A schematic diagram of the RBS system, as drawn by D. Beames [31], used to obtain compositional data of germanium-carbon and silicon-germanium-carbon alloys is shown in Figure 5.3. All of the RBS spectra were collected in collaboration with Dr. Charles Swann, Department of Physics and Astronomy, University of Delaware.

5.2.2 Compositional Analysis

The RBS output spectrum displays the total number, or counts, of ions that have been detected over an energy distribution. The energy with which the ions backscatter is dependent upon the target atom type and depth within the sample.

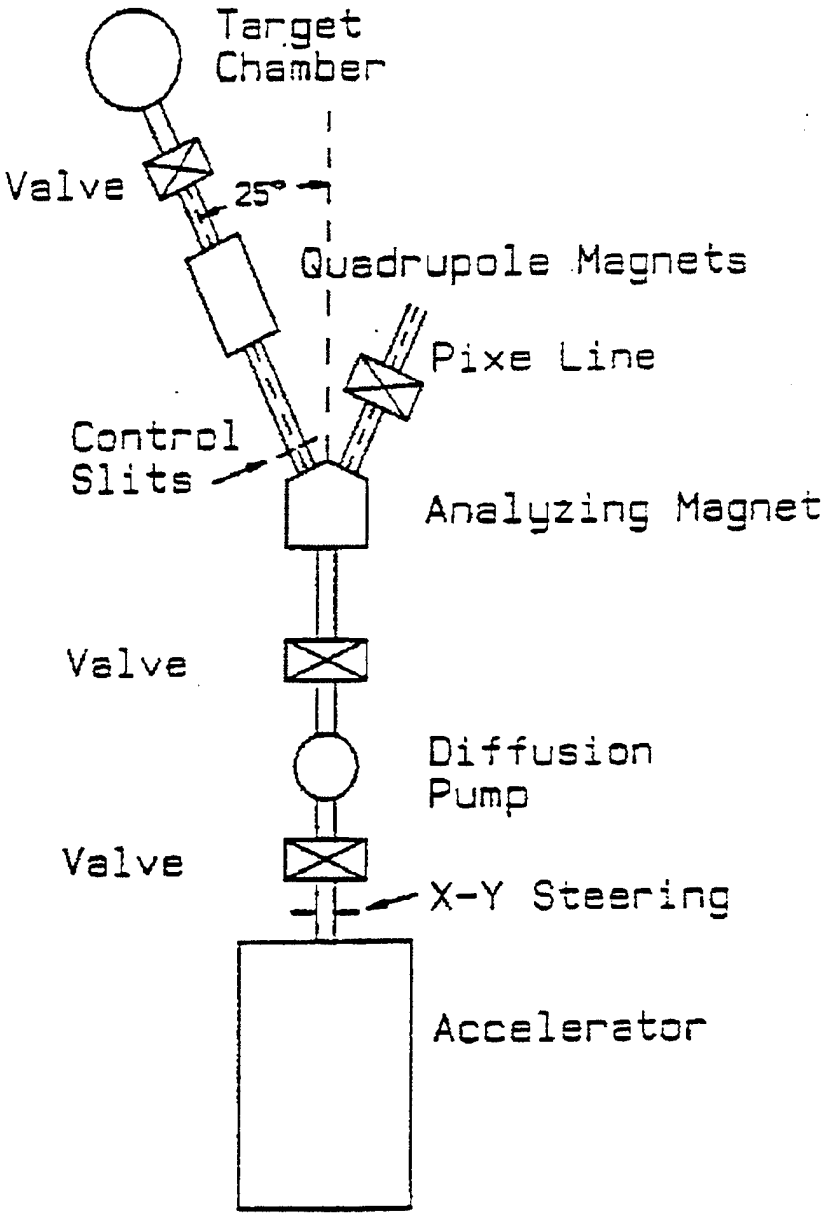

Figure 5.3: Diagram of University of Delaware's RBS system used for the collection of compositional data (Adapted from D. Beames [31]).

For example, a sample with a layer of silicon at the surface, germanium in the center, and a silicon substrate underneath will produce two silicon peaks separated in energy. The silicon substrate peak will appear at a lower energy in the spectrum than the silicon surface peak since ions that have scattered off of the substrate will have traveled further through the sample and will have lost a greater amount of energy. Without prior knowledge of the constituents of thick samples containing multiple layers, compositional analysis can be a difficult task.

The analysis of a sample's composition can be complicated by the overlapping in energy of spectral peaks usually found in thick multilayer samples. When a thick substrate is present, as is the case in epitaxial growth, a broad peak will appear in the spectrum. Characteristic peaks of elements of lighter mass than the substrate may appear at leading edge, falling edge, or atop the substrate spectral peak since the thick substrate has such a broad energy distribution. Ideally no peak overlap is desired. If overlap occurs, however, conventional compositional analysis can still be performed provided that the overlapping peaks ride on top of the broad spectral peak. If peaks overlap at the leading or falling edges, compositional analysis is performed by using simulation models.

5.2.2.1 Relative Peak Area

The most accurate method for obtaining composition from an RBS spectrum is through comparison of the relative characteristic peak areas obtained from the counts versus energy distribution associated with each constituent. Each peak represents the number of ions detected after backscattering off a particular element. This value can be equated to the actual number of target atoms per unit area by knowing the number of incident particles, the beam angle, and the scattering cross-section as shown in Equation (5.2).

$$A_i = \sigma_i \, \Omega \, Q \, N_i, \tag{5.2}$$

where,

A_i = Number of detected particles as determined from peak area (counts)

σ_i = Scattering cross-section

Ω = Beam angle illustrated in Figure 5.2 (Usually 170° to 175°).

Q = Number of incident particles (i.e., He ions)

N_i = Number of target atoms per unit area

i = Index of element in question.

For each element the average composition can be calculated from Equation (5.3), where n equals the number of elements in the material under analysis.

$$\% \; of \; Atom \; i \; = \; \frac{N_i}{\sum_{a=1}^{n} N_a}, \tag{5.3}$$

Since the number of incident particles, Q, and the beam angle, Ω, are constant throughout the data collection process, they will simply cancel out of Equation (5.3) upon calculation of the average composition. Therefore, the complete equation for determining the average composition is,

$$\% \; of \; Atom \; i \; = \; \frac{A_i/\sigma_i}{\sum_{a=1}^{n} A_a/\sigma_a.} \tag{5.4}$$

The spectra from which the calculations were performed are shown in Figures 5.4 and 5.5.

Carbon and oxygen peaks were present in both spectra and were detected at energies that coincided with the substrate. Since these peaks did not disrupt the leading or falling edge of the substrate peak, analysis of the sample compositions by Equation (5.4) was possible. The calculated number of counts for each peak

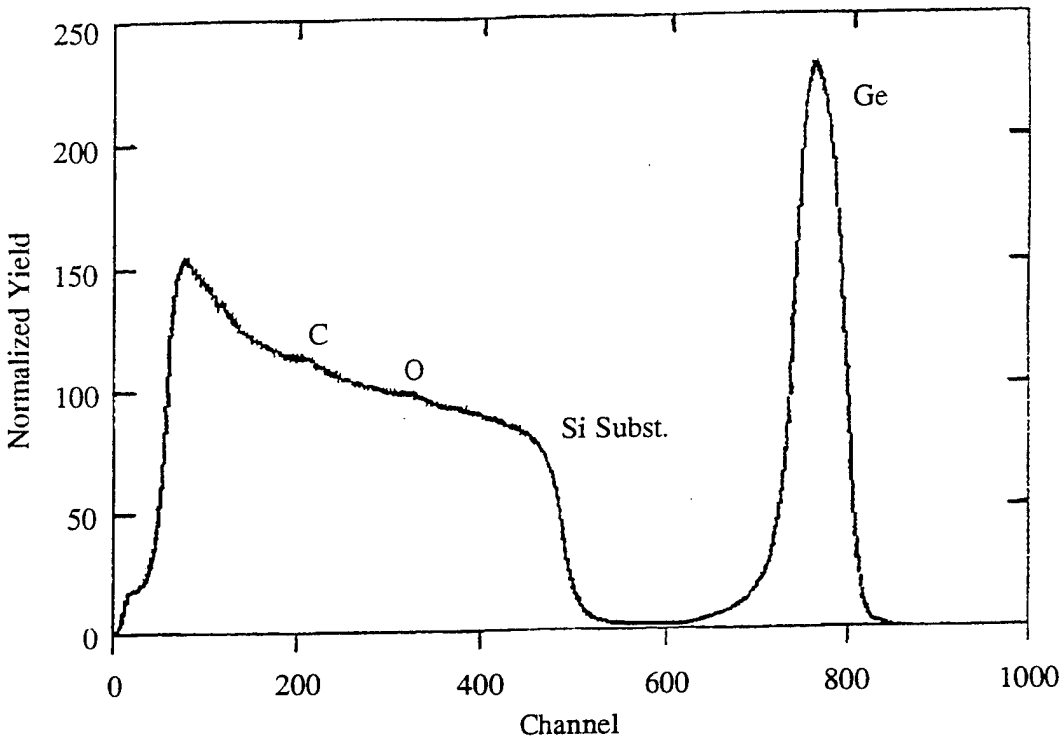

Figure 5.4: RBS spectra for germanium-carbon sample SGC-11, yielding the composition value: $Ge_{.634}C_{.253}O_{.113}$.

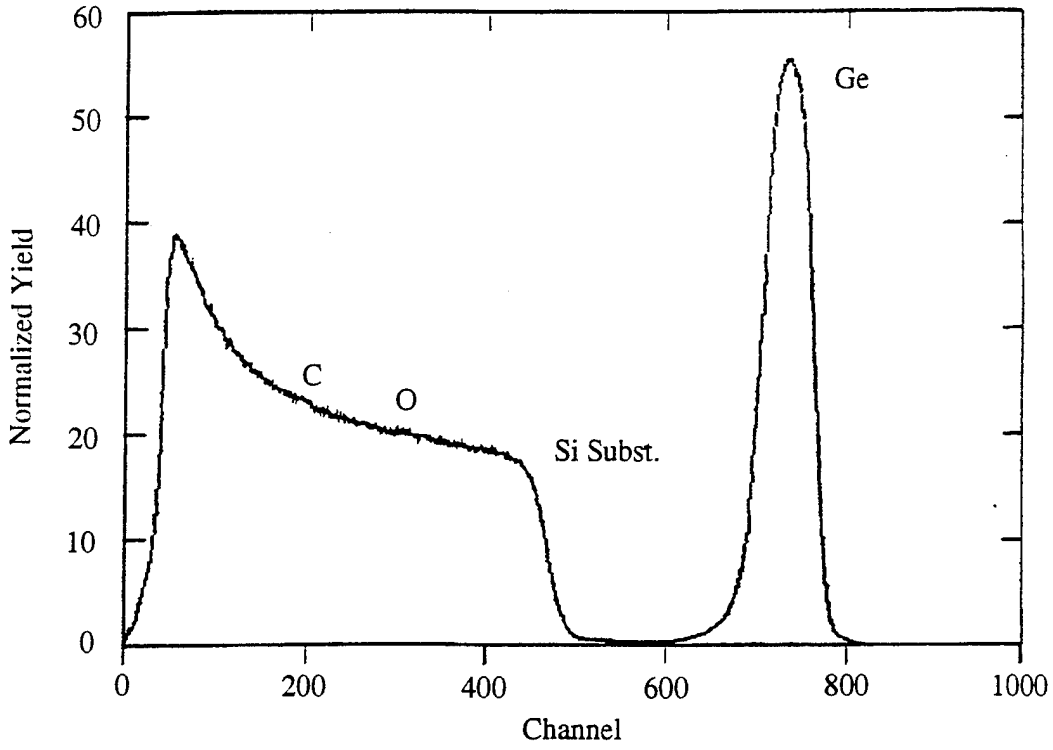

Figure 5.5: RBS spectra for germanium-carbon sample SGC-31, yielding the composition value: $Ge_{.836}C_{.138}O_{.026}$.

was determined by Dr. Charles Swann using graphical enlargement of each peak and subtraction of the substrate signal where necessary. Since the peaks attributing to light elements such as carbon and oxygen are inherently small in intensity, the compositions of samples with low concentrations of carbon, below about five percent, could not be accurately determined. The compositions of SGC-11 and SGC-31 have been calculated as shown in Table 5.3.

Table 5.3: Average compositions of SGC-11 and SGC-31 as determined by RBS.

Sample	% Germanium	% Carbon	% Oxygen
SGC-11	63.4	25.3	11.3
SGC-31	83.6	13.8	2.6

The contributions due to oxygen and the pure germanium buffer layer were removed from the RBS composition data since only the relative composition of the germanium-carbon epilayer was desired.

Table 5.4: Corrected RBS data of germanium-carbon samples which eliminates the percentage attributed to oxygen and the germanium buffer layer.

Sample	RBS Data	RBS, Omitting O	RBS, Omitting O and Buffer
SGC-11	$Ge_{0.634}C_{0.253}O_{0.113}$	$Ge_{0.715}C_{0.285}$	$Ge_{0.701}C_{0.299}$
SGC-31	$Ge_{0.836}C_{0.138}O_{0.026}$	$Ge_{0.858}C_{0.142}$	$Ge_{0.848}C_{0.152}$

Due to the presence of oxygen within both spectra, a pure germanium sample, SGC-10, was examined by RBS in order to determine if the oxygen was a product of the serpentine graphite filament. The spectra obtained for SGC-10 revealed no oxygen within the sample; therefore, based on the RBS data, it was concluded that the purity of the carbon source needed to be addressed.

5.2.2.2 Simulation Modeling for SiGeC Ternary Alloys

When examining RBS spectra of thin silicon-germanium-carbon layers, the silicon within the epitaxial layer becomes indistinguishable from the silicon substrate due to interference with the substrate leading edge. As a result, compositional analysis by the conventional method of peak area comparison becomes difficult to near impossible. Under these circumstances a simulation program, RUMP, that was developed by L. R. Doolittle under the advisement of J. W. Mayer at Cornell University, is utilized to determine the sample composition [32].

RBS spectra for silicon-germanium-carbon samples SGC-19 and SGC-20 were measured and compared with simulation spectra of varying known compositions. The carbon concentrations within the silicon-germanium-carbon samples were below the resolution of the simulator so that variations in carbon concentrations from zero to ten percent produced little effect in the shape of the simulated spectra. A ratio, however, of silicon to germanium could be obtained from the model. Samples SGC-19 and SGC-20 exhibited similar spectra from RBS analysis. Upon simulation both samples produced silicon to germanium composition ratios of 1 to 11. The experimental and simulated spectra for SGC-19 are shown in Figure 5.6. The simulated spectra was produced by modeling a 5500 Å $Si_{0.08}Ge_{0.88}C_{0.04}$ on a 50000 Å thick silicon substrate. Due to low carbon concentrations, the simulations of the silicon-germanium-carbon alloys gave only the *ratio* of silicon to germanium. This simulated silicon to germanium composition ratio, however, is valid for any carbon concentration and provides useful information toward the determination of the absolute composition. The compositions of SGC-19 and SGC-20 as determined by RBS can be represented as, $Si_xGe_{11x}Cy$. In order to determine the average compositions for these samples, additional information is required and will be discussed in further detail within a later section.

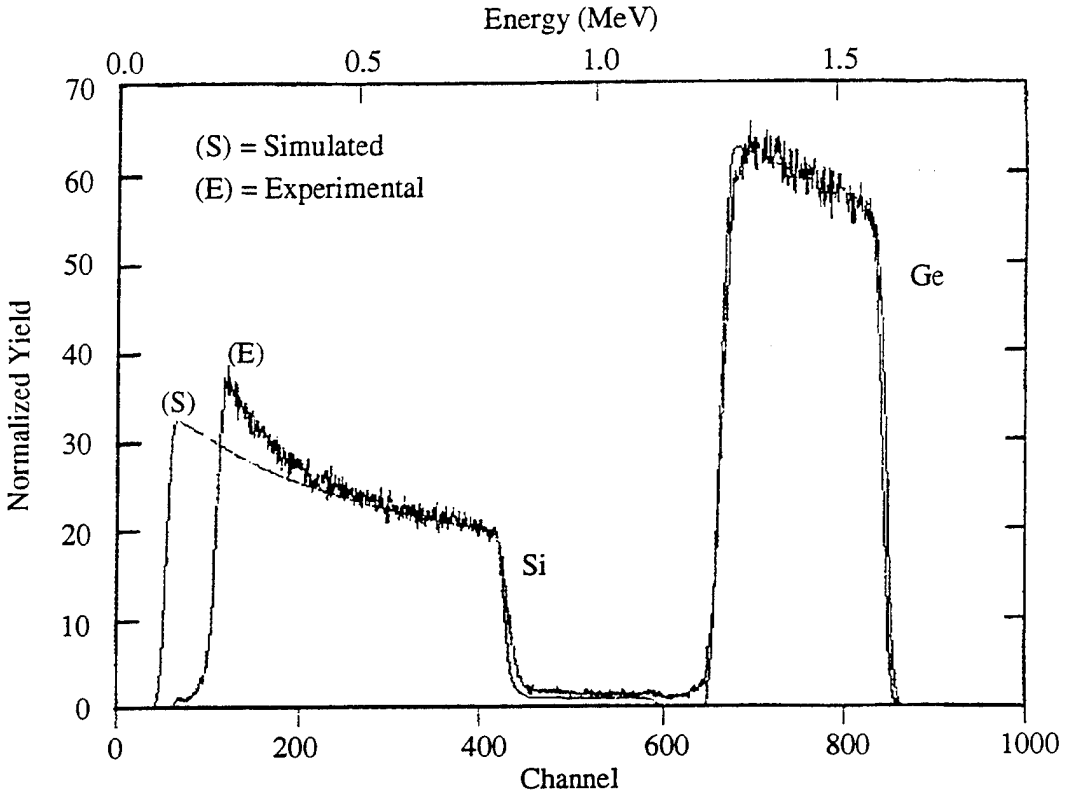

Figure 5.6: RBS experimental and simulated spectra for silicon-germanium-carbon sample SGC-19.

In order to determine the accuracy of the simulation model, two silicon-germanium alloys of known composition were analyzed. These two samples, IBM-27 and IBM-28, were provided by Dr. S. Iyer. The original compositions were determined at IBM by x-ray diffraction and optimized simulations of the two samples were obtained using the composition values of Table 5.5.

Table 5.5: Compositions of IBM-27 and IBM-28 as determined by x-ray diffraction at IBM and RBS simulations at the University of Delaware.

Sample	X-ray		RBS	
	% Germanium	% Silicon	% Germanium	% Silicon
IBM-27	7	93	8	92
IBM-28	22	78	22	78

The RBS simulations produced similar compositions as found with x-ray analysis. As shown in a prior section, IBM-27 had been analyzed by AES and produced a germanium composition of 7.7%. Upon comparison with RBS analysis, the two techniques produced similar germanium fractions. Through this additional analysis of known silicon-germanium "standards," compositional analysis by RBS simulation has proven to be reasonably accurate.

5.3 Estimation of Composition by Growth Rates

In order to obtain absolute composition values for the silicon-germanium-carbon alloys and the low carbon concentration germanium-carbon alloys, additional information is required. By using the estimated carbon growth rates and epilayer thicknesses, average compositions of all samples can be determined. As mentioned in Chapter 3, the carbon growth rate versus carbon filament temperature and current was found using the RBS data from SGC-31 and SGC-11 and the epilayer thickness. All samples were grown at one of the five carbon currents listed in Table 5.6.

Table 5.6: Carbon currents, temperatures and growth rates for growth with the serpentine carbon filament.

Serpentine Carbon Filament Conditions		
Current (A)	Temperature (C)	Growth Rate (μm/hr.)
35	1939	$7.40\text{x}10^{-4}$
36	1970	$1.35\text{x}10^{-3}$
37	2001	$2.30\text{x}10^{-3}$
38	2031	$4.33\text{x}10^{-3}$
40	2091	$1.24\text{x}10^{-2}$

From the carbon growth rate data and Equations (5.5) and (5.6), the average compositions of the germanium-carbon alloy layers, exclusive of any pure germanium buffer layer growth, was found for each sample that had a measurable epilayer thickness. The oxygen concentrations were factored out of the RBS data to represent the correct composition ratio of only germanium and carbon. The atomic carbon fraction is given by:

$$X_C = \left[\frac{d_C/a_C}{d_C/a_C + d_{Ge}/a_{Ge}}\right], \tag{5.5}$$

where,

$$d_C = G_C/t \quad and \quad d_{Ge} = \frac{(d - d_C)\,t}{t - t_b}, \tag{5.6}$$

and,

X_C = Carbon atomic fraction — d_C = Partial layer thickness of C in GeC

a_C = Carbon lattice constant — d_{Ge} = Partial layer thickness of Ge in GeC

a_{Ge} = Germanium lattice constant — d = Total layer thickness

t = Duration of total growth — t_b = Duration of buffer layer growth.

The compositions of the germanium-carbon alloy as predicted by growth rate analysis are listed in Table 5.7.

Table 5.7: Average composition of Ge_xC_{1-x} by RBS and growth rate calculations.

Sample	Composition	Analysis Method
SGC-11	$Ge_{0.701}C_{0.299}$	RBS, Omitting Buffer
SGC-17	$Ge_{0.991}C_{0.009}$	Carbon Growth Rate
SGC-18	$Ge_{0.974}C_{0.026}$	Carbon Growth Rate
SGC-21	$Ge_{0.993}C_{0.007}$	Carbon Growth Rate
SGC-23	$Ge_{0.978}C_{0.022}$	Carbon Growth Rate
SGC-24	$Ge_{0.987}C_{0.013}$	Carbon Growth Rate
SGC-27	$Ge_{0.993}C_{0.007}$	Carbon Growth Rate
SGC-28	$Ge_{0.977}C_{0.023}$	Carbon Growth Rate
SGC-30	$Ge_{0.962}C_{0.038}$	Carbon Growth Rate
SGC-31	$Ge_{0.848}C_{0.152}$	RBS, Omitting Buffer
SGC-32	$Ge_{0.848}C_{0.152}$	Carbon Growth Rate

Calculation of the silicon-germanium-carbon compositions of SGC-19 and SGC-20, proved to be a much more difficult task. Using the layer thickness. the carbon growth rate data, and the 1:11 silicon to germanium composition ratio determined by RBS, an average composition was determined. Unlike the germanium-carbon alloys in which the germanium buffer could be easily removed following the analysis, the compositions determined for the silicon-germanium-carbon alloys included the 15 minute silicon buffer layer of approximately 40 Å. By modifying Equation (5.5) to include silicon and germanium RBS fractions, the compositions of SGC-19 and SGC-20 were estimated as follows:

$$X_C = \left[\frac{d_C/a_C}{d_C/a_C + 11x + x}\right], \tag{5.7}$$

where,

$$d_C = G_C/t \quad and \quad x\,a_{Si} + 11x\,a_{Ge} + d_C = d \tag{5.8}$$

and,

a_C = Carbon lattice constant

a_{Ge} = Germanium lattice constant

x = Normalized thickness for silicon, d_{Si}/a_{Si}

Table 5.8: Average composition of $Si_{1-x-y}Ge_xC_y$ by RBS and growth rate calculations. The silicon-germanium-carbon compositions do not show an 11 to 1 ratio of germanium to silicon due to rounding errors.

Sample	Composition	Analysis Method
SGC-19	$Si_{0.082}Ge_{0.896}C_{0.022}$	RBS Simulation; Carbon Growth Rate
SGC-20	$Si_{0.082}Ge_{0.904}C_{0.014}$	RBS Simulation; Carbon Growth Rate

The low value of silicon concentration in SGC-19 and SGC-20 resulted from a shortage of silicon in the crucible. Based on the silicon-germanium-carbon, Vegard's Law would predict that the epitaxial layer of SGC-19 and SGC-20 would not be lattice matched to the silicon substrate as originally intended.

5.4 Estimation of Composition by Incorporation Rates

In order to eliminate possible error in the composition calculations that may occur using carbon growth rates, the sample compositions were recalculated using incorporation rates based on vapor pressure curves. For germanium, the incorporation rate was determined from a pure sample, SGC-10; for carbon, the incorporation rates were inferred from RBS measurements of the germanium-carbon layer SGC-11.

5.4.1 Determination of Incorporation Rates

The germanium incorporation rate for SGC-11 was determined using germanium vapor pressure data, the growth rate of germanium for SGC-10, and the germanium atomic density. The incorporation rate for germanium at a growth temperature of 1350°C was found by multiplication of the corresponding growth rate

and atomic density. Since germanium flux is proportional to vapor pressure, the incorporation rate at any germanium growth temperature could be determined from published vapor pressure versus temperature curves.

In order to determine the incorporation rates of carbon, the corresponding germanium incorporation rate for sample SGC-11 was found and utilized along with relative carbon and germanium compositions calculated from RBS. All other carbon incorporation rates were calculated using vapor pressure data. All germanium-carbon sample compositions were found from the relative calculated incorporation rates of germanium and carbon. The incorporation rates of germanium and carbon found for each growth condition have been listed in Table 5.9.

Table 5.9: Incorporation rates of carbon and germanium for all sample growth conditions

Source	Current (A)	Incorporation Rate (Atoms/cm^2·s)
Germanium	8.23	2.07×10^{14}
Carbon	40	2.55×10^{13}
Carbon	38	9.63×10^{12}
Carbon	37	5.50×10^{12}
Carbon	36	3.00×10^{12}
Carbon	35	1.65×10^{12}

5.4.2 Composition by Relative Incorporation Rates

The compositions of the germanium-carbon alloy samples were calculated from the incorporation rates of Table 5.9 and Equation (5.9). The final compositions have been determined and tabulated in Table 5.10.

$$X_C = \left[\frac{f_C}{f_C + f_{Ge}}\right], \tag{5.9}$$

where,

f_C = Carbon incorporation rate

f_{Ge} = Germanium incorporation rate.

Table 5.10: Average composition of Ge_xC_{1-x} by RBS and incorporation rate calculations where the composition analysis method used is indicated.

Sample	Composition	Analysis Method
SGC-11	$Ge_{0.701}C_{0.299}$	RBS, Omitting Buffer
SGC-17	$Ge_{0.986}C_{0.014}$	Incorporation Rate
SGC-18	$Ge_{0.974}C_{0.026}$	Incorporation Rate
SGC-21	$Ge_{0.992}C_{0.008}$	Incorporation Rate
SGC-23	$Ge_{0.974}C_{0.026}$	Incorporation Rate
SGC-24	$Ge_{0.986}C_{0.014}$	Incorporation Rate
SGC-27	$Ge_{0.992}C_{0.008}$	Incorporation Rate
SGC-28	$Ge_{0.974}C_{0.026}$	Incorporation Rate
SGC-29	$Ge_{0.956}C_{0.044}$	Incorporation Rate
SGC-30	$Ge_{0.956}C_{0.044}$	Incorporation Rate
SGC-31	$Ge_{0.848}C_{0.152}$	RBS, Omitting Buffer
SGC-32	$Ge_{0.848}C_{0.152}$	Incorporation Rate

Compositional analysis by incorporation rate evaluation involves making several reasonable assumptions which would not greatly affect the outcome of the calculations. The most crucial assumption involved the accuracy of the germanium incorporation rate. Since all germanium-carbon samples after SGC-11 were grown without knowledge of the actual germanium source temperature, the assumption of a constant germanium incorporation rate of 9.24×10^{13} atoms/(cm^2 sec) may not be valid. The source current, however, was monitored and assumed to produce equal germanium flux for all germanium growth currents between 8.22 and 8.27 Amps. Due to a cracked crucible which could potentially cause rapid germanium depletion, the actual flux more than likely decreased between growths of SGC-17 and SGC-32. Upon removal of the germanium source, however, the extent of depletion was not significant enough to invalidate this assumption. The next most

significant assumption involved the incorporation rates determined for the carbon source. The incorporation rates determined for carbon were based on vapor pressures and RBS compositions. The nominal vapor pressure values were found for specific carbon filament temperatures. Since the relation between filament current and temperature is based on a theoretical calculation as given in section 3.2.3.1, the actual experimental carbon vapor pressures may have differed from those which had been assumed. The final assumption involves the sticking coefficient for incorporation of both germanium and carbon. In order to empirically fit a vapor pressure trend to the incorporation rate data, the sticking coefficient of each element must be independent of source temperature and flux.

Analysis of silicon-germanium-carbon alloys SGC-19 and SGC-20 is performed similarly to that of germanium-carbon with the addition of the RBS silicon to germanium composition ratio. Since the silicon to germanium composition ratio was found by RBS to be 1 to 11, the silicon incorporation rate would equal one-eleventh the germanium incorporation rate, or 1.88×10^{13}. The average composition of SGC-19 and SGC-20 was determined using Equation (5.10) as follows:

$$X_C = \left[\frac{f_C}{f_C + f_{Ge} + f_{Si}} \right], \tag{5.10}$$

where,

f_C = Carbon incorporation rate

f_{Ge} = Germanium incorporation rate

f_{Si} = Silicon incorporation rate.

The compositions of silicon-germanium-carbon samples SGC-19 and SGC-20 as determined by incorporation rate calculations and Equation (5.10) are listed in Table 5.11.

Table 5.11: Average composition of $Si_{1-x-y}Ge_xC_y$ by RBS and incorporation rate calculations. The silicon-germanium-carbon compositions do not show an 11 to 1 ratio of germanium to silicon due to rounding errors.

Sample	Composition	Analysis Method
SGC-19	$Si_{0.081}Ge_{0.895}C_{0.024}$	RBS Simulation; Incorporation Rate
SGC-20	$Si_{0.082}Ge_{0.905}C_{0.013}$	RBS Simulation; Incorporation Rate

5.5 Comparison of Alloy Compositions as Determined by Growth Rates and Incorporation Rates

The alloy compositions determined by growth rate and incorporate rate calculations have been tabulated in Table 5.12.

Table 5.12: Average composition of Ge_xC_{1-x} and $Si_{1-x-y}Ge_xC_y$ by growth rate and incorporation rate calculations. Growth rate calculation of SGC-29 could not be performed since epilayer thickness was not measurable.

Sample	Growth Rate	Incorporation Rate
SGC-17	$Ge_{0.991}C_{0.009}$	$Ge_{0.986}C_{0.014}$
SGC-18	$Ge_{0.974}C_{0.026}$	$Ge_{0.974}C_{0.026}$
SGC-19	$Si_{0.082}Ge_{0.896}C_{0.022}$	$Si_{0.081}Ge_{0.895}C_{0.024}$
SGC-20	$Si_{0.082}Ge_{0.904}C_{0.014}$	$Si_{0.082}Ge_{0.905}C_{0.013}$
SGC-21	$Ge_{0.993}C_{0.007}$	$Ge_{0.992}C_{0.008}$
SGC-23	$Ge_{0.978}C_{0.022}$	$Ge_{0.974}C_{0.026}$
SGC-24	$Ge_{0.987}C_{0.013}$	$Ge_{0.986}C_{0.014}$
SGC-27	$Ge_{0.993}C_{0.007}$	$Ge_{0.992}C_{0.008}$
SGC-28	$Ge_{0.977}C_{0.023}$	$Ge_{0.974}C_{0.026}$
SGC-29	———	$Ge_{0.956}C_{0.044}$
SGC-30	$Ge_{0.962}C_{0.038}$	$Ge_{0.956}C_{0.044}$
SGC-32	$Ge_{0.986}C_{0.014}$	$Ge_{0.848}C_{0.152}$

Upon comparison of the alloy compositions obtained from the two calculation methods, the values found for growth rate analysis were less than or equal to those found using the incorporation rate analysis procedure. Variations in composition

between the two methods may have occurred as a result of the various required assumptions. For example, in order to utilize carbon growth rates for compositional analysis, it was assumed that all of the carbon within the epilayer had incorporated at substitutional sites within the lattice. Furthermore, the calculations were dependent upon the accuracy of the epilayer thickness measurement. For incorporation rate calculations, in order to determine the alloy compositions it was necessary to assume a constant germanium flux throughout the growths of SGC-10 through SGC-32. Furthermore, the carbon filament temperature which was used to calculate carbon incorporation rate was based on a theoretical calculation and therefore may have been inaccurate. Despite these assumptions, either compositional analysis technique is within the expected experimental error and could be used to determine alloy composition. For consistency, however, the composition values as determined by relative incorporation rates will be the preferred compositional method. This method has been chosen since an accurate layer thickness of each sample is not required and the placement of the carbon atoms at substitutional sites within the lattice is not assumed. Future compositional analysis of MBE grown alloy layers should be performed utilizing this method in order to maintain a consistent compositional evaluation method.

5.6 Carbon Segregation

For each sample, the compositional data obtained from RBS spectrum and calculations of rate equations has described the average composition over the total thickness of the alloy layer. As is evident from the high surface concentration of carbon in layer SGC-11 as obtained from AES, there exists a possibility of carbon segregation toward the sample surface. In order to determine the depth profile of carbon rich samples such as SGC-11, extensive RBS simulation and Secondary Ion Mass Spectrometry (SIMS) has been performed. The SIMS measurements were performed by Dr. Phillip Thompson at the Naval Research Laboratory.

5.6.1 RBS Simulation of Carbon Depth Profile

Using the average composition values obtained from relative peak area calculations of the experimental RBS spectrum of SGC-11, a simulation model was developed to test the compositional uniformity or the alloy layer. The model was composed of a 1500 Å layer of $Ge_{0.634}C_{0.253}O_{0.113}$ on a 30000 Å silicon substrate. As shown in Figure 5.7, the simulation does not accurately depict the germanium and silicon peaks. The edges of the simulation peaks are sharp whereas the edges of the RBS spectrum peaks are more gradually sloped.

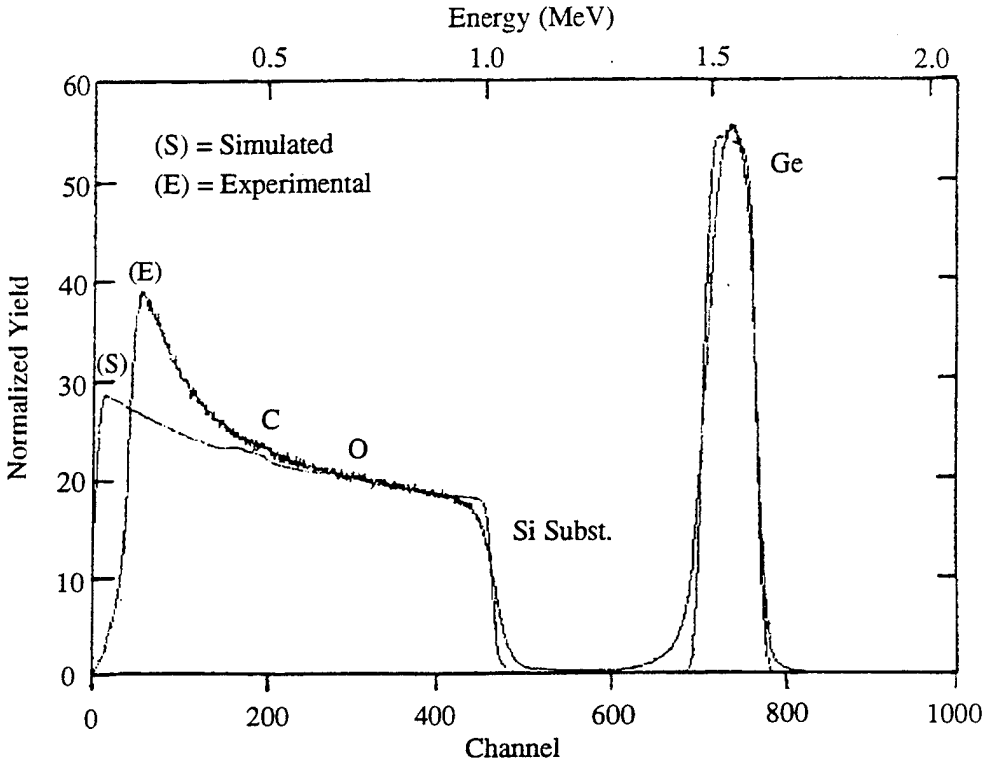

Figure 5.7: RBS experimental and simulated spectra using average, peak area composition for germanium-carbon sample SGC-11.

The spreading of the spectral peaks could have occurred as a result of density variations within the sample. For example, an epilayer model of constant composition and given thickness would be simulated using a constant atomic density. The

peaks in the simulated spectrum would be sharp due to clean abrupt interfaces. If however, variations in the composition or interdiffusion of the sample layers occurred, the spectral peaks would be sloped accordingly. For germanium-carbon on silicon, a sloped leading or high energy edge for the germanium peak would imply deficiency of germanium at the surface. For a sloped falling or low energy edge, however, the change in peak shape could be a result of a gradual decrease in germanium before the interface or interdiffusion between the silicon substrate and germanium in the epilayer. A simulation model was developed which accurately fit the spectral response of SGC-11 as obtained from RBS. The depth profiling schedule that was modeled is listed in Table 5.13.

Table 5.13: Depth profiling schedule used for RBS simulation model of germanium-carbon alloy SGC-11.

Thickness (Å)	% Germanium	% Oxygen	% Carbon	% Silicon
75	10	10	80	0
100	15	10	75	0
125	20	10	70	0
150	30	10	60	0
175	40	9	51	0
225	55	7	38	0
600	65	5	30	0
100	70	2	18	10
100	60	0	10	30
125	50	0	5	45
150	40	0	0	60
250	25	0	0	75
300	15	0	0	85
400	8	0	0	92
500	5	0	0	95
30000	0	0	0	100

The layer simulation that most closely depicted the experimental spectrum incorporated carbon and oxygen segregation toward the epilayer surface (or likewise

germanium segregation toward the interface) and interdiffusion between the germanium and silicon substrate. To within reasonable accuracy, the simulation model accounted for the unusual grading in both edges of the germanium and silicon peaks. It must be noted, however, that the ratio of carbon and oxygen may vary with position since only a decrease in the concentration of germanium at the surface was required to model the germanium leading edge. The sample has been modeled as multiple thin layers of varying compositions.

As can be seen from Figure 5.8, the germanium and silicon simulated and experimental spectral peaks sufficiently matched one another by simulation of epilayer segregation; carbon and oxygen segregated toward the epilayer surface whereas germanium segregated toward the substrate interface. The overshoot in the experimental silicon substrate peak at the falling edge is a direct result of the sample charging during the measurement and is not an error in the simulation model.

The simulated peak areas (in yield versus energy) representing the amount of carbon and oxygen in the epilayer are of greater intensity than the peaks directly obtained from RBS analysis. These variations in the simulated and experimental carbon and oxygen peaks suggest that the simulation is not including an additional chemical element within the film. Simulations of layers including germanium, carbon, oxygen, and hydrogen have been performed; however, substitution of carbon and oxygen with hydrogen has produced a sharper germanium leading edge than was experimentally determined.

From Figure 5.8, it can be concluded that the combination of the multiple layers in Table 5.13 produced a step-wise depth profiling which approximated the segregation trends of sample SGC-11. By averaging the stepped composition profile of Table 5.13 used for RBS simulation, a more realistic illustration of the estimated depth profile of SGC-11 was obtained as shown in Figure 5.9.

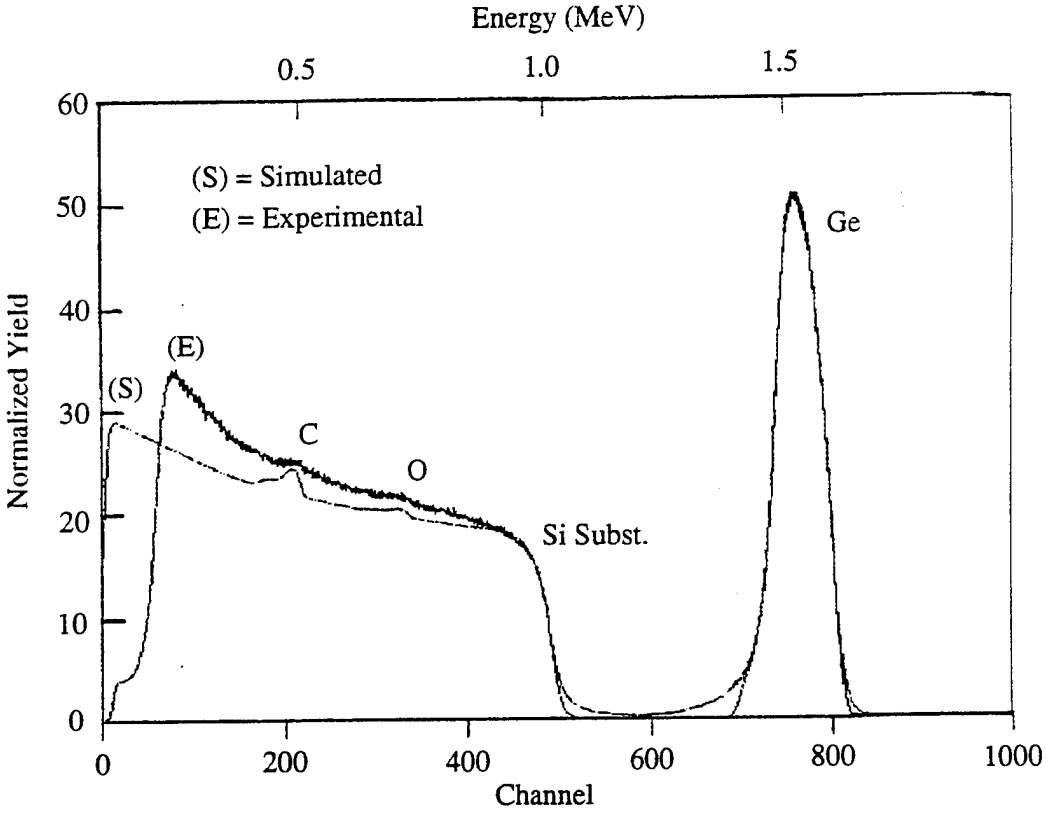

Figure 5.8: RBS experimental and simulated spectra for germanium-carbon sample SGC-11. The depth profile indicated in Table 5.14 was used as the simulation model.

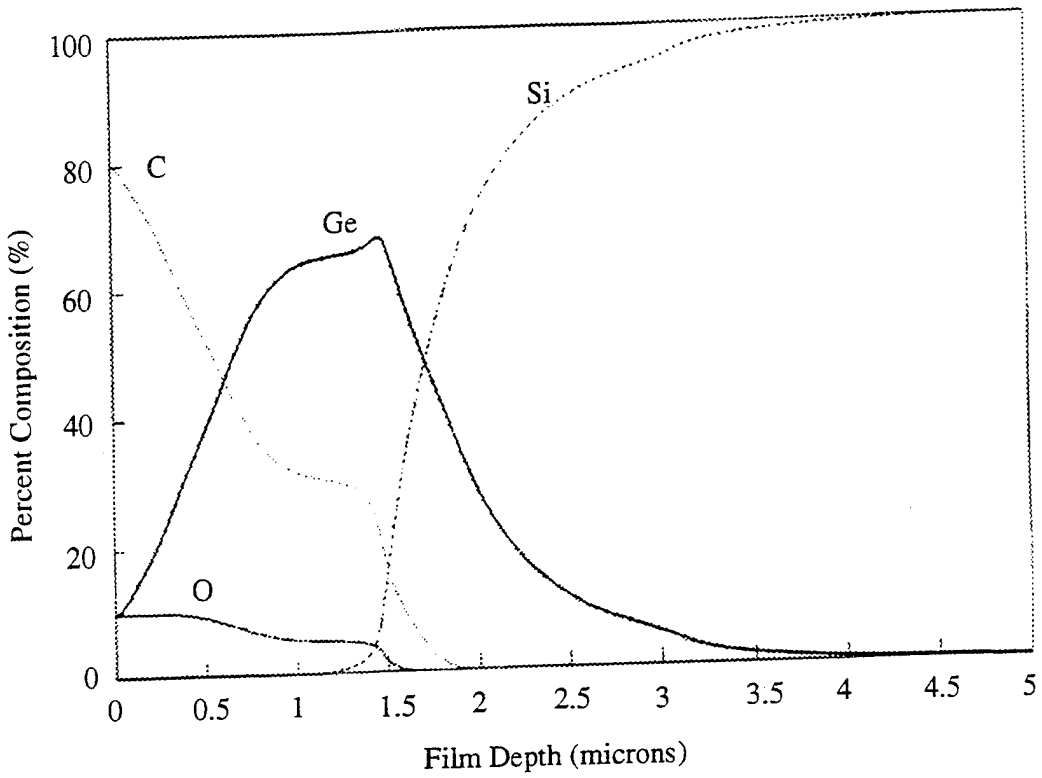

Figure 5.9: Graphical depth profiling of germanium-carbon alloy SGC-11 as determined by RBS simulation.

Similar segregation trends have been observed in RBS simulations of other high carbon concentration germanium-carbon samples such as SGC-31 and SGC-32. Carbon segregation may therefore appear in all germanium-carbon epitaxial growth but remains detectable by RBS at high levels of carbon concentration only. In order to determine the extent of carbon segregation and interfacial diffusion, further depth profiling analysis by more accurate means has been performed with SGC-11, $Ge_{0.634}C_{0.253}O_{0.113}$, and SGC-32, $Ge_{0.836}C_{0.138}O_{0.026}$.

5.6.2 SIMS Analysis

Additional depth profiling was performed by Dr. Phillip Thompson at the Naval Research Laboratory (NRL), using Secondary Ion Mass Spectrometry (SIMS). This technique uses an ion beam that sputters the sample surface. Secondary ions

from the sputtering process are collected in a mass spectrometer and separated according to mass to charge ratio. This technique allows for examination of selected elements versus sputtering time in order to determine a depth profile. Three setbacks, however, exist with the analysis of germanium-carbon-oxygen films by SIMS. Quantitative information is difficult to achieve since several standards of varying concentrations are required and germanium-carbon is not readily found. Furthermore, sputtering occurs unevenly, pitting the surface in a selected region. The sputtered elements may not be completely cleared away and elements which reside only near the surface of the sample may be detected as if at greater depths. Lastly, NRL uses oxygen as the ion beam source and therefore oxygen can not be detected in any sample. This is a major disadvantage since oxygen has been discovered in the germanium-carbon layer SGC-11 and SGC-31 by RBS and the profiling of this element will not be able to be observed.

As with the RBS simulations, the SIMS profile of SGC-11 as shown in Figure 5.10 indicates carbon surface segregation and interfacial diffusion of silicon and germanium. In addition to analysis of SGC-11, SIMS was performed on SGC-32, a lower carbon concentration sample, in which segregation of carbon was not apparent. Despite the lack of carbon segregation in the SIMS profile of SGC-32, interdiffusion of silicon and germanium was observed. Overall, clear evidence does exist from RBS simulations and SIMS analysis indicating nonuniform compositions due to both carbon segregation and/or interfacial diffusion in selective samples.

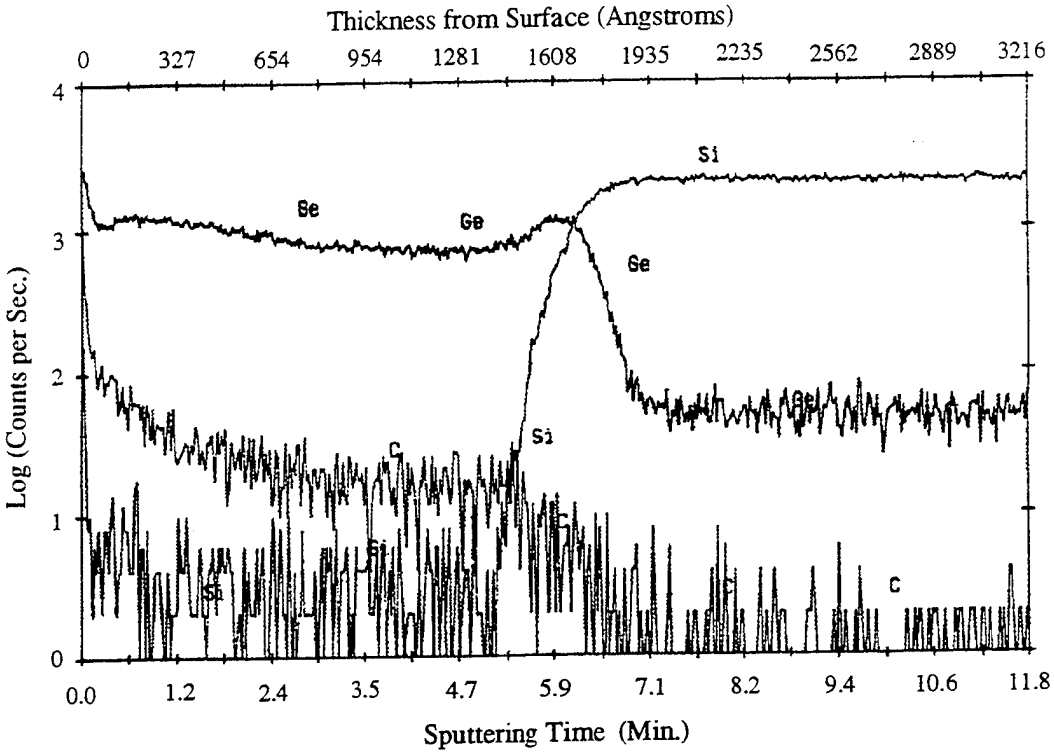

Figure 5.10: SIMS profile for germanium-carbon sample SGC-11. Profile indicates carbon surface segregation and interfacial diffusion.

Chapter 6

CONCLUSION

6.1 Conclusions

The development of a silicon lattice-matched alloy, such as silicon-germanium-carbon, may one day advance silicon heterojunction technology and provide for new silicon optoelectronic devices. Presently, however, this material is in its infancy. In order to determine the potential of silicon-germanium-carbon or any new material, extensive growth optimization and material characterization must be performed.

The first silicon-germanium-carbon and germanium-carbon alloys at the University of Delaware have been successfully grown by molecular beam epitaxy. The growth of these materials is considered an achievement in itself since the newly purchased MBE system had not been put into operation prior to this project. As described in this Thesis, extensive research has been performed toward optimizing the growth of silicon, germanium, and carbon by varying silicon source crucibles, carbon filament designs, and substrate growth temperatures. Compositional analysis, x-ray diffraction, and surface microscopy techniques were utilized in order to optimize the source and substrate growth conditions.

Further characterization of the carbon source was performed by investigation of carbon evaporation from two graphite filament designs, the serpentine and WWR graphite filaments. The serpentine filament provided adequate carbon growth but compromised the purity of the epitaxial layers. In addition to carbon, significant quantities of oxygen were adsorbed into the epilayer. The WWR filament was then

designed and developed from high purity Union Carbide graphite and is expected to produce higher carbon growth rates at equivalent filament temperatures. Growth with this new filament design has yet to be performed; therefore, the growth rate predictions have not been experimentally tested. The growth mechanisms of both filaments have been investigated, however, by measurement of the carbon cracking pattern at approximately 2090°C. The results obtained from both filaments provided direct evidence of trimeric carbon, C_3, in the molecular beam. This result is significant since molecular grouping may promote clustering of carbon within the epitaxial layer and prevent the growth of a perfectly random alloy. Based on these findings, the nature of carbon evaporation from the graphite filament and its effects on alloy growth merits even further investigation.

Additional growth characterization by optical microscopy and SEM provided information as to growth optimization and surface morphology of layers grown at various substrate temperatures. By examination of the layers' surfaces, optimum growth temperatures of 400°C to 600°C produced specular, smooth epilayer surfaces in germanium and germanium-carbon samples. An optimum substrate temperature range has not yet been determined for silicon-germanium-carbon since only two samples were grown at 400°C. Optimum growth, however, of the ternary alloy, would be expected to occur at higher temperatures than 400°C since pure silicon is grown at 700°C.

Calculated molecular growth rates and incorporation rates have provided valuable information in regards to compositional analysis of germanium-carbon and silicon-germanium-carbon alloys. The relative growth and incorporation rates have been used to provide the average epilayer compositions for low carbon concentration alloys. For layers containing a relatively large percentage of carbon, above five percent, Rutherford Backscattering Spectrometry (RBS) was used to determine the average composition. Auger Electron Spectroscopy (AES) was initially attempted

to provide alloy compositions. The system lacked adequate sputtering capabilities and therefore the carbon surface contamination compromised the integrity of the results for germanium-carbon and silicon-germanium-carbon alloys. Furthermore, as discovered with RBS, the compositions of the higher carbon concentration alloys, were not uniform. As was detected by AES, the alloy surface contained a significant percentage of carbon. For this reason the average composition of the alloy layers could not be determined using a surface analysis technique such as AES. Using RBS, however, the average epilayer composition could be determined by comparison of the relative peak areas (number of counts) of each element in the layer. In addition, depth profiling could still be performed with RBS by creating a simulation model. From the model, the alloy composition could be estimated throughout the thickness or depth of the layer. It was by this method that carbon segregation and interfacial diffusion of selective carbon-rich samples was initially discovered. For verification of the profile obtained from the RBS simulation model, further depth profiling by Secondary Ion Mass Spectroscopy (SIMS) was performed and confirmed the presence of segregation and interdiffusion in at least one of the germanium-carbon alloys, SGC-11.

In order to determine if the alloys grown were lattice-matched to silicon, x-ray diffraction was used to follow the effect of the carbon concentration on the alloy lattice parameter. For all germanium-carbon samples, the epilayer intensity peak was positioned at about the 2θ value corresponding to the germanium lattice constant. In other words, the carbon appeared to have an insignificant effect on the alloy lattice parameter. Upon annealing, however, the 2θ epilayer peak of the germanium-carbon sample SGC-31 increased, shifting toward the silicon substrate peak. Verification of carbon incorporation at substitutional sites within the germanium lattice would suggest a new scientific finding and certainly merits further investigation.

6.2 Future Work

Further growth of group IV alloys needs to be performed in order to map the properties of silicon-germanium-carbon and germanium-carbon as a function of composition. A majority of the growth optimization and characterization has been performed and will prove useful in these future growths. Since a reliable means of compositional analysis has been determined for all ranges of carbon concentrations, the composition of any new sample may be determined by the appropriate methods as described in Chapter 5. After achieving a full composition range of germanium-carbon or silicon-germanium-carbon samples, a variety of material properties such as bandgap, photoluminescence, infrared absorption, and lattice parameter may be analyzed versus composition. Due to the 2θ epilayer peak shifts present in the x-ray diffraction patterns of selective annealed samples as discovered by S. Zhang, further annealing experimentation should be investigated in attempt to produce silicon lattice-matching. The observed shift did, however, correspond to a lesser carbon content than was experimentally found. This finding raises two questions: Is the additional carbon residing at interstitial and/or other locations and producing no displacement in the lattice or does Vegard's Law not hold for this new alloy? Structural analysis by TEM or investigation of carbon bonding by FTIR vibrational mode absorption may uncover these unresolved questions. A better understanding of the carbon bonding mechanism within germanium-carbon and silicon-germanium-carbon is required in order to determine the true composition of carbon necessary for silicon lattice-matching.

Appendix A

AUGER ELECTRON SPECTROSCOPY USER'S GUIDE: EVANS ROOM 148

A.1 Sample Loading

1. Cool sorption pumps with LN_2 to prepare for later use.
2. Turn off ion gauge filament at gauge controller.
3. Attach vacuum gauge to the "T.C. Control Panel" located in the right blue equipment rack.
4. Close main valve in rear of vacuum chamber to close off ion pump. (Make sure pump controller is in protect mode in case of a leak.)
5. Open nitrogen gas regulator.
6. Open shut-off valve to roughing line and wait for pressure read by T.C. Control Panel to reach "ATM", atmospheric pressure.
7. Slowly open gold-seal valve to vent chamber - pressure read by T.C. Control Panel will decrease and then rise to ATM when the chamber is vented.
8. Remove loading flange (manipulator) and attach samples(s).
9. Replace gasket and seal flange closed.
10. Close nitrogen shut-off valve at roughing line.

11. Close regulator.

12. Open first sorption for approximately 1 minute and then close.

13. Open second sorption.

14. Note when T.C. Control Panel reads minimum pressure.

15. Wait 15 more minutes and then close gold-seal valve connecting roughing line to main chamber.

16. Put ion pump controller in Start mode and monitor voltage or current. Slowly open gate valve while monitoring voltage or current.

17. As voltage increases or current decreases, continue to open valve. Controller may require as much as an hour to produce normal voltage and current pump settings.

18. After valve has been opened completely and pressure in chamber is 10^{-5} Torr or less (as monitored by pump controller), ion gauge filament may be turned on.

19. When pressure in chamber has stabilized to less than 10^{-8} Torr, sample analysis may be performed.

A.2 Sputtering

1. Turn on argon regulator. (Bleed line if possible to remove oxygen.)
2. Open argon shut-off valve.
3. Make sure ion gauge controller is on to monitor pressure.
4. Place -800v bias on sample from right rack power supply. (Red: -800v to sample; Black: ground to chamber.)
5. Open variable leak valve slowly and monitor ion pump controller voltage. (Want to maintain a high voltage across the pump.)
6. Keep opening the variable leak valve until ion gauge reads 10^{-7} to 10^{-6}. (May be able to reduce pressure further with present multivac controller.)
7. Sputter for a determined period of time. Several hours will be required. (Monitor controller during process and adjust variable leak valve in order to maintain a constant chamber pressure.)
8. Close variable leak valve.
9. Close argon shut-off valve.
10. Remove bias.
11. Close regulator.
12. Wait for pressure to drop to less than 10^{-8} Torr.

A.3 Sample Analysis

1. Turn sample using goniometer so that sample is in line with CMA.
2. Crank in Electron Gun so that metal plates separating the bellows are 3 and 1/8 inches apart. (Measure inner to inner on plates: see log book for illustration.)
3. Connect ground path to sample. (Red: to sample connector; Black to chamber.)
4. Make sure filament current dial is counter-clockwise and emission current dial is clockwise.
5. Turn on power for Auger System Control, Electron Gun Control, Lock-in Amplifier, and Electron Multiplier.
6. Press "ON" for Electron Gun Control and "High Voltage" for Multiplier.
7. Set Beam voltage to 3 KeV.
8. Raise filament current so that emission current meter reads 1mA. (Need 7 turns before any change occurs.)
9. Set the Multiplier to 1900 and the Lock-in Amplifier sensitivity as needed.
10. Set upper/lower limit on the Auger System Control and zero the pen on the Chart Recorder.
11. Press Start on the Auger System Control to begin energy scan. To end scan. press Start again.
12. For shut-down, reverse all steps.

REFERENCES

[1] H. Kroemer, "Heterostructure Bipolar Transistors and Integrated Circuits," *Proceeedings of the IEEE*, vol. 70, no. 1, pp. 13-25, 1982.

[2] J. C. Bean, "Silicon-Based Heterostructures: Column IV Bandgap Engineering," *Proceedings of the IEEE*, vol. 80, no. 4, pp. 571-587, 1992.

[3] T. P. Pearsall, "Silicon-Germanium Alloys and Heterostructures: Optical and Electronic Properties," *CRC Critical Review in Solid State and Materials Science*, vol. 15, issue 6, pp. 551-600, 1989.

[4] K. L. Wang and R. P. G. Karunasiri, "SiGe/Si Electronics and Optoelectronics," *Journal of Vacuum Science and Technology B*, vol. 11, no. 3, pp. 1159-1167, 1993.

[5] M. Arienzo, "SiGe Heterojunctions: Devices and Applications," *Microelectronic Engineering*, vol. 19, no. 1-4, pp. 519-530, 1992.

[6] A. Gruhle,H. Kibbel, U. König, U. Erben, and E. Kasper, "MBE-Grown Si/SiGe HBT's with High β, f_T, and f_{max}," *IEEE Electron Device Letters*, vol. 13, no. 4, pp. 206-208, 1992.

[7] *CRC Handbook of Chemistry and Physics*, R. C. Weast, Editor-in-Chief, CRC Press Inc., Boca Raton, Florida, 1987.

[8] R. A. Soref, "Optical bandgap of ternary semiconductor $Si_{1-x-y}Ge_xC_y$," *Journal Applied Physics*, vol. 70, no. 4, pp. 2470-2472, 1991.

[9] K. S. Furukawa, K. H. Etoh, K. A. Ishizaka, K. T. Shimada. "Semiconductor Devices with Crystalline Silicon-Germanium-Carbon Alloy," *United States Patent*, Number 4,885,614, Dec. 5, 1989.

[10] F. Demichelis, G. Kaniadakis, A. Tagliaferro, E. Tresso, G. Della Mea, and A. Paccagnella, "Investigation on Structure and Optoelectronic Properties of Hydrogenated Amorphous CSiGe:H Alloys," *Solid State Communications*, vol. 70, no. 3, pp. 381-384, 1989.

[11] F. Deminchelis and A. Tagliaferro, "Annealing Temperature Dependence of Conductivity in a-CSiGe:H Alloys Deposited at Different Substrate Temperatures," *Journal of Non-Crystalline Solids*, vol. 114, pp. 468-470, 1989.

[12] F. Demichelis and A. Tagliaferro, "Thermal Equilibrium Processes in Carbon-based Amorphous Semiconducting Ternary Alloys," *Philisophical Magazine B*, vol. 61, no. 5, pp. 867-879, 1990.

[13] J. W. Strane, H. J. Stein, S. R. Lee, B. L. Doyle, S. T. Picraux, and J. W. Mayer, "Metastable SiGeC Formation by Solid Phase Epitaxy," *Applied Physics Letters*, vol. 63, no. 20, pp. 2786-2788, 1993.

[14] A. Gupta, Y. Cheng, J. Qiao, M. Rahman, C. Yang, S. Im, N. Cheung, P. Yu. "Characterization of Ge and C Implanted $Si_{1-x}Ge_x$ and $Si_{1-y-z}Ge_yC_z$ Layers," *Proceedings of Materials Research Society*, Spring 1993.

[15] A. Fukami,K. Shoji, T. Nagano, and C. Yang, "Characterization of SiGe/Si Heterostructures Formed by Ge^+ and C^+ Implantation," *Applied Physics Letters*, vol. 57, no. 22, pp. 2345-2347, 1990.

[16] S. S. Iyer, K. Eberl, A. R. Powell, and B. A. Ek, "SiCGe Ternary Alloys - Extending Si-based Heterostructures," *Microelectronic Engineering*, vol. 19, pp. 351-356, 1992.

[17] S. S. Iyer, "Silicon Molecular Beam Epitaxy," *Epitaxial Silicon Technology*, Academic Press Inc., Orlando, FL, Chapter 2, 1986.

[18] R. J. Malik, R. N. Nottenberg, E. F. Schubert, J. F. Walker, and R. W. Ryan, "Carbon Doping in Molecular Beam Epitaxy of GaAs from a Heated Graphite Filament," *Applied Physics Letters*, vol. 53, no. 26, pp. 2661-2663, 1988.

[19] W. E. Hoke, P. J. Lemonias, P. S. Lyman, H. T. Hendriks, D. Weir, and P. Colombo, "Carbon Doping of MBE GaAs and $Ga_{0.7}Al_{0.3}As$ Films Using a Graphite Filament," *Journal of Crystal Growth*, vol. 111, pp. 269-273, 1991.

[20] A. Ishizaka and Y. Shiraki, "Low Temperature Surface Cleaning of Silicon and Its Applications to Silicon MBE," *Journal of the Electrochemical Society: Electrochemical Science and Technology*, vol. 133, no. 4, pp. 666-671, 1986.

[21] P. J. Grunthaner, F. J. Grunthaner, R. W. Fathauer, T. L. Lin, M. H. Hecht, L. D. Bell, W. J. Kaiser, F. D. Schowengerdt, and J. H. Mazur, "Hydrogen-Terminated Silicon Substrates for Low-Temperature Molecular Beam Epitaxy," *Thin Solid Films*, vol. 183, pp. 197-212, 1986.

[22] J. M. Baribeau, T. E. Jackman, P Maigne, D. C. Houghton, and M. W. Denhoff, "Heteroepitaxy of Ge on (100) Si Substrates," *Journal of Vacuum Science and Technology, A*, vol. 5, no. 4, pp. 1898-1902, 1987.

[23] W. Chupka and M. Inghram, "Molecular Species Evaporating from a Carbon Surface," *Journal of Chemical Physics*, vol. 21, pp. 1313, 1953.

[24] J. Drowart, R. Burns, G. DeMaria, and M. Inghram, "Mass Spectrometric Study of Carbon Vapor," *Journal of Chemical Physics*, vol 31, pp. 1131-1132, 1959.

[25] P. Zavitsanos and G. Carlson, "Experimental Study of the Sublimation of Graphite at High Temperatures," *Journal of Chemical Physics*, vol 59, no. 6, pp. 2966-2973, 1973.

[26] P. Lyman, S. Thevuthasan, and L. Seiberling, "Low Temperature Growth of Ge on Si(100)-(2 multiplied by 1)," *Journal of Crystal Growth*, vol 113, no. 1-2, pp. 45-52, 1991.

[27] S. Zhang, *Growth and Analysis of GeC and SiGeC Thin Films*, Master's Thesis, University of Delaware, 1994.

[28] B. Pregger, *Surface Crystallization of an Amorphous Alloy*, Ph.D. Dissertation, University of Delaware, 1986.

[29] P. Palmberg, G. Riach, R. Weber, and N. MacDonald, *Handbook of Auger Electron Spectroscopy*, Physical Electronics Industries, Inc., Edina, Minnesota, 1972.

[30] W. Chu, J. Mayer, and M. Nicolet, *Backscattering Spectrometry*, Academic Press, Inc., New York, New York, 1978.

[31] D. Beames, *The Use of Rutherford Backscattering Spectrometry for the Analysis of Elemental and Compound Thin Films*, Master's Thesis, University of Delaware, 1988.

[32] L. R. Doolittle, Ph.D. Dissertation, Cornell University, Ithaca, New York, 1987.